IDENTIFYING SULFATE SOURCES AND RECYCLING PROCESSES IN THE ATACAMA DESERT WITH SULFUR, STRONTIUM, AND TRIPLE OXYGEN ISOTOPES

INAUGURAL-DISSERTATION

zur

Erlangung des Doktorgrades

der Mathematisch-Naturwissenschaftlichen Fakultät

der Universität zu Köln

vorgelegt von

Swea Klipsch

aus Solingen

Köln, 2021

Berichterstattter / Gutachter:

Prof. Dr. Michael Staubwasser

Prof. Dr. Carsten Münker

Tag der mündlichen Prüfung:

12.11.2021

Abstract

Sulfate is the dominating salt in soils of the Atacama Desert, one of the oldest and driest deserts on Earth. Sulfate sources include marine sulfate, terrestrial weathering (e.g., redistribution of surface material), and sulfate that is formed within the atmosphere by oxidation of reduced sulfur species. The stable isotopic composition of sulfate ($\Delta^{17}O_{SO_4}$, $\delta^{18}O_{SO_4}$, and $\delta^{34}S_{SO_4}$) is characteristic for each formation process, wherefore it serves as a tool to identify respective sulfate sources. The classical stable isotope proxies ($\delta^{18}O_{SO_4}$ and $\delta^{34}S_{SO_4}$) mainly help to distinguish between marine and terrestrial sulfate. In addition to these, the novel triple oxygen isotope tool ($\Delta^{17}O_{SO_4}$) also allows to identify sulfate formed in the atmosphere. Under Earth's surface conditions, the isotopic composition of sulfate only alters when the sulfate is processed by microbes or plants. Hence, the isotopic composition of sulfate allows identifying the sulfate sources and enables to draw conclusions on biological alteration processes. This is especially interesting for areas, where biological activity is limited due to the low water availability, like the Atacama Desert.

The first study presents a fast and easy to use method to determine $\Delta^{17}O_{SO_4}$ of natural sulfate samples. It includes a protocol for the quantitative dissolution of natural Ca- and Na-sulfates samples and subsequent conversion into sufficiently pure Ag-sulfate for pyrolysis analyses. Determined $\Delta^{17}O_{SO_4}$ values from multiple in-house standards are compared to previously published results from different laboratories using different methods (pyrolysis and fluorination). A normalization procedure results in excellent reproducibility of standards, comparable to other laboratories including those using the fluorination method, verifying the accuracy and precision of the presented method.

The second study aims to improve the understanding of sulfate deposition and the spatial distribution of hyperaridity. Samples taken along four E-W transects are analyzed for their isotopic compositions ($\Delta^{17}O_{SO_4}$, $\delta^{18}O_{SO_4}$, $\delta^{34}S_{SO_4}$, and $^{86}Sr/^{88}Sr$). Throughout positive

$\Delta^{17}O_{SO_4}$ values, determined using the method developed in the first study, suggest a significant contribution from atmospheric sulfate for all Atacama Desert sediments. The combination of $\Delta^{17}O_{SO_4}$ and $\delta^{34}S_{SO_4}$ allows distinguishing between marine sulfate and sulfate that derived from atmospheric oxidation of biogenic sulfur gases emitted from the Ocean. In addition, a clear trend is visible in the triple oxygen isotopic composition ($\Delta^{17}O_{SO_4}$ and $\delta^{18}O_{SO_4}$) of all samples, pointing from the isotopic composition of atmospheric sulfate to that of biological cycled sulfate. This trend reflects a gradient in the degree of biological activity and can therefore be used as indicator for water availability in the Atacama Desert.

This work provides an optimized pyrolysis method for triple oxygen isotope analysis of sulfate from desert environments and expands our knowledge of sulfate source contribution, sulfate deposition, biological sulfate cycling, and water availability within the hyperarid Atacama Desert.

Kurzfassung

Sulfat ist das dominierende Salz in den Böden der Atacama Wüste, einer der ältesten und trockensten Wüsten der Erde. Zu den Sulfatquellen gehören marines Sulfat, terrestrische Verwitterung (z. B. Umverteilung von Oberflächenmaterial) und Sulfat, das in der Atmosphäre durch Oxidation von reduzierten Schwefelspezies gebildet wird. Die stabile Isotopenzusammensetzung von Sulfat ($\Delta^{17}O_{SO_4}$, $\delta^{18}O_{SO_4}$ und $\delta^{34}S_{SO_4}$) ist charakteristisch für den jeweiligen Entstehungsprozess, weshalb sie genutzt werden kann, um die einzelnen Sulfatquellen zu identifizieren. Die klassischen, stabilen Isotopen Systeme ($\delta^{18}O_{SO_4}$ und $\delta^{34}S_{SO_4}$) helfen hauptsächlich bei der Unterscheidung zwischen marinem und terrestrischem Sulfat, während eine positive Anomalie in der 3-Sauerstoffisotopenzusammensetzung ($\Delta^{17}O_{SO_4}$) ein spezifisches Merkmal für in der Atmosphäre gebildetes Sulfat ist. Unter den Bedingungen, die an der Erdoberfläche herrschen, ändert sich die Isotopenzusammensetzung von Sulfat nur, wenn das Sulfat von Mikroben oder Pflanzen verarbeitet wird. Die Isotopenzusammensetzung von Sulfat erlaubt es daher, Sulfatquellen zu identifizieren und Rückschlüsse auf biologische Prozesse zu ziehen. Dies ist besonders interessant für Gebiete, in denen die biologische Aktivität aufgrund der geringen Wasserverfügbarkeit eingeschränkt ist, wie zum Beispiel in der Atacama Wüste.

In der ersten Studie wird eine schnelle und einfach anzuwendende Methode zur Bestimmung von $\Delta^{17}O_{SO_4}$ von natürlichen Sulfatproben vorgestellt. Sie beinhaltet ein Protokoll zur quantitativen Auflösung natürlicher Ca- und Na-Sulfatproben und Umwandlung in ausreichend reines Ag-Sulfat für Pyrolyseanalysen. Ermittelte $\Delta^{17}O_{SO_4}$-Werte von mehreren laborinternen Standards werden mit zuvor veröffentlichten Ergebnissen aus verschiedenen Laboren unter Verwendung unterschiedlicher Methoden (Pyrolyse oder Fluorierung) verglichen. Ein Normalisierungsverfahren führt zu einer ausgezeichneten Reproduzierbarkeit der Standards aus verschiedenen Laboren, einschließlich derjenigen, die die Fluorierungsmethode verwenden, was die Genauigkeit und Präzision der vorgestellten Methode bestätigt.

Die zweite Studie zielt darauf ab, die Sulfatablagerung und die räumlichen Verteilung der Hyperaridität besser zu verstehen. Proben, die entlang von vier E-W Transekten genommen wurden, werden auf ihre Isotopenzusammensetzung ($\Delta^{17}O_{SO_4}$, $\delta^{18}O_{SO_4}$, $\delta^{34}S_{SO_4}$ und $^{86}Sr/^{88}Sr$) analysiert. Die durchweg positiven $\Delta^{17}O_{SO_4}$-Werte, die mit der in der ersten Studie entwickelten Methode bestimmt wurden, deuten auf einen signifikanten Beitrag von atmosphärischem Sulfat für alle Sedimente der Atacama Wüste hin. Die kombinierte Betrachtung von $\Delta^{17}O_{SO_4}$ und $\delta^{34}S_{SO_4}$ erlaubt es, zwischen marinem Sulfat und Sulfat zu unterscheiden, welches aus der atmosphärischen Oxidation von biogenen Schwefelgasen stammt, die aus dem Ozean emittieren. Darüber hinaus wird ein klarer Trend in der 3-Sauerstoffisotopenzusammensetzung ($\Delta^{17}O_{SO_4}$ and $\delta^{18}O_{SO_4}$) aller Proben von der Isotopenzusammensetzung von atmosphärischem Sulfat zu der von biologisch zyklischem Sulfat beobachtet. Dieser Trend spiegelt einen Gradienten im Grad der biologischen Aktivität wider und kann daher als Indikator für die Wasserverfügbarkeit in der Atacama Wüste verwendet werden.

Diese Arbeit liefert eine optimierte Pyrolyse-Methode für die 3-Sauerstoffisotopenanalyse von Sulfat aus Wüstenumgebungen und erweitert das Wissen über den Beitrag von Sulfatquelle, der Sulfatablagerung, dem biologischen Sulfatkreislauf und der Verfügbarkeit von Wasser in der hyperariden Atacama Wüste.

Acknowledgment

First of all, I would like to express my honest gratitude to my supervisor Prof. Michael Staubwasser for his support over the years. He aroused my interest in the field of stable isotopes and fostered my scientific skills from the start of my bachelor thesis until today. I have greatly benefited from insightful discussions, helpful advice, critical feedback, and his sharp thoughts on various scientific topics. I really appreciate that he gave me the opportunity to experience and work in the incredible landscape of the Atacama Desert.

Secondly, I would like to thank Prof. Carsten Münker for infecting me with his enthusiasm for geochemistry and for agreeing to examine this PhD thesis. I am really pleased that he became interested in my research and decided to contribute $^{87}Sr/^{86}Sr$ measurements.

My deepest thanks go to Dr. Daniel Herwartz for being a mentor in all aspects of life and scientific work. Due to his excitement for various scientific topics, every conversation with him provided new perspectives and led to innovative ideas. He always supported me with inspiring discussions and countless pep talks. No matter how bad I felt, he always conjured a smile upon my face. During the ups and especially the downs of the last years, he managed to keep me motivated by taking time, finding the right words, and always being kind and empowering. I definitely would not have made it through my PhD studies without him. Thank you for the risotto.

Special thanks are directed to Prof. Michael Böttcher for contributing $\delta^{18}O$ and $\delta^{34}S$ measurements. In addition, I would like to express my gratitude to Prof. Becky Alexander, Prof. Mark Thiemens, and Prof. David Johnston for providing sample material and for interesting and directive chats during the early stage of my PhD. I would also like to acknowledge our Chilean colleagues Prof. Eduardo Campos and Prof. Guillermo Chong for thier support with administrative issues, collaborative field work, and sharing their comprehensive scientific knowledge about the Atacama Desert. For financial support of my thesis, I want to thank the University of Cologne and the CRC 1211 “Earth-Evolution at the Dry limit”.

I would like to thank Dr. Claudia Voigt and Dr. David Bajnai, presumably the dearest and most supportive colleagues one can wish for. Thank you for your helpful comments, warm encouragement, lunch breaks, coffee breaks, ice cream breaks, chocolate breaks, and all the breaks in general. I am especially grateful to our technician Jochen Scheld, who always had a ready ear and a helping hand to support me in the laboratory. Thanks to my other fellows who supported me over the course of this work and during my studies: Jakub Surma, Chiara Krewer, Marina Kemperle, Stephanie Weinstock, Lucia Halbauer, Nathalie Thor, Patrick Wollenweber, and Stephanie Kusch.

Furthermore, I wish to thank all my dear friends and comrades who had to put up with my stresses and moans over the past years and who always encouraged and supported me: Sophia, Tobi, Julia, Bert, Manni, Mia, Motte, Nina, Sebi, Sandra, Christian, Joh, Silas, and all the others that are too many to be listed here. I am beyond thankful to call this wonderful bunch of people my friends. I also have to thank the most loyal, crazy, loving, and cutest dog in the world, thus, shout out to Lavie for keeping me busy. Special thanks go to my family: Dorothee Buscher-Klipsch, Kalle Greeven, Norbert Klipsch, Jannick Klipsch, Gerhard Klipsch, and Lilo Klipsch. In your own way, each and every one of you is an important role model for me. Thank you for supporting me since day one and making me who I am today. Finally, I want to thank Paul for suddenly flipping my life upside down. Thank you, for all your support, encouragement, and kindness, and for seeing nothing but the best in me. You are probably the most patient, caring, and loving person I know and I really appreciate that you became such an important part of my life.

Table of Contents

1. Introduction

The Atacama is one of the oldest and driest deserts on Earth (Dunai et al., 2005; Evenstar et al., 2017; Schween et al., 2020) even though it is located close to the Pacific Ocean at the western coast of South America. The core of the Atacama Desert receives average annual precipitation lower than 5% of potential evapotranspiration and is therefore characterized as hyperarid (UNEP, 2011). The long-term hyperaridity highly influences biological but also geological processes and has led to the exceptional environment observed today in the Atacama Desert, which often serves as an analog for Mars. Under the prevalent hyperarid climate conditions, surface processes operate relatively slowly leading to preservation of landscapes and traces, which once have been shaped by the influence of water (e.g., fluvial erosion and deposition, weathering, authigenic mineral formation, etc.) (e.g., Dunai et al., 2005; Evenstar et al., 2009, 2017; Ritter et al., 2018; Mohren et al., 2020; Walk et al., 2020). An additional indicator for the long-term hyperaridity are the salt (e.g., halite, sulfate, nitrate) deposits of the Atacama Desert, which are unique on Earth in their extent and composition (Ericksen, 1981, 1983; Chong, 1994; Michalski et al., 2004; Pérez-Fodich et al., 2014; Álvarez et al., 2015; Reich and Bao, 2018). For example, the Atacama nitrate deposits, which can be found in an almost continuous 700 km long and about 20 km wide belt east of the Coastal Cordillera, are by far the largest nitrate deposits in the world Ericksen (1981, 1983); Chong (1994). The accumulation and preservation of such massive amounts of nitrate were only possible due to long-term prevailing hyperarid conditions in the Atacama Desert. Because all nitrate salts are highly soluble, humid conditions and the frequent occurrence of precipitation would have leached-out the nitrates from the sediment. The most dominant salts in Atacama Desert soils are calcium sulfates ($CaSO_4 \cdot xH_2O$; x= 0...2) (Ericksen, 1981, 1983; Ewing et al., 2006; Voigt et al., 2020). Along with nitrates (NO_3^-) and chlorides (Cl^-), sulfates (SO_4^{2-}) play an important role regarding weathering, water infiltration and trapping in the soil, and general soil

dynamics (Ericksen, 1981; Ewing et al., 2006; Davis et al., 2010; Mohren et al., 2020). Prominent features include surfaces covered in powdery gypsum (chuca), gypsum crust formation and disintegration, and polygon patterned grounds (Ericksen, 1981; Davis et al., 2010; Sager et al., 2021). Because sulfate dominates this unique desert environment, it is crucial to identify local sulfate sources and post-depositional processes to understand its deposition and the evolution of the desert landscape. The contribution of each source to the total soil depository varies spatially depending on elevation, distance from sources, and local climate conditions like water availability or prevailing wind direction (Rech et al., 2003; Voigt et al., 2020). In the present thesis, a novel triple oxygen isotope tool ($\Delta^{17}O_{SO4}$) is combined with more classical indicators ($\delta^{18}O_{SO4}$, $\delta^{34}S_{SO4}$, and $^{87}Sr/^{86}Sr$) to disentangle different sulfate sources and estimate their contributions.

1.1. Atacama Desert

The Atacama Desert covers a land strip in southern Peru and northern Chile between 15°S and 30°S from the sea level (Pacific Ocean) to 3500 m altitude (western slope of the high Andes) (Houston and Hartley, 2003). From west to east, the Atacama Desert can be divided into four major tectonic areas (1) the Coastal Cordillera, (2) the Central Depression, (3) the Precordillera, and (4) the Western Cordillera of the high Andes. The Coastal Cordillera mainly shows elevations <2000 m and consists of Jurassic andesitic volcanic rocks intercalated with Cretaceous marine limestone, shale, and conglomerates (Allmendinger and González, 2010). The Central Depression is a topographic low situated between the Coastal Cordillera and the Precordillera with elevations between 1000 and 2000 m. This longitudinal continental forearc basin is filled with several hundred meters of Cenozoic fluvial and lacustrine sediments and alluvial fan deposits from both Cordilleras (Hartley et al., 2000; Hartley and Evenstar, 2010). The Precordillera extends from $1900 - 2300$ m in the west to $3200 - 3650$ m in the east and consists of a number of faulted blocks of Palaeozoic and Mesozoic strata and Cenozoic alluvial sediments interbedded with ignimbrites derived from the Western Cordillera (Victor et al., 2004; Garcia and Hérail, 2005). The Western Cordillera of the high Andes has average altitudes between 3800 and 4500 m and peaks as high as 6350 m. It is a presently active volcanic arc,

with rhyolitic volcanism dating back to the Miocene. Its basement is formed by Precambrian to Early Paleozoic metamorphic rocks and Mesozoic volcanic and sedimentary rocks (Hartley and Evenstar, 2010; Karátson et al., 2012).

The zonal location of the Atacama Desert between 15°S and 30°S in the subtropical high-pressure belt promotes the hyperaridity due to permanent air subsidence caused by the Hadley circulation (Houston, 2006; Nguyen et al., 2013). Additionally, southerly trade winds blow parallel to the coast, which causes upwelling of cold water masses from high latitudes inhibiting the moisture uptake of coastal onshore winds by low-surface evaporation (Thiel et al., 2007). This leads to a stable atmospheric stratification due to a strong temperature inversion layer trapping any Pacific moisture below ~1200 m altitude, inhibiting precipitation, and preventing moisture transport to the interior of the Atacama Desert (Rundel et al., 1991; Hartley and Chong, 2002; Rutllant et al., 2003). Moisture transport from the east is limited due to the rain shadow effect of the high Andes and the long distance to moisture sources from the Atlantic Ocean or Amazonia (Houston and Hartley, 2003). All effects combined lead to the (hyper-)arid conditions presently observed in the Atacama Desert – in parts with less than 2 mm yr^{-1} precipitation (Houston, 2006).

The rare annual precipitation events can be divided into two regimes. First, summer rain occurs at the slope of the Andes and increases with altitude. However, precipitation exceeding 20 mm yr^{-1} is only observed above 2400 m altitude (Houston, 2006). Second, winter rain occurs between the Andes and the coast. This regime of precipitation increases towards the south and values higher than 5 mm yr^{-1} are observed south of 24.5°S (Houston, 2006; Schween et al., 2020). Despite these low annual precipitation amounts, severe precipitation events with >20 mm may occur in relation with cutoff low events, especially in the southern part of the Atacama Desert (Jordan et al., 2019; Reyers and Shao, 2019; Schween et al., 2020). Today, the Central Depression and the Coastal Cordillera above 1200 m between 19°S and 23.5°S receive the least amount of precipitation (Figure 1.1). Aridity generally decreases with increasing distance to this hyperarid core, especially at elevations >4000 m (Houston, 2006).

As rare precipitation events mainly occur in the southern part of the Atacama Desert, moisture transport by fog becomes increasingly important towards the north, especially away from groundwater fed playas (Cáceres et al., 2007). Stratocumulus clouds expanding from

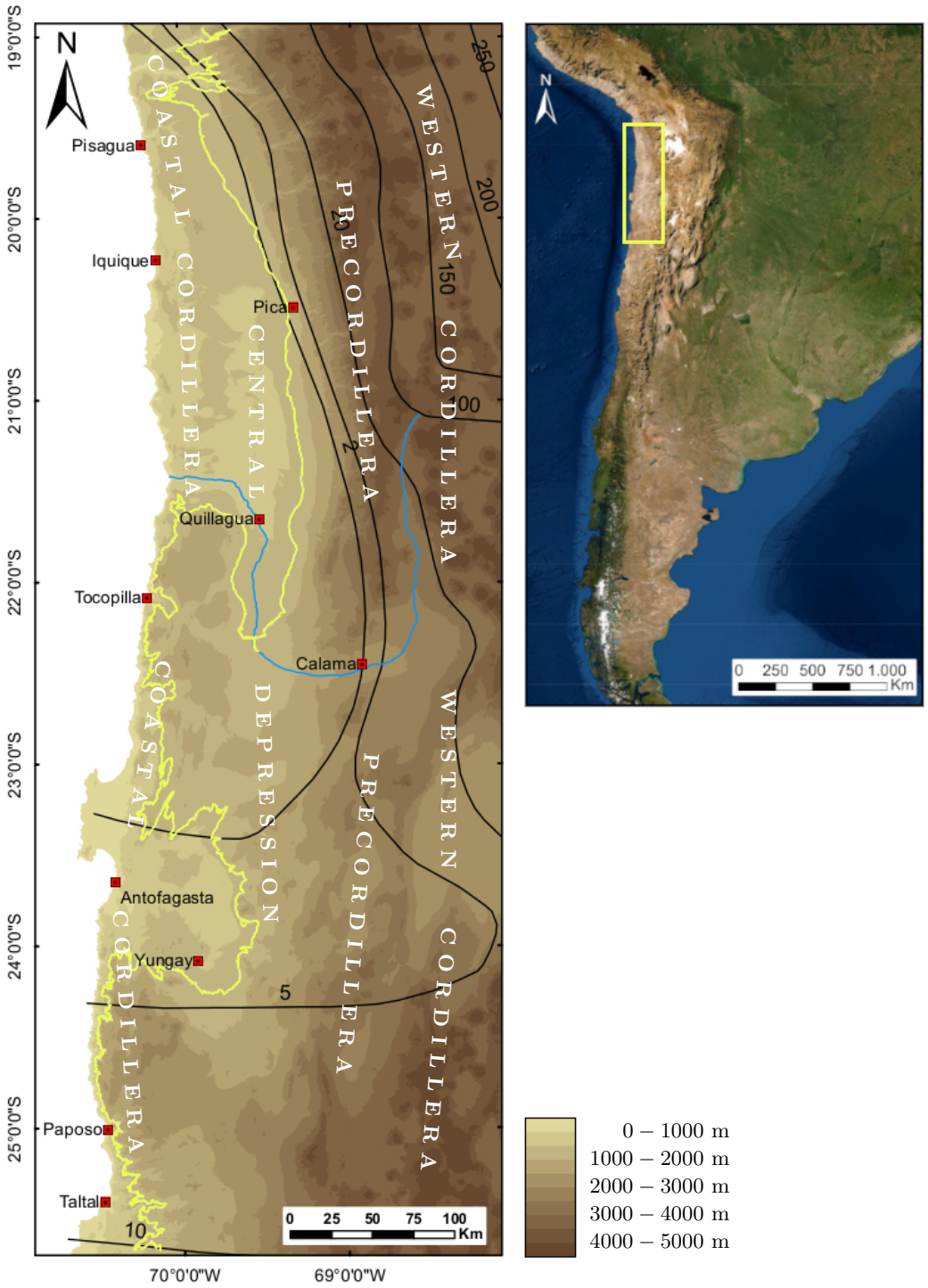

Figure 1.1.: Right panel: Location of the studied area indicated by yellow square.
Left panel: Enlarged section from right panel. Color-shaded digital elevation model derived from SRTM data, created using ArcGIS 10.5.1 with isohyets (solid black lines; numbers are in mm yr^{-1}; Houston, 2006). The maximum extension of fog penetrating inland is approximately equal to 1200 m (solid yellow line; Cereceda et al., 2008).

the Pacific Ocean transport moisture to coastal areas at elevations between 700 and 1000 m but occasionally reaching altitudes down to 600 m and up to 1200 m (Cáceres et al., 2007; Cereceda et al., 2008; Muñoz et al., 2011; Schween et al., 2020). In the northern part of the Atacama Desert (between 19°S and 22°S), the Coastal Cordillera is generally lower than 1200 m and additionally intersected by deep canyons (quebradas), through which fog can penetrate deeper inland (Cereceda et al., 2008). Between 22°S and 25.5°S, the mean altitude of the Coastal Cordillera is 1500 m with several zones being >2000 m high. Hence, in this southern part of the Atacama Desert, the Coastal Cordillera effectively blocks the advective fog from penetrating inland. An exception is the coastal region near Antofagasta (Figure 1.1), where inland fog is regularly observed (Cáceres et al., 2007). Additionally, radiative fog may occur when temperatures in the Central Depression strongly decrease at night causing condensation of atmospheric vapor initiating fog formation (Cereceda et al., 2008; Schween et al., 2020).

1.2. Triple Oxygen Isotopes

Oxygen has three stable isotopes, ^{16}O, ^{17}O, and ^{18}O, which have average terrestrial abundances in atom per cent of 99.76206, 0.03790 and 0.20004, respectively (Coplen et al., 2002). Analyses of the stable oxygen isotopes provide insights into recent and paleo geo-, bio-, and cosmochemical, hydrological, and atmospheric phenomena for nearly a century (Urey and Bradley, 1931; Manian et al., 1934; Urey, 1947; McCrea, 1950; Craig et al., 1963). The triple oxygen isotope composition between different reservoirs vary due to preference and discrimination of isotopes during natural processes. Differences in the resulting oxygen isotope ratios can help to identify these processes (e.g., Barkan, 2007; Hofmann et al., 2012; Landais et al., 2012; Pack and Herwartz, 2014; Casado et al., 2016; Sharp et al., 2016; Surma et al., 2021; Voigt et al., 2021).

1.2.1. Terminology

The oxygen isotope composition of a material is commonly reported relative to an internationally accepted standard using δ notation:

$$\delta^{*}\mathrm{O} = \frac{{}^{*}R_{smp}}{{}^{*}R_{std}} - 1, \tag{1.1}$$

where ${}^{*}R$ is the mole ratio of the rare over the abundant isotope ($^{17}\mathrm{O}/^{16}\mathrm{O}$ or $^{18}\mathrm{O}/^{16}\mathrm{O}$) in the sample (${}^{*}R_{smp}$) and standard material (${}^{*}R_{std}$), and * denotes the mass of the rare isotope (17 or 18, respectively). In a similar fashion, the δ notation is used for other elements, e.g., for sulfur $\delta^{34}\mathrm{S}$ with $R = {}^{34}\mathrm{S}/^{32}\mathrm{S}$.

In general, differences in the isotope ratio of matter evolve due to fractionation processes like phase transitions, transport, or chemical reactions. The fractionation between two phases A and B can be expressed by the fractionation factor ${}^{*}\alpha_{A-B}$:

$$ {}^{*}\alpha_{A-B} = \frac{{}^{*}R_A}{{}^{*}R_B}. \tag{1.2} $$

For a specific fractionation process, $^{17}\alpha$ and $^{18}\alpha$ are related by the triple oxygen isotope exponent θ (Young et al., 2002):

$$ \begin{aligned} \theta &= \frac{ln(^{17}\alpha)}{ln(^{18}\alpha)} \\ {}^{17}\alpha &= {}^{18}\alpha^{\theta} \ . \end{aligned} \tag{1.3} $$

Fractionation processes can be divided into mass-independent and mass-dependent processes. For mass-independent processes, θ is approximately 1 resulting in $^{17}\alpha \approx {}^{18}\alpha$. For mass-dependent processes, θ varies between 0.5 and 0.5305 depending on the specific fractionation process, the substances involved, and fractionation temperature (Matsuhisa et al., 1978; Bao et al., 2016; Herwartz, 2021). The value of approximately 0.5 is a result of the relative mass difference between $^{17}\mathrm{O}$ and $^{16}\mathrm{O}$, and $^{18}\mathrm{O}$ and $^{16}\mathrm{O}$:

$$ \frac{17-16}{18-16} = \frac{1}{2} = 0.5. \tag{1.4} $$

In natural processes, like evaporation or condensation, several mass-dependent fractionation processes occur simultaneously. Observed correlations between $\delta^{17}\mathrm{O}$ and $\delta^{18}\mathrm{O}$ are described by (Bao et al., 2016):

$$ \delta^{17}\mathrm{O} = \lambda \cdot \delta^{18}\mathrm{O}. \tag{1.5} $$

Deviations from this mass-dependent correlation can be illustrated by the $\Delta^{17}O$ notation:

$$\Delta^{17}O = \delta^{17}O - \lambda \cdot \delta^{18}O. \tag{1.6}$$

Note that λ is arbitrary and thus a variety of definitions for $\Delta^{17}O$ are in use. For terrestrial materials, 0.52 is a reasonable average value λ (Matsuhisa et al., 1978) and is commonly used when dealing with large mass-independent fractionation effects (Savarino et al., 2001; Alexander et al., 2002; Kunasek et al., 2010; Schauer et al., 2012; Geng et al., 2013; Hill-Falkenthal et al., 2013; Walters et al., 2019). The focus of this study is to reveal and interpret such mass-independent oxygen isotope signatures in sulfates. Therefore, $\lambda = 0.52$ is used throughout the present thesis.

1.2.2. Mass-Independent Oxygen Isotope Signatures

Meteorites

A mass-independent oxygen isotope correlation of $\delta^{17}O \approx \delta^{18}O$ was first observed in calcium-aluminum-rich inclusions (CAI) from the carbonaceous chondrite, Allende (Clayton et al., 1973). Additional measurements of CAIs, hibonite-bearing inclusions from a CM chondrite (Murchison), and a chondrule from a carbonaceous chondrite (Acfer214) revealed depletions in $\delta^{18}O$ and $\delta^{17}O$ of up to 75‰ (Kobayashi et al., 2003; Liu et al., 2009). Complementary, enrichments in $\delta^{18}O$ and $\delta^{17}O$ of up to 180‰ were found in the aqueous altered matrix of a primitive carbonaceous chondrite (Acfer094) (Sakamoto et al., 2007). The prevailing view is that the mass-independent oxygen isotope correlation reflects a chemical process (Dauphas and Schauble, 2016), rather than a nucleosynthetic process as initially proposed by Clayton et al. (1973). The chemical process might be self-shielding in the ultraviolet photo-dissociation of carbon monoxide (Clayton, 2002; Lyons and Young, 2005). Alternatively, a symmetry-based dynamical fractionation effect is postulated for monoxide (e.g., SiO) recombination on the surface of growing CAIs (Marcus, 2004; Chakraborty et al., 2013) similar to the fractionation effect observed during the formation of ozone (Gao and Marcus, 2001).

Ozone

Thiemens and Heidenreich (1983) first demonstrated experimentally that the formation of ozone from molecular oxygen results in a mass-independent oxygen isotope correlation of $\delta^{17}O \approx \delta^{18}O$ in ozone. Oxygen isotope measurements of stratospheric ozone later confirmed equal enrichments in $\delta^{18}O$ and $\delta^{17}O$ of up to 100‰ (e.g., Mauersberger, 1987; Schueler et al., 1990). The distinct mass-independent oxygen isotope signature is thought to originate mainly from the formation reaction. The formation of ozone proceeds through two collisions. A two-body O-O_2 collision forms the metastable state of ozone (O_3^*) which can stabilize to ozone (O_3) by an inelastic collision with a third body M (Babikov et al., 2003; Teplukhin and Babikov, 2018):

$$O + O_2 \longleftrightarrow O_3^*, \tag{1.7}$$

$$O_3^* + M \longrightarrow O_3 + M. \tag{1.8}$$

In both equations any combination of ^{16}O, ^{17}O, and ^{18}O may be involved. The observed isotope effect is independent of the identity of M that can be any atmospheric atom or molecule (typically N_2) (Babikov et al., 2003). The possibility for a stabilization increases with the lifetime of O_3^*. The dissociation lifetime is strongly affected by the substitution of ^{17}O or ^{18}O into the ozone molecule and the position (central or distal) of these rare isotopes in the ozone molecule (Janssen et al., 2001; Babikov et al., 2003). Thus, a long dissociation lifetime of O_3^* leads to a higher formation rate of the respective stable ozone isotopologue. In addition, the formation rate of a certain ozone isotopologue depends on the isotope concentration of the involved oxygen atoms. Figure 1.2 shows the formation rate coefficient (formation rate relative to the isotope concentration) of stable ozone isotopologues for different formation pathways relative to the $^{16}O + {}^{16}O^{16}O = {}^{16}O^{16}O^{16}O$ pathway. The observed mass-independent oxygen isotope signature of ozone ($\delta^{17}O/\delta^{18}O \approx 1$) is probably a result of varying formation rates of different ozone isotopologues.

The mass-independent fractionation effect during ozone formation results in (1) an enrichment of heavy isotopes in ozone, and (2) a corresponding depletion in the residual atomic and molecular

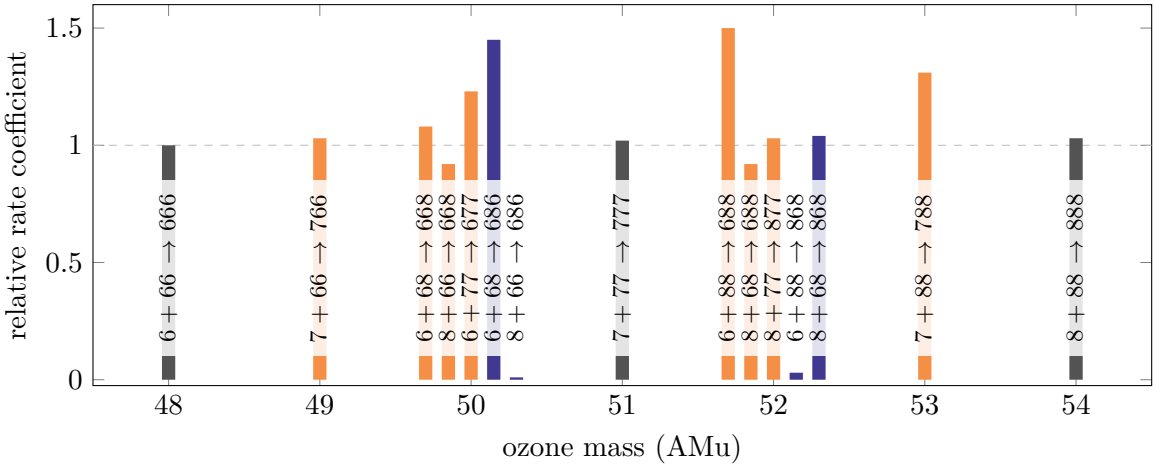

Figure 1.2.: Variable formation rates coefficients of stable ozone for different formation pathways relative to $^{16}O + {}^{16}O^{16}O = {}^{16}O^{16}O^{16}O$ (AMu 48). The relative formation rate of 1 is indicated by the dashed line. Displayed in gray are mono-isotopic pathways, blue shows symmetric, and orange asymmetric final ozone isotopologues. 6, 7, and 8 represent ^{16}O, ^{17}O, and ^{18}O, respectively. Data derived from Mauersberger et al. (2005) and references therein.

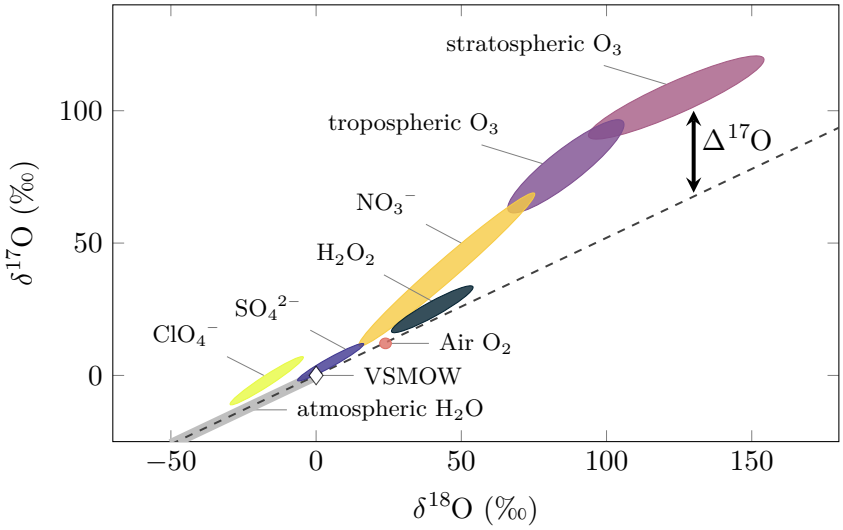

Figure 1.3.: Oxygen isotopic composition ($\delta^{18}O$ and $\delta^{17}O$) of atmospheric compounds. The dashed line displays the mass-dependent fractionation line with a slope of 0.52. Figure modified from Thiemens (2006); Thiemens and Lin (2021).

oxygen (Thiemens and Heidenreich, 1983). Since the O_2 reservoir in the atmosphere is extremely large compared to that of O_3, the isotope effect in O_2 is relatively small ($\Delta^{17}O = -0.32‰$, recalculated with $\lambda = 0.52$; Pack, 2021) compared to that observed in O_3 ($\Delta^{17}O = +20‰$ to $+40‰$; Johnston and Thiemens, 1997). The effect diminishes at high gas pressure or high temperature conditions, where collision rates with surrounding molecules increase and O_3^* lifetime differences become less important (Dauphas and Schauble, 2016). However, details of the fractionation mechanism are still not fully understood (Teplukhin and Babikov, 2018; Miller and Pack, 2021; Thiemens and Lin, 2021).

During atmospheric reactions, the unique triple oxygen isotope signature of O_3 is transferred to other oxygen bearing compounds like hydrogen peroxide (H_2O_2), perchlorate (ClO_4^-), stratospheric carbon dioxide (CO_2), sulfate (SO_4^{2-}), or nitrate (NO_3^-) (Figure 1.3). Aerosols of these compounds therefore show positive ^{17}O anomalies. After deposition, this unique oxygen isotope signature allows to identify the contribution of the atmospheric source within a sedimentary record (Bao et al., 2004; Michalski et al., 2004). The present thesis investigates the potential of the triple oxygen isotope composition of sulfates from Atacama Desert sediment samples to identify different sulfate sources.

1.3. Isotope Characteristics of Sulfate Sources

Sulfate can be found in continental rocks and sediments, dissolved in water, or as aerosol in the atmosphere. Once formed, the oxygen isotope composition of sulfate remains generally unchanged. Under abiotic conditions sulfate requires about 10^9 years to fully exchange its oxygen isotope inventory with that of water (at marine pH and temperature; Rennie and Turchyn, 2014). The isotopic composition of sulfate can however be altered when it is exposed to extremely acidic or higher temperature/pressure conditions (Kusakabe and Robinson, 1977; Chiba et al., 1981; Rennie and Turchyn, 2014), or when processed by microbes or plants (Böttcher et al., 2001; Koprivova and Kopriva, 2016). Sulfate can form via oxidative weathering of sulfides, precipitate from evaporating water, or accumulate by wet and dry atmospheric deposition (Bao et al., 2001a, 2004; Michalski et al., 2004). These individual sulfate sources comprise distinct isotopic fingerprints that are discussed in detail in the following subsections.

1.3.1. Terrestrial Sulfate

Terrestrial weathering as sulfate source includes dissolution and reprecipitation of sulfate (e.g., $CaSO_4$) and oxidative weathering of sulfides. During dissolution, the isotopic composition of sulfate maintains unchanged and thus, reflects the isotopic composition of the original sulfate source. Sulfides, like pyrite (FeS_2), are oxidized biotically or abiotically via dissolved oxygen, or though reaction with Fe^{3+} and H_2O (Balci et al., 2007; Tichomirowa and Junghans, 2009; Kohl and Bao, 2011). These two main oxidation processes can be described by the following bulk reactions (e.g., Singer and Stumm, 1970)

$$FeS_2 + \frac{7}{2}\,O_2 + H_2O \longrightarrow 2\ {SO_4}^{2-} + Fe^{2+} + 2\ H^+ \tag{1.9}$$

$$FeS_2 + 14\ Fe^{3+} + 8\ H_2O \longrightarrow 2\ {SO_4}^{2-} + 15\ Fe^{2+} + 16\ H^+ \tag{1.10}$$

The oxygen isotope composition of the produced terrestrial sulfate depends on (1) the proportion of these two reactions and whether these reactions proceed biotically or abiotically, (2) the oxygen isotope composition of dissolved O_2 and H_2O, (3) the relation between the sulfate formation rate and the oxygen isotope exchange rate between water and the intermediates during sulfate production (e.g., sulfite (${SO_3}^{2-}$)), and (4) equilibrium and kinetic isotope fractionation during the oxidation itself or during isotope exchange, e.g., between water and sulfite (Pisapia et al., 2007; Thurston et al., 2010; Kohl and Bao, 2011; Bao, 2015; Cao and Bao, 2021). These aspects lead to an overall fractionation effect in $\delta^{18}O$ between sulfate and H_2O of +2‰ to +16‰, and between sulfate and O_2 of −29‰ to −4‰ (Thurston et al., 2010). All these aspects and processes are expected to affect the oxygen isotope composition mass-dependently, wherefore $\Delta^{17}O_{SO_4}$ values from 0‰ to slightly negative values (down to −0.3‰) gained from atmospheric O_2 or highly evaporated water are reasonable. The sulfur isotope composition of the formed sulfate depends on similar aspects: (1) the proportion of the two reactions and whether they proceed biotically or abiotically, (2) the sulfur isotope composition of the oxidized sulfide, and (3) equilibrium and kinetic isotope fractionation effects (Pisapia et al., 2007; Thurston et al., 2010). The overall fractionation effect in $\delta^{34}S$ between the formed sulfate and the oxidized sulfide varies between −4‰ and +5‰ (Thurston et al., 2010).

Due to the low water availability in the Atacama Desert oxidative weathering of sulfides is generally limited. However, in salt lakes, like the Salar de Llamará, sulfate is reduced to H_2S, which diffuses to the surface where it is reoxidized to sulfate. The isotopic characteristics of this cycled sulfate is described in subsection 1.3.4 (p. 17).

1.3.2. Marine Sulfate

Marine sulfate mainly originates from terrestrial weathering delivered to the ocean by rivers (Wortmann et al., 2007; Burke et al., 2018; Waldeck et al., 2019). Sulfate is then removed from the ocean through biological reactions and precipitation of sedimentary sulfides (e.g., pyrite) and sulfates (evaporites and carbonate associated sulfate). Thus, the isotopic composition of marine sulfate represents a global average of terrestrial weathering, modified by the fractionation introduced by biological sulfate cycling.

The isotopic composition of marine sulfate is well characterized and generally invariable due to the long residence time of sulfate in the ocean compared to the much shorter oceanic mixing time (~10^7 years and 10^3 years, respectively; Turchyn and Schrag, 2004). The oxygen isotope composition of marine sulfate is $+8.67 \pm 0.21$‰ and 0.07 ± 0.02‰ for $\delta^{18}O_{SO_4}$ and $\Delta^{17}O_{SO_4}$, respectively (recalculated with $\lambda = 0.52$; Waldeck et al., 2019). The $\delta^{34}S_{SO_4}$ value of marine sulfate is 21.15 ± 0.15‰ (Johnston et al., 2014).

1.3.3. Atmospheric Sulfate

Atmospheric sulfate can be divided into emissions of fully oxidized sulfate at the source called primary atmospheric sulfate = PAS and sulfate that is formed within the atmosphere by oxidation of reduced sulfur species called secondary atmospheric sulfate = SAS.

Primary Atmospheric Sulfate

PAS emits directly as sulfate into the atmosphere. Sources include anthropogenic emissions from fossil fuel combustion or industrial processes, volcanoes, sea spray, and wind erosion (Bao et al., 2004; Mather et al., 2006; Dominguez et al., 2008; Alexander et al., 2012). PAS is isotopically indistinguishable from the initial sulfate sources, e.g., marine sulfate or cycled sulfate, which are described individually in their respective subsections.

Secondary Atmospheric Sulfate

Secodary atmospheric sulfates originate from oxidation of reduced sulfur species in the atmosphere (e.g., SO_2). They show a unique positive $\Delta^{17}O_{SO_4}$ (see above). The three major sources of reduced sulfur gases to the atmosphere are (1) anthropogenic emissions, (2) emission from volcanoes, and (3) biogenic sulfur gases emitted from the ocean (e.g., dimethyl sulfide (DMS), a waste produced by phytoplankton) (Brimblecombe, 2013).

The oxidation is initiated by rapid equilibrium oxygen exchange between the gas phase sulfur species and liquid water droplets described by (Newman et al., 1991; Michalski et al., 2004):

$$SO_2 + H_2O_{(l)} \longleftrightarrow H_2SO_3 \longleftrightarrow H^+ + HSO_3{}^- \longleftrightarrow 2H^+ + SO_3{}^{2-}. \tag{1.11}$$

All sulfur species in (1.11) have the same oxidation state and are collectively termed S(IV). As oxygen isotopes exchange rapidly between the different S(IV) species, all S(IV) species generally have the same oxygen isotope composition as tropospheric H_2O with $\delta^{18}O = -15‰$ to $-5‰$ and $\Delta^{17}O \approx 0‰$ in the South American atmosphere (Bowen and Wilkinson, 2002; Uemura et al., 2010) (Figure 1.3 and Figure 1.4). S(IV) is then oxidized to sulfate either in gas phase via OH, or in aqueous phase via O_3, H_2O_2 or transition-metal-catalyzed via O_2 (Savarino et al., 2000). During these reactions oxygen and its isotopic composition is transmitted from the oxidant to the final sulfate ion (Savarino et al., 2000). The oxidant OH shows the same oxygen isotope composition as tropospheric H_2O and thus S(IV), while the other possible oxidants – O_3, H_2O_2, and O_2 – show significant different oxygen isotope signatures compared to S(IV) (Figure 1.4). Hence, the oxygen isotope composition of sulfates originating from aqueous phase oxidation ($SO_{4(O_3)}$, $SO_{4(H_2O_2)}$, and $SO_{4(O_2)}$) falls between S(IV) and the respective oxidant in the triple oxygen isotope space (Figure 1.4).

The dominance of an oxidation pathway mainly depends on temperature, the amount of each reactant, and the pH value of the aqueous phase in the atmosphere (Liang and Jacobson, 1999; Martin et al., 2014). Generally, H_2O_2 is the major oxidant at pH values below 6, while oxidation via O_3 becomes increasingly important for pH values above 6 (Liang and Jacobson, 1999). For anthropogenic and volcanic emissions to the North Chilean atmosphere, the relative contribution of each S(IV) oxidation pathway was estimated from several global circulation

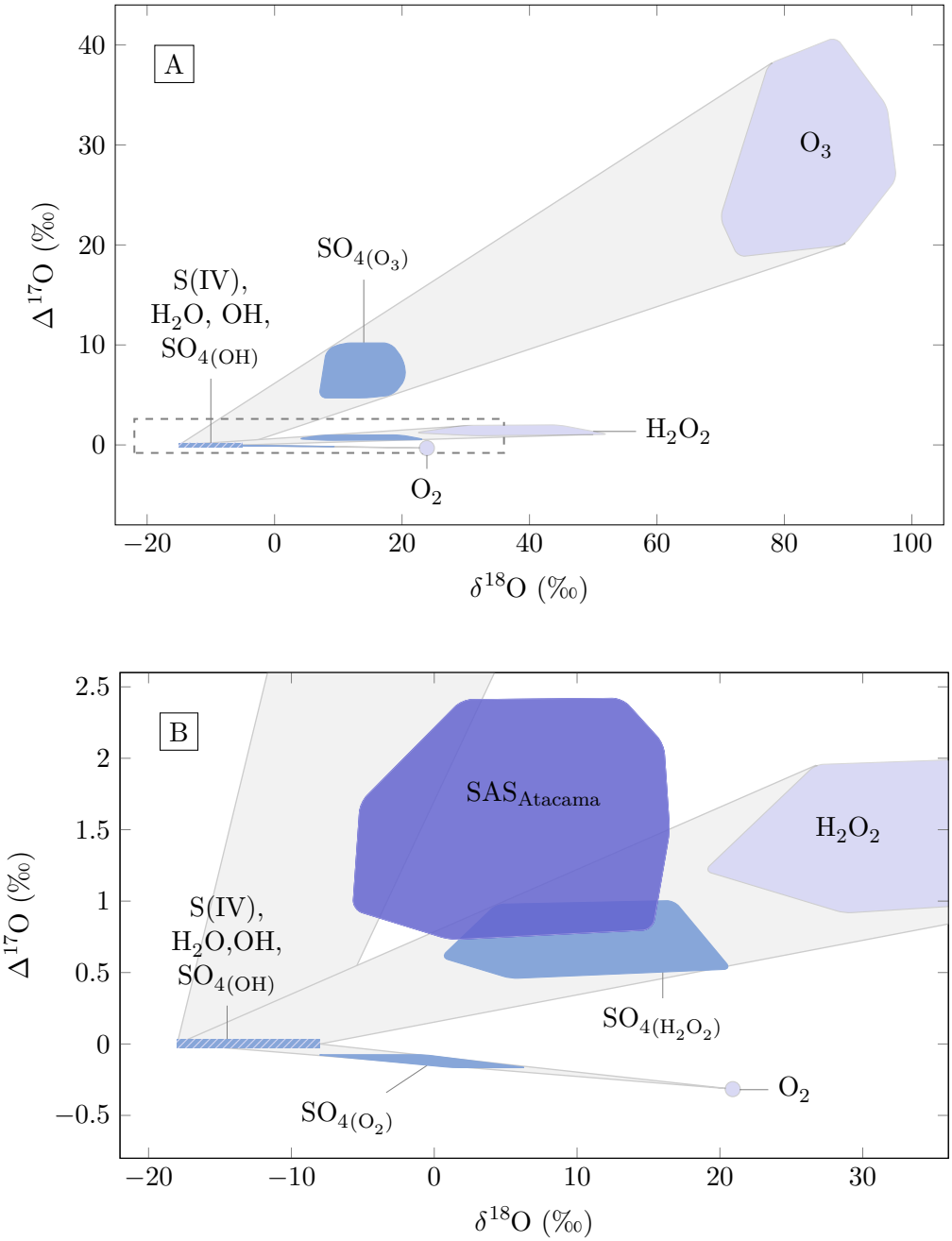

Figure 1.4.: A) $\delta^{18}O$ and $\Delta^{17}O$ values of S(IV) and its oxidants (O_3, H_2O_2, O_2, OH, and H_2O) in the troposphere and the respective resulting $\delta^{18}O_{SO_4}$ and $\Delta^{17}O_{SO_4}$ values of the oxidized endmember sulfate ($SO_{4(O_3)}$, $SO_{4(H_2O_2)}$, $SO_{4(O_2)}$, and $SO_{4(OH)}$). Gray areas indicate each oxidation pathway. Data originates from Johnston and Thiemens (1997); Savarino and Thiemens (1999); Savarino et al. (2000); Bowen and Wilkinson (2002); Pack (2021).
B) Enlarged section from A) (indicated by the dashed square) with additional predicted $\delta^{18}O_{SAS}$ and $\Delta^{17}O_{SAS}$ values of SAS based on various global circulation models (Feichter et al., 1996; Barth et al., 2000; Rasch et al., 2000; Berglen et al., 2004; Sofen et al., 2011).

models giving total ranges of 11 - 36% oxidation via OH, 8 - 17% via O_3, 50 - 74% via H_2O_2, and 0 - 5% transition-metal-catalyzed via O_2 (Feichter et al., 1996; Barth et al., 2000; Rasch et al., 2000; Berglen et al., 2004; Sofen et al., 2011). These relative contributions and the oxygen isotope signatures of $SO_{4(OH)}$, $SO_{4(O_3)}$, $SO_{4(H_2O_2)}$, and $SO_{4(O_2)}$ shown in Figure 1.4 were used to define a range of the possible oxygen isotope composition of SAS for the Atacama Desert. The $\delta^{18}O_{SAS}$ values vary between -2.8‰ and 19.5‰, while $\Delta^{17}O_{SAS}$ values show a range from 0.7‰ to 2.4‰ (Figure 1.4B). When studying a rather polluted atmosphere, these models might underestimate the transition-metal-catalyzed O_2 oxidation pathway (Alexander et al., 2009; Harris et al., 2013; Li et al., 2020). However, for the rather clean southern hemisphere up to 5% of S(IV) oxidation proceeding through the O_2 pathway is a reasonable assumption. Biogenic sulfur gases emitted from the ocean are mainly oxidized within the marine boundary layer, where alkaline conditions lead to higher contributions of the O_3 oxidation pathway (Alexander et al., 2012). The relative amounts of each oxidation pathway vary significantly within the marine boundary layer due to unstable prevalent conditions, resulting in variable amounts and thus variable proportions of the reactants (Dominguez et al., 2008; Alexander et al., 2012). Nevertheless, biogenic sulfur gases (e.g., DMS) above the ocean are dominantly oxidized via O_3 due to aerosol pH > 6. In order to model this endmember, hereafter referred to as '$SAS_{(DMS)}$', it is assumed that O_3 is the only reactant (Figure 1.5).

The sulfur isotope composition of SAS mainly depends on the $\delta^{34}S$ of the S(IV) source and varies slightly with the relative contribution of each oxidation pathway (Harris et al., 2012, 2013). Anthropogenic and volcanic emissions show ranges in $\delta^{34}S_{SO_4}$ of -3‰ to 10‰ and -7‰ to 7‰, respectively (Nielsen, 1974; Thode, 1991; Krouse and Mayer, 2000; Bao et al., 2003). Biogenic sulfur gases emitted from the ocean show a narrow range in $\delta^{34}S$ of 18.9‰ to 20.3‰ (Amrani et al., 2013). At low temperatures, high humidity, and high aerosol concentrations (haze episodes), fractionation effects during S(IV) oxidation may lead to sulfate aerosol with $\delta^{34}S$ values 5 ± 2‰ higher compared to the S(IV) source (Mukai et al., 2001; Li et al., 2020). However, such conditions are generally not observed in the Atacama Desert, wherefore fractionation effects are expected to be small. Here, the $\delta^{34}S$ of the S(IV) source is assumed for the formed sulfate resulting in $\delta^{34}S_{SO_4}$ ranges of -3‰ to 10‰, -7‰ to 7‰, and 18.9‰ to 20.3‰ for anthropogenic SAS, volcanic SAS, and $SAS_{(DMS)}$, respectively.

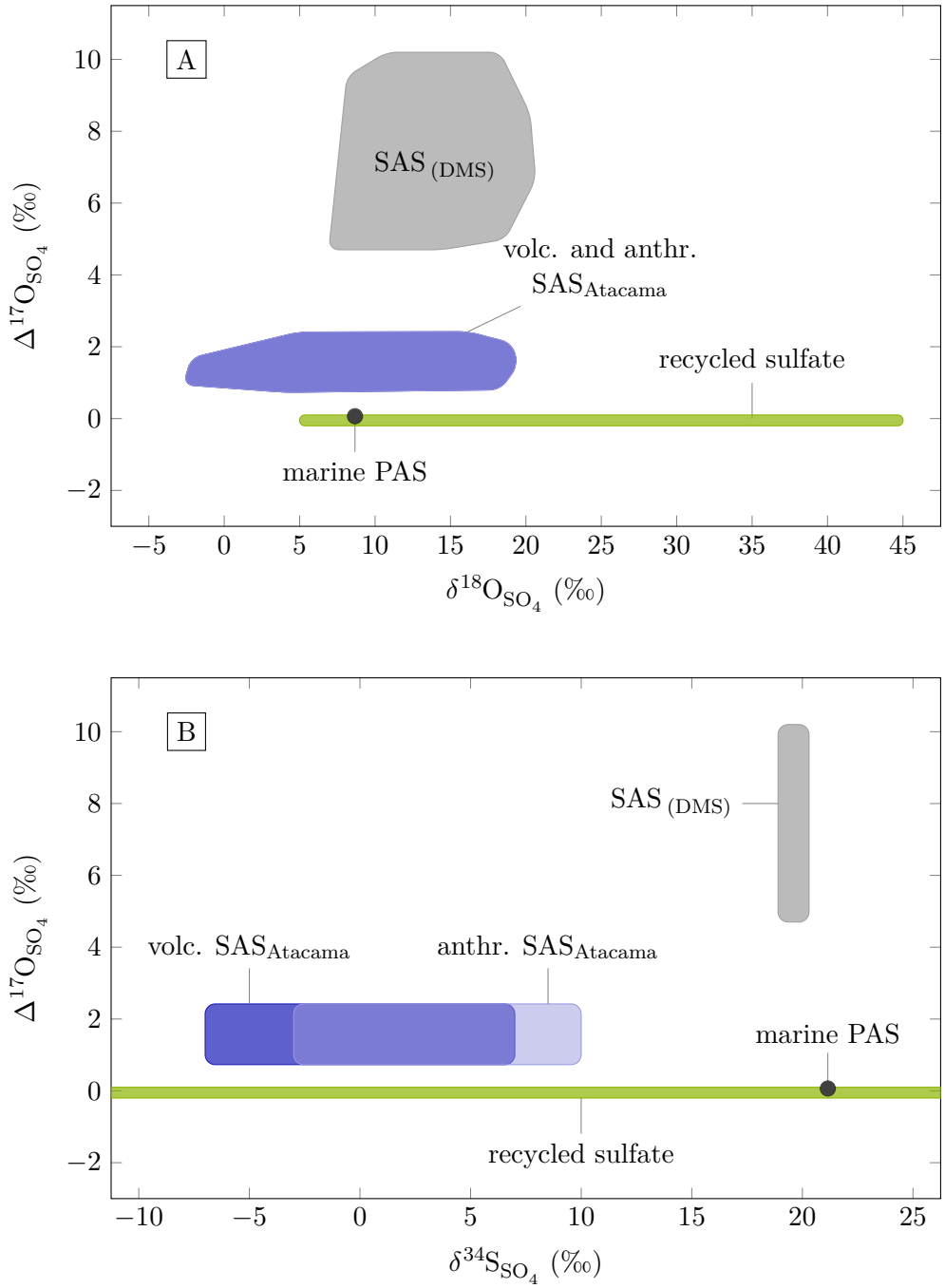

Figure 1.5.: The isotope composition A) $\Delta^{17}O_{SO_4}$ versus $\delta^{18}O_{SO_4}$ and B) $\Delta^{17}O_{SO_4}$ versus $\delta^{34}S_{SO_4}$ of each individual sulfate source. Sources include SAS that originates from volcanic and anthropogenic emissions and from biogenic sulfur gases (e.g., DMS), marine sulfate, and biological cycled sulfate.

1.3.4. Cycled Sulfate

Sulfate is taken up by plants, which reduce sulfate to sulfite and further to sulfide when it is assimilated into amino acid cysteine (Koprivova and Kopriva, 2016). Additionally, in anaerobic environments, the sulfur cycle is dominated by microbial sulfate reduction (Wankel et al., 2014). In these biological sulfate reduction pathways, sulfuroxy intermediates exchange their oxygen with ambient water and thereby overprint the original oxygen isotope signal (Betts and Voss, 1970; Böttcher et al., 2001). The reduced sulfur species (e.g., sulfite (SO_3^{2-}) and sulfide (H_2S)) are subsequently abiotically or biotically reoxidized to sulfate via dissolved O_2, Fe^{3+}, or other oxidants (Bao, 2015; Cao and Bao, 2021). The reoxidized sulfate is hereinafter termed 'cycled sulfate'.

The oxygen isotope composition of cycled sulfate depends on (1) the oxygen isotope signature of the respective oxygen source (O_2 and H_2O), (2) the relative proportion of each oxidation pathway, (3) the oxygen exchange rates between water and the sulfuroxy intermediates (e.g., SO_3^{2-}), (4) respective fractionation factors, and (5) general reaction rates (Wankel et al., 2014). Calculations (Zeebe, 2010) and observations (Böttcher et al., 2001; Farquhar et al., 2008) predict an overall oxygen isotope fractionation between cycled sulfate and H_2O of 15‰ to 30‰ in $\delta^{18}O$. The oxygen isotope composition of water in the Atacama Desert (e.g., salar water) depends largely on the degree of evaporation at given climatic conditions (e.g., temperature, relative humidity, and wind speed), the amount of recharge, the oxygen isotope composition of all involved H_2O species (i.e., initial water, atmospheric water vapor, recharge water), and salinity (Surma et al., 2018; Voigt et al., 2021). Observed salar water isotope compositions cover a wide range in $\delta^{18}O_{H_2O}$ of -10‰ to 15‰, but show a rather limited variability in $\Delta^{17}O_{H_2O}$ of -0.1‰ to 0.1‰ (recalculated with $\lambda = 0.52$), because all involved processes are mass-dependent (Surma et al., 2018; Voigt et al., 2021). Hence, for cycled sulfate in the Atacama Desert assuming a $\delta^{18}O_{SO_4}$ range between 5‰ and 45‰ and a $\Delta^{17}O_{SO_4}$ range between -0.2‰ and 0.1‰ is reasonable. The more negative $\Delta^{17}O_{SO_4}$ values derive from oxidation via O_2 or highly evaporated water.

The sulfur isotope composition of the cycled sulfate is controlled by the $\delta^{34}S_{SO_4}$ of the initial sulfate, the sulfur flux through the network of involved biochemical reactions, as well as the kinetic and equilibrium isotope effects associated with each step within the reaction

network (Johnston et al., 2007; Bradley et al., 2011; Wankel et al., 2014). The sulfur isotope composition of possible initial sulfates already covers a large range in $\delta^{34}S_{SO_4}$ from −7‰ to 21.15‰. Therefore, a range in $\delta^{34}S_{SO_4}$ of cycled sulfate is not further defined.

1.3.5. Strontium

The strontium isotope ratio of matter is influenced by the β^- decay of ^{87}Rb to ^{87}Sr with a half life of $T_{1/2} = 4.96 \cdot 10^{10}$ years (Villa et al., 2015). Due to the geochemical behavior of Rb during partial melting and subsequent melt transport, the bulk continental crust is enriched in Rb relative to the primitive mantle (Wedepohl, 1991). The radioactive decay of ^{87}Rb subsequently leads to higher $^{87}Sr/^{86}Sr$ ratios in the continental crust (global average from modern rivers $^{87}Sr/^{86}Sr = 0.712$) compared to the Rb depleted mantle with $^{87}Sr/^{86}Sr = 0.702$ (Palmer, 1992; McArthur, 1994). Sr fluxes to the ocean of these two main Sr sources – continental crust and mantle – vary due to different intensities of seafloor spreading and continental rock weathering leading to variations of marine $^{87}Sr/^{86}Sr$ over geological time scales (Brass, 1975; Burke et al., 1982). Globally, the strontium isotope ratio is invariable within the ocean, due to the long residence time of strontium in the ocean compared to the much shorter oceanic turnover time (~10^6 years and 10^3 years, respectively; Burke et al., 1982; McArthur, 1994). The modern marine $^{87}Sr/^{86}Sr$ ratio is 0.7091 (Burke et al., 1982), while groundwater in the Atacama Desert shows a range in $^{87}Sr/^{86}Sr$ from 0.705 to 0.715 (Gamboa et al., 2019; Godfrey et al., 2019).

Sr is geochemically similar to Ca in ionic charge and ionic radius and therefore substitutes for Ca in mineral crystal lattices (Salifu et al., 2018). Rb is geochemically different compared to Ca and does therefore not substitute for Ca in the Ca-sulfate crystal lattice. Hence, after crystallization, no radiogenic ^{87}Sr is produced and the initial $^{87}Sr/^{86}Sr$ ratio of Ca-sulfates is preserved. This allows to use the $^{87}Sr/^{86}Sr$ ratio of Ca-sulfate as a proxy to distinguish between the marine and the Andean Ca sources (Rech et al., 2003; Salifu et al., 2018).

1.4. Objectives

Previous work demonstrated the potential of isotope analysis of oxygen, sulfur, and strontium to trace different sulfate sources (e.g., Rech et al., 2003; Bao et al., 2004; Harris et al., 2012; Alexander et al., 2012). The primary objective of this thesis is to investigate the spatial distribution of different sulfate sources and to identify post-depositional processes, like microbial sulfate cycling. To trace biological activity is especially interesting in areas, where life is limited, e.g., due to extremely low water availability. This is especially interesting for areas, where biological activity is limited due to the low water availability. In this thesis, different isotope systems ($\Delta^{17}O_{SO_4}$, $\delta^{18}O_{SO_4}$, $\delta^{34}S_{SO_4}$, and $^{87}Sr/^{86}Sr$) are combined to evaluate the relative contribution of marine, continental, and atmospheric sulfate deposition across the coastal and central regions of the Atacama Desert between 19°S and 25°S. The oxygen isotope composition of sulfates is of particular interest because it can be used to trace biological activity. Under abiotic Earth's surface conditions the oxygen isotopic composition of sulfates is stable and does not undergo any considerable isotope exchange with water. Thus, sulfates' oxygen isotopic composition reflects the initial sulfate source.

Chapter 2 comprises descriptions of the used methods to determine $\Delta^{17}O_{SO_4}$, $\delta^{18}O_{SO_4}$, $\delta^{34}S_{SO_4}$ and $^{87}Sr/^{86}Sr$ of natural samples from the Atacama Desert. For the triple oxygen isotope analysis of the large sample set investigated in this study, a fast and easy-to-use protocol was elaborated. The protocol includes quantitative dissolution of natural sulfate samples, conversion into silver sulfate sufficiently pure for pyrolysis and subsequent $\Delta^{17}O_{SO_4}$ measurements, and a data normalization procedure to ensure the comparability between methods and laboratories. The accuracy and precision of this protocol was proved by analyzing various in-house standards from other laboratories and by re-analyzing an Atacama Desert soil pit which was previously analyzed using the fluorination method (Ewing et al., 2008).

Chapter 3 deals with the results and interpretation of combined sulfur, strontium, and triple oxygen isotope analyses of soil samples in order to identify, map and quantify sulfate source contributions. While the triple oxygen isotope composition is especially useful to identify the atmospheric source contribution, the sulfur isotope composition and strontium isotope ratio trace the redeposition of marine sulfate (Rech et al., 2003). The combination of oxygen and sulfur isotope analyses can help to identify biogenic sulfur gases emitted from the ocean and to

detect biological sulfate cycling. In addition, the potential of $\Delta^{17}O_{SO_4}$ to identify bioactivity and therewith water availability is investigated. In combination with $\delta^{18}O_{SO_4}$ and $\delta^{34}S_{SO_4}$, $\Delta^{17}O_{SO_4}$ might help to detect the spatial extend of extreme long-term hyperaridity in the Atacama Desert.

2.

Methods

2.1. Optimizing Sulfate Pyrolysis Triple Oxygen Isotope Analysis for Samples from Desert Environments

Klipsch, S., Herwartz, D. and Staubwasser, M. (2021) 'Optimizing Sulfate Pyrolysis Triple Oxygen Isotope Analysis for Samples from Desert Environments'. *Rapid Communication of Mass Spectrometry* **35 14** DOI: 10.1002/rcm.9102

2.1.1. Introduction

The triple oxygen isotope composition of sulfate provides information on the formation pathway of sulfate ions (Savarino et al., 2000; Bao, 2015). Sulfate formed in the atmosphere (secondary atmospheric sulfate = SAS) generally reveals a positive mass-independent fractionation signature ($\Delta^{17}O_{SO_4}$) as a result of SO_2 oxidation via ozone or H_2O_2 (Johnston and Thiemens, 1997; Savarino and Thiemens, 1999; Savarino et al., 2000). Changes in the contribution of SAS or variations in atmospheric oxidation capacity are recorded as variable $\Delta^{17}O_{SO_4}$ in sulfates from ice cores (Alexander et al., 2002; Kunasek et al., 2010; Hill-Falkenthal et al., 2013; Walters et al., 2019) or desert soils (Bao et al., 2001b,a, 2004). These records trace the global-scale intra-decadal ENSO climate cycles (Shaheen et al., 2013), and the distribution and biologic cycling of SAS deposition (Johnson et al., 2001). Negative $\Delta^{17}O_{SO_4}$ values are generated via oxidation with O_2 and reveal anomalously high atmospheric pCO_2 in past climatic extremes like Snowball-Earth (Bao et al., 2008; Cao and Bao, 2013) and the corresponding state of the global sulfur cycle (Crockford et al., 2016; Waldeck et al., 2019). In desert environments, triple oxygen isotopes are useful to quantify the distribution of individual sulfate sources (oceanic, volcanic, atmospheric) in space and time, and to identify biological sulfate cycling, which erases $\Delta^{17}O_{SO_4}$ anomalies. The application of this method to Atacama and Namib Desert process

studies was our prime motivation for the present analytical study. Such environmental studies are usually conducted along transects to work out spatial patterns of desert processes or down soil and sediment profiles to reconstruct changes of environmental conditions in the past. Both types of studies require the preparation and analysis of large numbers of samples.

There are a number of challenges to overcome in preparing sulfates from natural samples for triple oxygen isotope analysis and to perform such analyses on large numbers of samples. Water and HCl extracts have been used to leach sulfates from desert soil samples (Bao et al., 2001b,a, 2004). However, water extracts disproportionately dissolve highly soluble sulfate common in the desert environment, e.g., thenardite (Na_2SO_4). Acidic sample dissolution may lead to artifacts caused by oxygen isotope exchange between sulfate and water at low pH (<1) (Rennie and Turchyn, 2014) and may also dissolve unwanted detritus. Impurities, particularly from ^{17}O-anomalous nitrate, must be separated (Bao, 2006). In aerosol studies, this is done by ion chromatography of water extracts (Kunasek et al., 2010; Alexander et al., 2012; Walters et al., 2019), but this is a time-consuming process. The total variability in $\Delta^{17}O_{SO_4}$ observed in the Atacama Desert environment is in the order of 1‰ (Bao, 2006; Ewing et al., 2008; Sun et al., 2018; Klipsch et al., 2021b). As such, the analytical method must be suitable for rapid and automated analyses at sufficient precision; i.e., of the order of 0.1‰. The present study describes an accurate and comparatively easy to use method for large sample sets with sufficient precision to resolve spatial and temporal gradients in desert environments. Consistent accuracy and precision between mass spectrometry sessions are maintained by applying standardized correction procedures as well as simple peak-shape screening and statistical rejection criteria to identify bad measurements.

For the measurement of $\Delta^{17}O_{SO_4}$ values, two methods are in use: (1) laser fluorination (Bao and Thiemens, 2000) and (2) pyrolysis (Savarino et al., 2001). Laser fluorination generates O_2 from >10 µmol of natural sulfate converted to $BaSO_4$ with a precision in $\Delta^{17}O$ of $0.02 - 0.05$‰ (Bao and Thiemens, 2000; Cowie and Johnston, 2016; Waldeck et al., 2019). For smaller sample sizes, e.g., aerosol sulfate from ice cores, the pyrolysis method is used (Alexander et al., 2002; Kunasek et al., 2010; Hill-Falkenthal et al., 2013; Walters et al., 2019). Here, O_2 is generated by pyrolysis of natural samples converted to Ag_2SO_4. After ion chromatographic purification, typical precisions in $\Delta^{17}O_{SO_4}$ for samples between 0.2 and 10 µmol are $0.1 - 0.3$‰ (Savarino

et al., 2001; Schauer et al., 2012; Geng et al., 2013). Improved precision was reported on using gold sample capsules rather than quartz glass vials, where isotopic exchange may occur between the sample and quartz O_2 (Schauer et al., 2012). However, quartz cups have the advantage of being reusable, whereas folded gold capsules are for single-use only.

In addition, there are accuracy requirements to be met when comparing soil samples measured after laser fluorination and pyrolysis. During both methods, fluorination and pyrolysis, a stable oxygen isotope fractionation of variable magnitude occurs – between SO_xF_x and O_2, and between SO_x and O_2, respectively. Due to this fractionation, the absolute δ^xO_{O2} values derived from fluorination or pyrolysis measurements are not representative of the true δ^xO_{SO4} values. Thus, both methods require pairing with independent $\delta^{18}O$ measurements and referencing with standard sulfate material. The correction factor for $\delta^{18}O$ values from fluorination and pyrolysis measurements varies between +9‰ and +23‰ (Bao and Thiemens, 2000; Cowie and Johnston, 2016) and between −6.6‰ and +3.9‰ (see supplementary data Klipsch et al., 2021a), respectively. However, $\Delta^{17}O$ measurements are still possible, because this fractionation follows a mass-dependent relationship and fractionation effects on $\Delta^{17}O$ are negligible (Geng et al., 2013).

Internal method precision is generally better than reproducibility between methods and between laboratories. We compare $\Delta^{17}O$ values measured at the University of Cologne (UoC; this study) with previously measured data from University of Washington (UW) (Schauer et al., 2012; Geng et al., 2013), University of California San Diego (UCSD) (Ewing et al., 2008; Schauer et al., 2012), and Harvard University (HU) (Cowie and Johnston, 2016). The methods used are fluorination (F) and pyrolysis (P), which is further divided into pyrolysis with quartz cups or with gold capsules. In a first step we test for consistency between laboratories using the pyrolysis method. Subsequently, the pyrolysis data is compared with data from the fluorination method to test for consistency between the two methods.

In this study, we present a fast and easy to use protocol for the quantitative dissolution of natural Ca-sulfate samples and conversion into sufficiently pure Ag-sulfate for accurate and precise pyrolysis analyses. To facilitates high sample throughput, the method described by Schauer et al. (2012) was simplified by omitting the ion chromatography or other ion exchange methods (Le Gendre et al., 2017) and only addressing possible contaminations by the major

soil salt anions Cl^- and $NO_3{}^-$. The accuracy of this approach was tested by analyzing various in-house standards from other laboratories. We also reanalyzed an Atacama Desert soil pit previously analyzed by the fluorination method at UCSD (Ewing et al., 2008). The respective results are identical within error and attest to the accuracy of our method for natural samples from desert environments with high Cl^- and $NO_3{}^-$ contents.

Terminology

The oxygen isotope composition of a material is commonly reported relative to an internationally accepted standard in δ notation, which is given by:

$$\delta^{*}\mathrm{O} = \frac{{}^{*}R_{smp}}{{}^{*}R_{std}} - 1, \tag{2.1}$$

where R is the mole ratio of the rare over the abundant isotope ($^{17}O/^{16}O$ or $^{18}O/^{16}O$) in the sample (R_{smp}) and standard material (R_{std}), and x denotes the mass of the respective rare isotope (17 or 18).

In general, differences in the oxygen isotope ratio of matter evolve due to mass-dependent processes resulting in a correlation between $\delta^{17}O$ and $\delta^{18}O$ (Bao et al., 2016; Thiemens, 2013):

$$\delta^{17}\mathrm{O} \approx \lambda \cdot \delta^{18}\mathrm{O}. \tag{2.2}$$

Deviations from this correlation are illustrated by the $\Delta^{17}O$ definition:

$$\Delta^{17}\mathrm{O} = \delta^{17}\mathrm{O} - \lambda \cdot \delta^{18}\mathrm{O}. \tag{2.3}$$

In this study, the traditional definition of $\Delta^{17}O$ is used with $\lambda = 0.52$, which is a reasonable average value for terrestrial materials (Matsuhisa et al., 1978) and is commonly used when dealing with large mass-independent fractionation effects ($> 0.1‰$) (Savarino et al., 2001; Alexander et al., 2002; Kunasek et al., 2010; Schauer et al., 2012; Geng et al., 2013; Walters et al., 2019). Other definitions of $\Delta^{17}O$ result in slightly different numerical values, but these are not resolvable with the precision obtained in this study. These definitions are mainly used

in studies aiming to resolve small, purely mass-dependent variations in $\Delta^{17}O$ (Herwartz, 2021; Surma et al., 2021; Voigt et al., 2021).

2.1.2. Experimental

Sample Dissolution and Conversion into Silver Sulfate

The entire analytical procedure comprises quantitative leaching of sulfate from soil or geologic samples, conversion into Ag-sulfate, removal of residual mayor anions – particularly chloride and nitrate, drying, and pyrolysis continuous flow mass spectrometry of sample O_2 gas. The Atacama Desert soil samples are dominated by gypsum and anhydrite with minor amounts of halite (NaCl), nitratine ($NaNO_3$), and thenardite (Na_2SO_4) (Voigt et al., 2020). This method does not consider contaminations with organic matter (e.g., Xie et al., 2016), because the total organic carbon content of Atacama Desert soils is generally low (<0.2 wt% Mörchen et al., 2019).

To dissolve natural Na- and Ca-sulfate at neutral pH, 7.5 mL H_2O was mixed with a 1 mL slurry of cation resin in Na^+ form (AG 50W X8, 200–400 mesh, Bio-Rad, Hercules, CA, USA) and 100 mg Ca-sulfate overnight (Frenkel et al., 1986). This amount equals 100 to 250 mg of natural Atacama sample material, dependent on the sulfate concentration. Due to a higher absorption coefficient, Ca^{2+} exchanges with Na^+ on the resin, leaving only Na^+, $SO_4{}^{2-}$, and all other anions in solution (Frenkel et al., 1986). The mixture was centrifuged, and the supernatant pipetted off. Subsequently, Na^+ was exchanged with Ag^+ using the cation resin in Ag^+ form (following Schauer et al., 2012). One mL of resin in a column may be transferred into Ag^+ form using 42 mL of 25 mM Ag_2SO_4 solution, followed by 20 mL H_2O to rinse out all $SO_4{}^{2-}$. To further minimize the risk of $SO_4{}^{2-}$ contamination, a Ag_2NO_3 solution may be used as an alternative. We verified the absence of $SO_4{}^{2-}$ from the conditioning by analyzing eluted water from the final water rinse step by inductively coupled plasma optical emission spectrometry (SPECTRO ARCOS ICP-OES; SPECTRO Analytical Instruments GmbH, Kleve, Germany). A similar procedure would have to be performed for $NO_3{}^-$. Columns were then loaded in three repeating steps, each with 1 mL of 0.1 M Na_2SO_4 sample solution, followed by 2 mL H_2O, to prevent clogging of the column tip by Ag_2SO_4 precipitation. A final rinse of 5 mL H_2O was applied to completely flush out the sulfate sample. Contaminations with Cl^- were removed from

the sample as it precipitated on the resin as AgCl. ICP-OES measurements were conducted on the final Ag-sulfate from eight natural samples to verify the purity (see supplementary data Klipsch et al., 2021a). Working with higher sample Na_2SO_4 concentrations leads to incomplete cation exchange and consequently to surplus sodium in the final Ag_2SO_4 sample, which result in several minutes long peaks with low amplitudes during mass spectrometry. The whole elute solution, in total 14 mL, was collected as an Ag_2SO_4 sample solution. Each sample exchanged about 30% of Ag^+ on the resin. The resin was regenerated after each sample to prevent cross-contamination. The Ag_2SO_4 samples were dried in a vacuum centrifuge (Concentrator plus, Eppendorf, Hamburg, Germany) at 30 °C over night. Finally, the solid Ag_2SO_4 precipitate was leached three times with 50 µL H_2O to remove any $AgNO_3$. The leaching was conducted by mixing 50 µL H_2O with the Ag-sulfate crystals. After all the crystals had settled, the solution was pipetted off. One leaching step with 50 µL H_2O removes up to 0.65 mmol $AgNO_3$ (= 111 mg; solubility: 2220 g L^{-1} at 20 °C (Willmes, 1993)) and a maximum of 1.3 µmol Ag_2SO_4 (= 0.41 mg; solubility: 8.3 g L^{-1} at 25 °C (Seidell and Linke, 1919)). This step is critical for natural samples that may also contain nitrate salts with a distinct $\Delta^{17}O$ signature up to 30‰ (Michalski et al., 2004; Bao, 2006). The described protocol forms $200 - 300$ µmol Ag_2SO_4. A fraction of the dry Ag_2SO_4 (about 30 µmol) was then weighed into quartz cups or gold capsules using a high-precision balance (resolution: 1 µg; Sartorius MC21S, Sartorius AG, Göttingen, Germany) for subsequent pyrolysis and isotope ratio measurements.

Standard Materials

In absence of certified $\Delta^{17}O$ reference Na- or Ca-sulfate material, we compared a number of in-house standards from different laboratories. Three non-zero $\Delta^{17}O_{SO_4}$ in-house sulfate standards (UoC-α, UoC-β, and UoC-ϵ) were produced by equilibrating 12.5 g sodium sulfite (Na_2SO_3, Sigma-Aldrich, St. Louis, MO, USA) with 100 mL water (following Schauer et al., 2012). The water was enriched in ^{17}O by first diluting 70% ^{17}O water (purchased from Cambridge Isotope Laboratories, Andover, MA, USA) by 1:50000. Secondly, 3.6 mL, 7.5 mL, and 25 mL of this diluted ^{17}O enriched water were mixed with the corresponding amount of 18 MΩ water to get 100 mL, respectively. After equilibrating Na_2SO_3 with the ^{17}O enriched water for 24 h, a volume of 10 mL 30% H_2O_2 was added to each solution to oxidize Na_2SO_3 to sodium

sulfate (Na_2SO_4). Subsequently, the Na_2SO_4 solutions were dried down in an oven at 60 ℃ for about 10 days. In addition, pure Ag-sulfate ($\geq$ 98.5%, VWR, Radnor, PA, USA) is used as a zero-$\Delta^{17}O_{SO_4}$ in-house standard, labeled UoC-zero.

Three laboratory internal Na_2SO_4 standards (Sulf-α, Sulf-β, and Sulf-ϵ) were provided by B. Alexander from the University of Washington (UW), where they were previously analyzed by pyrolysis with quartz and gold sample containers (Schauer et al., 2012; Geng et al., 2013). These samples were also analyzed at the University of California San Diego (UCSD) by pyrolysis with quartz sample cups (Schauer et al., 2012) along with a lab internal Ag_2SO_4 standard (MT) provided to us by M. Thiemens. In addition, an internal standard JMG ($CaSO_4 \cdot xH_2O$) was supplied by D. Johnston from Harvard University (HU) (Cowie and Johnston, 2016). All the $\Delta^{17}O$ results obtained for Sulf-α, Sulf-β, Sulf-ϵ, MT, and JMG are listed in Table 2.2 and Table 2.3.

To report the reference gas and data in general relative to VSMOW (Vienna Standard Mean Ocean Water), each laboratory uses its own normalization procedure. By calibrating their method to known silicate standards, Cowie and Johnston (2016) are able to report high-precision fluorination triple oxygen data relative to VSMOW. Schauer et al. (2012) normalized the quartz pyrolysis raw data to raw gold capsules data which are assumed to be free from exchange with quartz and, therefore, presumed to be on the VSMOW scale ($\Delta^{17}O_{VSMOW}(P)$). For practical reasons, in this study, the pyrolysis raw data are first normalized to this $\Delta^{17}O_{VSMOW}(P)$ scale defined by gold capsules data from Schauer et al. (2012) (see subsection 2.1.3). To reveal whether the raw data from gold capsules pyrolysis analyses are indeed free of detectable exchange with quartz and, therefore, suitable for normalizing to VSMOW, the data are compared with VSMOW-scaled fluorination data ($\Delta^{17}O_{VSMOW}(F)$) from UCSD and HU. The details of these protocols are not described but significant systematic errors should show up in the comparison of the $\Delta^{17}O_{VSMOW}(P)$ and $\Delta^{17}O_{VSMOW}(F)$ scales unless all normalizing procedures result in an identical offset from the true VSMOW scale.

Pyrolysis and Measurement

The pyrolysis was conducted as described in Schauer et al. (2012) with minor modifications. The Ag_2SO_4 pyrolysis system at the UoC outlined in Figure 2.1 mainly consists of (1) a reactor

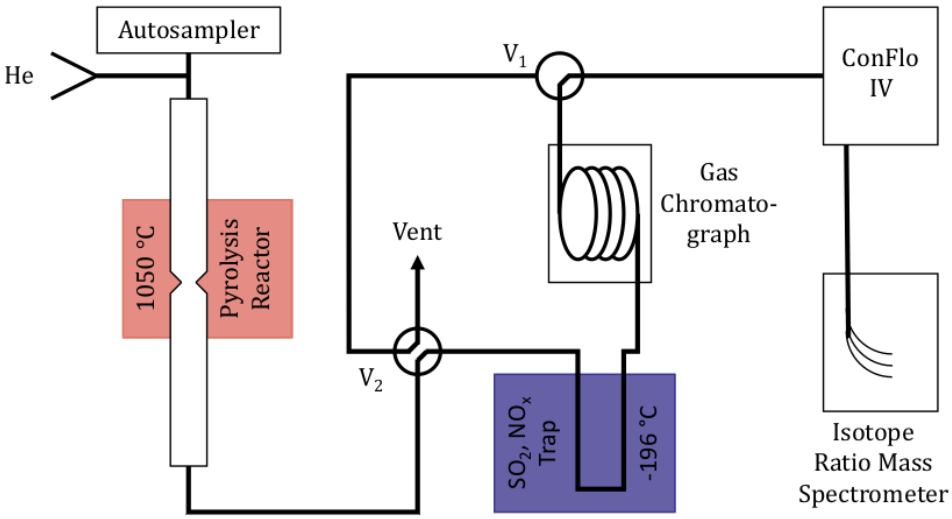

Figure 2.1.: Flow path diagram of the UoC silver sulfate pyrolysis system which consists of an autosampler, a pyrolysis reactor, a cold trap, a gas chromatograph (1.5 m column packed with 5 Å molecular sieve), a ConFlo interface and an isotope ratio mass spectrometer. To flush the gas chromatograph and the cold trap the He flow is redirected by turning the valves (V_1 and V_2).

furnace, (2) a condensation trap, (3) a 1.5 m gas chromatography (GC) column, (4) an open split interface, and (5) an isotope ratio mass spectrometer (MAT 253, Thermo Fisher Scientific, Waltham, MA, USA).

About 30 µmol of the Ag_2SO_4 sample was loaded into a sample container made of (1) custom-made quartz cups (5 or 9 mm tall, 5 mm outer diameter, 1 mm wall thickness, Ullrich Laborbedarf, Bonn, Germany) or (2) custom-made gold capsules (12 mm tall, 5 mm outer diameter, ESG Edelmetall-Service, Rheinstetten, Germany). The sample containers were loaded into a He-purged autosampler (zero blank Vector SAS, 80 positions, EuroVector, Pavia, Italy) and successively dropped into the pyrolysis reactor. With this particular autosampler design, a sample vial first drops from the 80-position wheel into a cavity within a moving cylinder, which subsequently pushes the sample over the hot reactor tube. The reactor tube is an empty custom-made quartz glass tube with a diameter restriction to catch the sample containers within the hot zone of the furnace (Schauer et al., 2012). This quartz tube rests vertically in an EA furnace (Euro EA 3000, EuroVector, Pavia, Italy), which was heated to 1050 °C. The

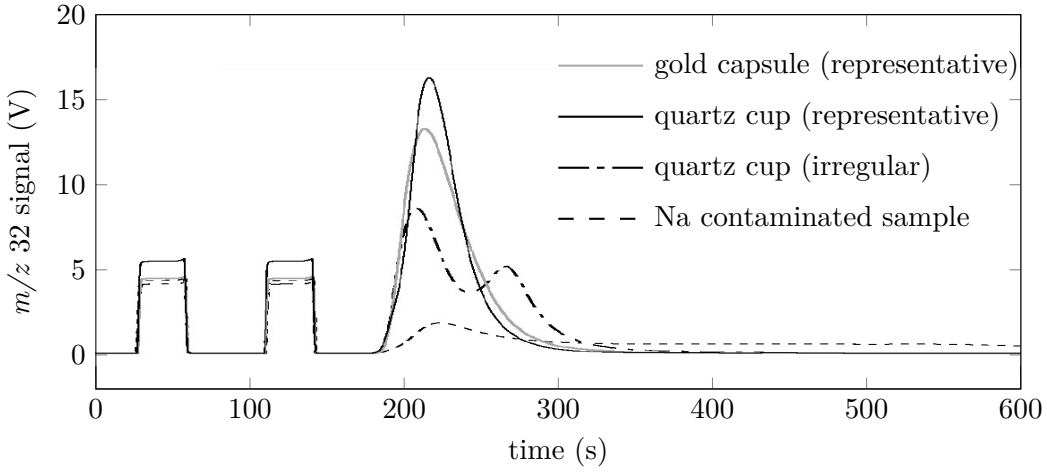

Figure 2.2.: The *m/z* 32 measurement sequences shown here are representative for measurement with quartz cups (black solid line) and gold capsules (gray solid line). Irregular peak shapes (black dashed-dotted line) were observed in 6.5% of the measurements. In addition, a sequence of Ag_2SO_4 samples contaminated with sodium is shown (dashed line). All peaks are normalized to the same sample introduction time.

pyrolysis of Ag_2SO_4 in the reactor tube can be described by the following equation (Savarino et al., 2001):

$$Ag_2SO_4\,(s) \xrightarrow{1050\ ^\circ C} O_2\,(g) + SO_2\,(g) + 2Ag\,(s) + SO_3\,(\text{trace}) \tag{2.4}$$

All gaseous reaction products are transported by He with a flow rate of about 120 mL min^{-1} through a cold trap held at −196 °C with liquid N_2 to remove SO_2 and SO_3. Afterwards, trace amounts of N_2, CO, or other gases were separated from the O_2 sample gas with a 1.5 m GC column packed with 5 Å molecular sieve at room temperature. Subsequently, the sample O_2 gas is introduced into the mass spectrometer via an open split interface (ConFlo IV, Thermo Fisher Scientific, Waltham, MA, USA). Isotope ratios of sample O_2 are determined by comparison with reference O_2 gas and by measuring *m/z* 32, 33, and 34 of respective reference and sample O_2 peaks. Typical measuring sequences are shown in Figure 2.2.

The peak areas of the sample gas were compared with the peak areas of the working reference O_2 gas that was introduced through the ConFlo IV interface twice prior to the sample peak. The raw $\delta^{x}O$ values were calculated relative to the second reference peak. A blank correction,

as described by Geng et al. (2013), was not required since our sample sizes were more than an order of magnitude larger.

Irregular peak shapes and tailing, as already described by Schauer et al. (2012), were observed in 6.5% of the measurements, resulting in poor precision and accuracy. There are two principal sources for imperfect peaks. Chemical impurities, such as Na contamination, can alter peak shapes, as shown in Figure 2.2. However, irregular peak shapes are also observed for pure Ag_2SO_4 samples. In our setup, the open-top quartz cup falls into the reactor tube in an uncontrolled manner. We suspect that irregular peak shapes are probably caused by delayed pyrolysis of sample material scattered from the sample cup when dropping into the reactor. Irregular peak shapes were not observed during gold capsules measurements, probably because gold capsules fully enclose the sample material. Even when excluding Na-contaminated samples, results from irregular peak shapes deviate considerably in $\Delta^{17}O_{VSMOW}(P)$ of $0.24 \pm 0.28‰$ from the mean value of regular peak-shaped measurements of the respective sample. Therefore, these analyses were excluded from the results.

Over the course of this study, two additional sources for erratic errors have been encountered. First, the sample introduction mechanism of the autosampler involves a step where the sample vial falls into a cavity within a moving cylinder. When open-top quartz cups are used, small quantities of Ag_2SO_4 may be spilled into the cavity which leads to possible cross-contamination. Over the long term the spilled Ag_2SO_4 powder abrades the rubber seals of the moving cylinder, resulting in leakage, and an irregular He flow. Thorough cleaning of the autosampler after each analytical session as well as the use of taller quartz cups (9 mm instead of 5 mm) significantly reduced but did not fully remove this problem. An alternative zero blank autosampler design is required to completely prevent this and would probably result in a significant better reproducibility. Secondly, minor amounts of SO_2 may leak through the liquid N_2 trap into the gas chromatograph and eventually through the gas chromatograph into the mass spectrometer causing interferences on m/z 33, due to doubly charged SO_2 molecules with mass 66, e.g., $^{32}S^{16}O^{18}O$, $^{33}S^{16}O^{17}O$, or $^{34}S^{16}O^{16}O$. Therefore, the gas chromatograph was heated to 130 ℃ and the He flow was redirected by turning the valves V_1 and V_2 (Figure 2.1) overnight between each analytical session.

An analytical session comprises a maximum of 21 samples including three calibration sets, which consists of two to three external or in-house standards, in the beginning, the middle, and the end of one session. We determined that sample vials move out of the hot zone of the furnace after 25 samples have been introduced, indicated by later occurring, and smeared-out sample peaks with lower amplitudes.

2.1.3. Results and Discussion

Normalizing Procedure and Data Treatment

As is common practice, we normalize our $\Delta^{17}O_{raw}$ values to the $\Delta^{17}O_{VSMOW}(P)$ scale by scaling and shifting the data of each analytical session to sulfate standards – external or in-house – with known $\Delta^{17}O_{VSMOW}(P)$ values according to the following equation (Meier-Augenstein and Schimmelmann, 2019):

$$\Delta^{17}O_{VSMOW}(P) = s \cdot \Delta^{17}O_{raw} + b, \tag{2.5}$$

where the scaling factor (slope) $s = (RM2_{accepted} - RM1_{accepted})/(RM2_{measured} - RM1_{measured})$ and the shifting value (intercept) $b = RM1_{accepted} - (s \cdot RM1_{measured}) = RM2_{accepted} - (s \cdot RM2_{measured})$. To calibrate our in-house standards, the external standards Sulf-α ($\Delta^{17}O_{VSMOW}(P) = 0.9‰$; Schauer et al., 2012) and Sulf-ϵ ($\Delta^{17}O_{VSMOW}(P) = 7.0‰$; Schauer et al., 2012) are used as reference material $RM1_{accepted}$ and $RM2_{accepted}$, respectively. Subsequently, our in-house sulfate standards, as listed in Table 2.1, were used as internal reference material. Because most natural samples had rather low $\Delta^{17}O$ values, the in-house standards UoC-zero ($\Delta^{17}O_{VSMOW}(P) = -0.06‰$) and UoC-$\beta$ ($\Delta^{17}O_{VSMOW}(P) = 1.90‰$) were generally used for normalizing purposes. The external reproducibility and accuracy were monitored by repeated measurements of standards as unknowns.

The average correction for our quartz data to our gold data (Equation 2.6) from this study is comparable with a correction previously published by Schauer et al. (2012) (Equation 2.7):

$$\Delta^{17}O_{gold} = 1.17 \cdot \Delta^{17}O_{quartz} - 0.07, \tag{2.6}$$

$$\Delta^{17}O_{gold} = 1.14 \cdot \Delta^{17}O_{quartz} + 0.06, \tag{2.7}$$

However, the scaling factors and shifting values varied significantly between individual analytical sessions (Figure 2.3). Hence, a universal equation to correct all quartz data is not ideal and data should be normalized separately for each individual session.

The scaling factors >1 show that the raw values are contracted relative to the $\Delta^{17}O_{VSMOW}(P)$ scale. The contraction is generally interpreted to reflect oxygen isotope exchange between quartz cups and the evolved sample O_2 (Schauer et al., 2012). One aspect that probably influences the scaling factor is degradation of the reactor tube. Generally, we observed increasing scaling factors with the number of analytical sessions performed with the same reactor tube. A possible explanation was offered by Schauer et al. (2012). The use of quartz cups during the pyrolysis of Ag_2SO_4 may cause etching on the side-walls of the reactor tube, which could increase the isotopic exchange rate of sample oxygen with the reactor walls. In addition, elementary silver – a reduction product of the pyrolysis – on the walls of the reactor tube may interact with sample O_2. Finally, sample material could scatter from the open quartz cups and coat the reactor wall, thereby introducing memory. Measurements conducted with gold capsules, which more fully enclose the sample material, are less prone to high scaling factors. The possible oxygen isotope exchange with the reactor tube becomes increasingly significant with decreasing sample size (Geng et al., 2013). Nevertheless, we demonstrate that analyses of about 30 µmol sample

Table 2.1.: List of $\Delta^{17}O_{raw}$ and respective $\Delta^{17}O_{VSMOW}(P)$ values of our in-house standards UoC-zero, UoC-α, UoC-β, and UoC-ϵ measured with quartz cups. The $\Delta^{17}O_{VSMOW}(P)$ values were calculated after Equation 2.5 with Sulf-α $\Delta^{17}O_{VSMOW}(P) = 0.9‰$ (Schauer et al., 2012) and Sulf-ϵ $\Delta^{17}O_{VSMOW}(P) = 7.0‰$ (Schauer et al., 2012) as reference material $RM1_{measured}$ and $RM2_{measured}$, respectively. Errors depict 1σ standard deviation.

	$\Delta^{17}O_{raw}$ (‰)	$\Delta^{17}O_{VSMOW}(P)$ (‰)	n
UoC-zero	0.06 ± 0.13	-0.06 ± 0.15	31
UoC-α	0.82 ± 0.12	0.77 ± 0.12	13
UoC-β	1.81 ± 0.08	1.90 ± 0.09	20
UoC-ϵ	5.22 ± 0.20	5.69 ± 0.26	10

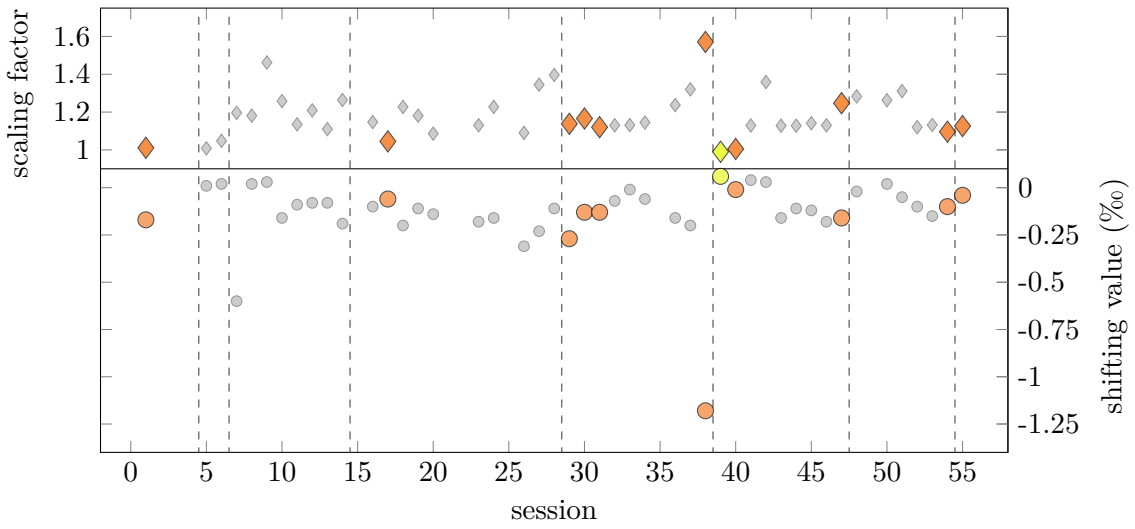

Figure 2.3.: Scaling factors (diamonds) and shifting values (dots) vary significantly between each analytical session. Reactor tube exchanges are indicated by dashed lines. The correction parameters for session 38 are so high because the session was conducted with a heavily used reactor tube with etched walls and silver probably interacting with the sample O_2. In addition, the calibration standards of session 38 show a large 1σ in $\Delta^{17}O_{raw}$ (Figure 2.4) indicating a low reliability of the correction of this session.

material performed with quartz cups may reach a similar internal precision to measurements conducted with gold capsules (Figure 2.4).

High scaling factors are an indicator for large systematic errors. However, as long as the 1σ standard deviations in $\Delta^{17}O_{raw}$ of the calibration standards remain small, the analytical session is stable enough for correction by the normalizing procedure described above. Session stability can be evaluated by the Z-score of its scaling factor and its 1σ in $\Delta^{17}O_{raw}$ of the calibration standards. A Z-score is defined by the deviation of a certain value ($= x_i$) from the mean ($= x_m$) divided by the standard deviation ($= \sigma$) ($= (x_i - x_m)/\sigma$) (Kreyszig, 2006).

Z-scores based on a total of 45 analytical sessions conducted with quartz cups were used. As shown in Figure 2.4, sessions conducted with quartz cups are comparable with results from a session comprising only gold capsule measurements.

External reproducibility was significantly improved by rejecting data based on three criteria. First, all measurements with an irregular peak shape were excluded (7% of all data) improving the reproducibility from 0.20‰ to 0.17‰. Second, data from one sample that differed more than 0.52‰ (3σ reproducibility) in $\Delta^{17}O_{VSMOW}(P)$ from the daily mean was discarded as

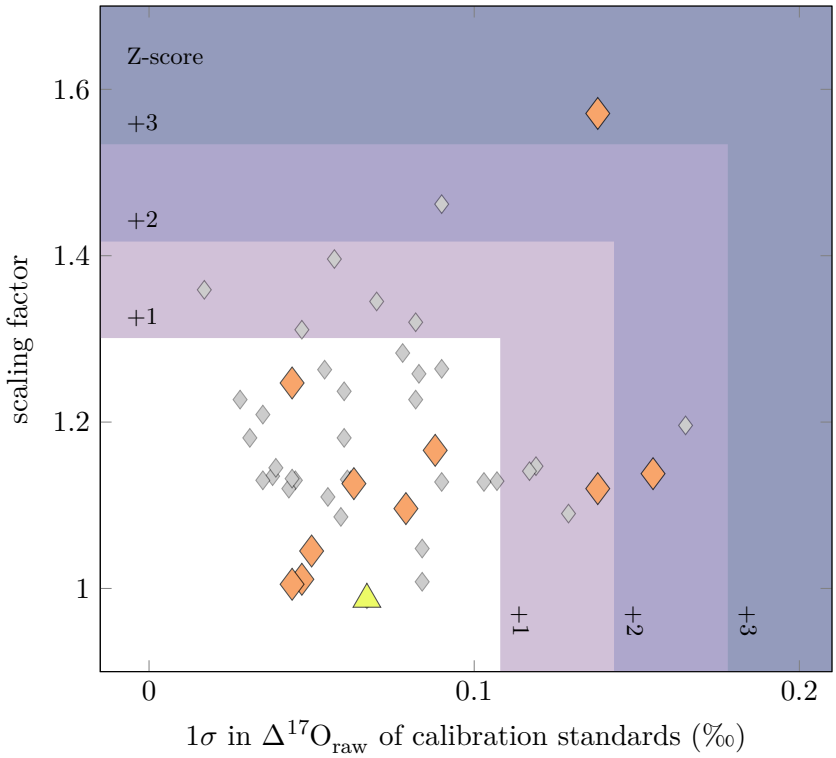

Figure 2.4.: The scaling factors and 1σ in $\Delta^{17}O_{raw}$ of calibration standards of analytical sessions from this study are shown by large colored symbols. Measurements conducted with quartz cups (diamonds) may reach similar low scaling factors and 1σ in $\Delta^{17}O_{raw}$ of calibration standards to those of measurements conducted with gold capsules (yellow triangle). Data can be rejected based on the Z-score of the scaling factor and the 1σ in $\Delta^{17}O_{raw}$ of calibration standards. Z-scores were calculated based on 45 analytical sessions conducted with quartz cups (small gray and large orange diamonds). In this study, analytical sessions showing scaling factors or 1σ in $\Delta^{17}O_{raw}$ of calibration standards with Z-scores >3 were rejected.

outlier (for n $\geq$ 3; 0.5% of all data). Third, data with anomalously high scaling factors and large 1σ in the $\Delta^{17}O_{raw}$ values of the calibration standards were rejected based on their Z-scores (Figure 2.4). In this study, analytical sessions showing scaling factors or 1σ in $\Delta^{17}O_{raw}$ of calibration standards with Z-scores >3 were rejected (Figure 4; 9% of all data). The weighted mean of all 1σ standard deviations of samples measured in multiple analytical sessions is used as 1σ SD external reproducibility = 0.12‰. Using different rejection criteria does not significantly change the precision. When using a Z-score of 2 or 1, the 1σ SD external reproducibility becomes 0.10‰ and 0.09‰, respectively, but as much as 27% and 39% of the data set is then excluded. The accuracy estimated by the root mean square error of our data from Sulf-α, Sulf-β, Sulf-ϵ, MT, and JMG compared with the published $\Delta^{17}O$ values (listed in Table 2.2 and Table 2.3) was also improved from 0.26‰ to 0.12‰ by applying the described rejection criteria.

Sample Size

Tests of variable sample sizes within one analytical session revealed substantial increases in $\Delta^{17}O_{raw}$ values with decreasing sample size (Figure 2.5). To minimize uncertainties, the sample size was held constant to about 30 µmol of Ag_2SO_4 with variations of 4.7 $\pm$ 3.7% within each analytical session. The results were normalized to internal standards individually for each analytical session. The normalizing procedure of scaling and shifting described above offers a reproducible way to account for systematic errors associated to differing sample size or variable blanks and backgrounds between analytical sessions.

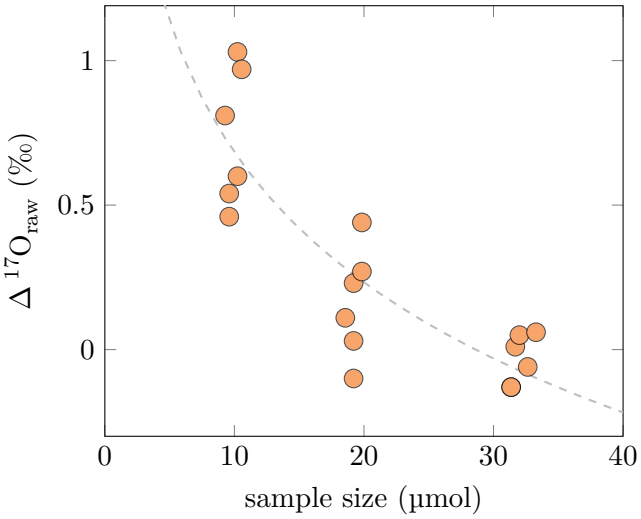

Figure 2.5.: $\Delta^{17}O_{raw}$ values increase with decreasing sample size. $\Delta^{17}O_{raw}$ values of different quantities of the in-house standard UoC-zero, shown here, were measured within one analytical session. For material with $\Delta^{17}O \neq 0$, the shown sample size effect might look different.

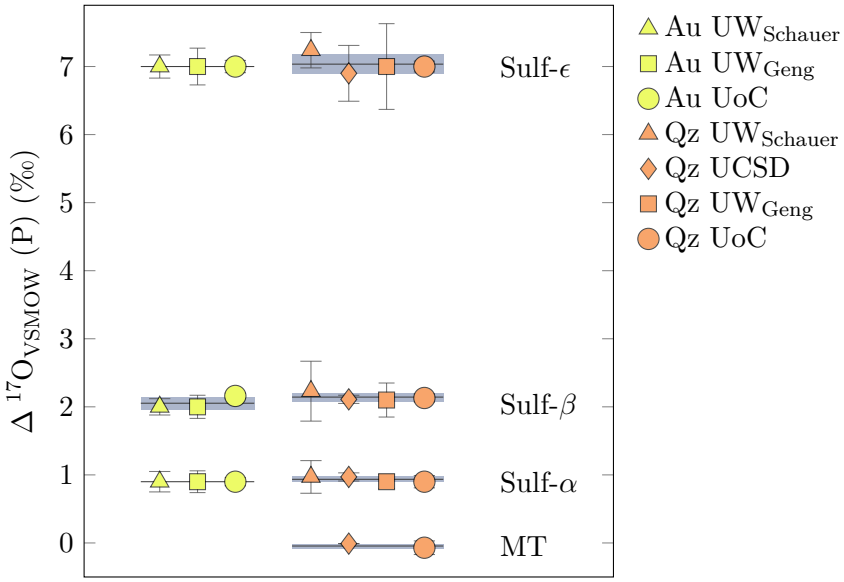

Figure 2.6.: $\Delta^{17}O_{VSMOW}$(P) values of Sulf-α, Sulf-β, Sulf-ϵ, and MT were measured at UCSD (personal communication; Schauer et al., 2012), UW (Schauer et al., 2012; Geng et al., 2013), and UoC with quartz cups (orange symbols) and gold capsules (yellow symbols). All $\Delta^{17}O_{VSMOW}$(P) values are identical within analytical uncertainty for both quartz cups and gold capsule measurements. All error bars show 1σ standard deviation. Mean values of the results from all laboratories are shown by dark lines; shaded areas indicate 1σ standard deviation of the respective sample and vial material (gold or quartz).

Inter Laboratory Comparison of the Pyrolysis Method

The first step in our inter-laboratory comparison was to test for consistency between laboratories using the pyrolysis method by normalizing all pyrolysis data to the same scale defined by gold pyrolysis analyses of Schauer et al. (2012) ($\Delta^{17}O_{VSMOW}$(P) scale). All $\Delta^{17}O_{raw}$ and $\Delta^{17}O_{VSMOW}$(P) values of Sulf-α, Sulf-β, Sulf-ϵ, and MT measured at UW (Schauer et al., 2012; Geng et al., 2013), UCSD (personal communication; Schauer et al., 2012), and UoC are listed in Table 2.2 and plotted in Figure 2.6.

Variations in $\Delta^{17}O_{raw}$ between laboratories become distinct at high $\Delta^{17}O$ for measurements conducted with both quartz cups and gold capsules (Table 2.2). However, the normalized $\Delta^{17}O_{VSMOW}$(P) values of Sulf-α, Sulf-β, Sulf-ϵ, and MT are identical within analytical uncertainty between laboratories and sample containers used (quartz cups and gold capsules; Figure 2.6). The normalizing procedure used in this study corrects for systematic

Table 2.2.: List of all $\Delta^{17}O_{raw}$ and respective $\Delta^{17}O_{VSMOW}(P)$ values of Sulf-α, Sulf-β, Sulf-ϵ, and MT measured at UW (Schauer et al., 2012; Geng et al., 2013), UCSD (personal communication; Schauer et al., 2012), and UoC (this study) with quartz cups and gold capsules. The $\Delta^{17}O_{VSMOW}(P)$ values of Sulf-α, Sulf-β, and Sulf-ϵ were calculated after Equation 2.5 with Sulf-α $\Delta^{17}O_{VSMOW}(P) = 0.9‰$ and Sulf-ϵ $\Delta^{17}O_{VSMOW}(P) = 7.0‰$ (Schauer et al., 2012) as reference material $RM1_{accepted}$ and $RM2_{accepted}$, respectively. For MT, UoC-zero and UoC-β were used for normalization purposes as listed in Table 2.1. Errors depict 1σ standard deviation.

		Quartz			Gold			
		$\Delta^{17}O_{raw}$ (‰)	$\Delta^{17}O_{VSMOW}(P)$ (‰)	n	$\Delta^{17}O_{raw}$ (‰)	$\Delta^{17}O_{VSMOW}(P)$ (‰)	n	Reference
Sulf-α	UW	0.8 ± 0.21	0.97 ± 0.24[a]	11		0.9 ± 0.15	11	Schauer et al. (2012)
	UCSD	0.8 ± 0.05	0.97 ± 0.06[a]	3				Schauer et al. (2012)
	UW	0.90 ± 0.09	0.90 ± 0.10	41	0.8 ± 0.14	0.9 ± 0.16	9	Geng et al. (2013)
	UoC	0.99 ± 0.12	0.90 ± 0.09[b]	9	0.98 ± 0.06	0.90 ± 0.06[b]	5	
Sulf-β	UW	1.9 ± 0.39	2.23 ± 0.44[a]	11		2.0 ± 0.12	10	Schauer et al. (2012)
	UCSD	1.8 ± 0.05	2.11 ± 0.06[a]	3				Schauer et al. (2012)
	UW	2.0 ± 0.23	2.1 ± 0.25	34	1.9 ± 0.15	2.0 ± 0.17	4	Geng et al. (2013)
	UoC	2.09 ± 0.13	2.14 ± 0.06[b]	8	2.25 ± 0.05	2.16 ± 0.04[b]	5	
Sulf-ϵ	UW	6.3 ± 0.23	7.24 ± 0.26[a]	21		7.0 ± 0.17	10	Schauer et al. (2012)
	UCSD	6.0 ± 0.36	6.9 ± 0.41[a]	6				Schauer et al. (2012)
	UW	6.6 ± 0.60	7.0 ± 0.63	43	6.4 ± 0.25	7.0 ± 0.27	7	Geng et al. (2013)
	UoC	6.46 ± 0.43	7.00 ± 0.16[b]	8	7.16 ± 0.09	7.00 ± 0.09[b]	5	
MT	UCSD		-0.06	n.a.				pers. comm. Mark Thiemens
	UoC	-0.02 ± 0.07	-0.07 ± 0.10[b]	4				

[a] calculated after Equation 2.7
[b] calculated after Equation 2.5

errors resulting in a considerably higher external reproducibility for analyses with both quartz cups and gold capsules, especially when applied on a day-to-day basis. We recommend scaling and shifting the data of each analytical session to standards with known $\Delta^{17}O_{VSMOW}(P)$ values using Equation 2.5.

Inter laboratory comparison between pyrolysis and fluorination methods

To compare the $\Delta^{17}O$ pyrolysis results with the fluorination method, we analyzed the internal standard JMG from HU (Cowie and Johnston, 2016) and natural samples from a soil pit (24°06.794′ S, 70°00.396′ W, Yungay, Atacama Desert, Chile) previously analyzed by laser fluorination at UCSD and published by Ewing et al. (2008) (Table 2.3; Figure 2.7). The two natural sample sets were taken from the same locality but different depths (Figure 2.7) and analyzed by two different methods in two different laboratories. All the pyrolysis results and previously published fluorination data are listed in Table 2.3 and shown in Figure 2.7.

The pyrolysis results from this study are in good agreement with previously published fluorination data. The average variation is -0.02 ± 0.08‰ between $\Delta^{17}O_{VSMOW}(P)$ and $\Delta^{17}O_{VSMOW}(F)$, well within analytical uncertainty. Although some inter-sample variability may be expected between the two Atacama Desert soil pit sample sets due to possible intra-soil heterogeneity in $\Delta^{17}O$ and alteration over time, the maximum difference between two samples from the same depth is 0.14‰ (at 95 ±1 cm). Our pyrolysis data confirm positive and constant $\Delta^{17}O$ values throughout the soil profile of $\Delta^{17}O_{VSMOW}(F) = 0.52 \pm 0.06$‰ (Ewing et al., 2008) and $\Delta^{17}O_{VSMOW}(P) = 0.51 \pm 0.06$‰ (Figure 2.7). Three of the natural samples were initially measured with a smaller sample size than the respective calibration standards and corrected using the curve shown in Figure 2.5 (see supporting information of Klipsch et al., 2021a). The sample-size-corrected $\Delta^{17}O$ values are still in good agreement with respective $\Delta^{17}O_{VSMOW}(P)$ values (Figure 2.5). However, as samples with $\Delta^{17}O \neq 0$‰ may follow a somewhat different curve from the one shown in Figure 2.5, such a sample-size correction is not recommended and should best be avoided by maintaining constant sample sizes within an analytical session.

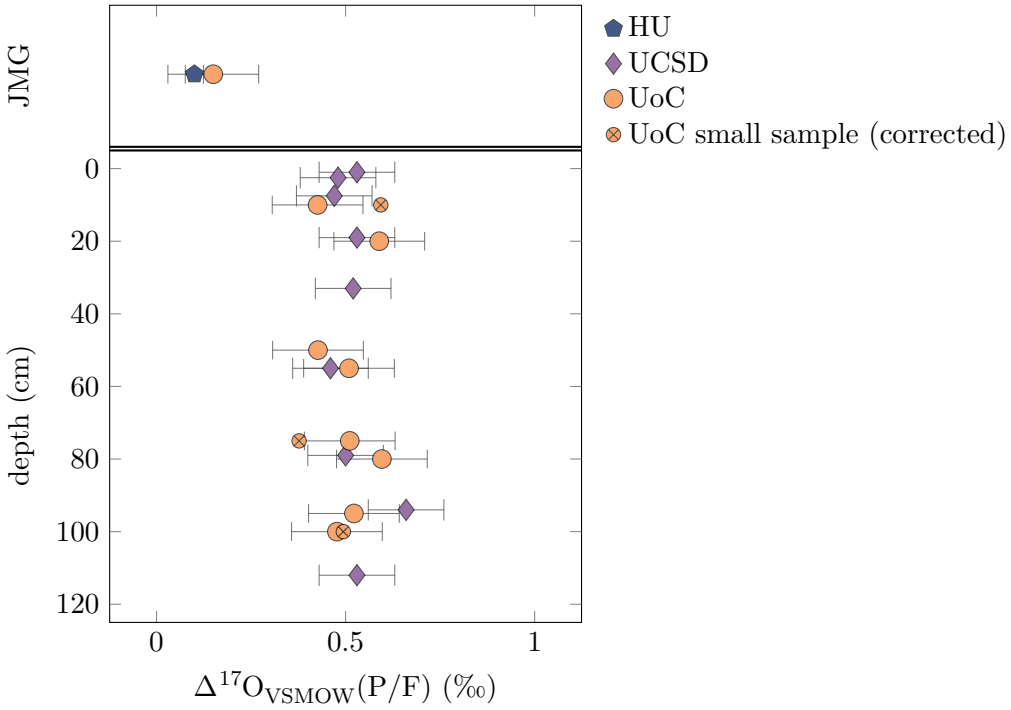

Figure 2.7.: Mean $\Delta^{17}O_{VSMOW}$(P) values of JMG are in good agreement with previously published $\Delta^{17}O_{VSMOW}$(F) values from HU (dark pentagon) (upper panel). $\Delta^{17}O$ values of the Atacama Desert soil profile (lower panel) are uniform with average $\Delta^{17}O_{VSMOW}(F) = 0.52 \pm 0.06‰$ (Ewing et al., 2008) and $\Delta^{17}O_{VSMOW}(P) = 0.51 \pm 0.06‰$, respectively. Shown are published fluorination data measured at UCSD (diamonds) and pyrolysis data measured at UoC (orange dots; this study). All data are identical within analytical uncertainty. All errors show 1σ external reproducibility. Three samples were additionally measured with a smaller sample size and subsequently corrected based on data shown in Figure 2.5 (crossed dots). Error bars for respective samples are not shown.

Table 2.3.: List of $\Delta^{17}O_{raw}$, respective normalized $\Delta^{17}O_{VSMOW}(P)$, and $\Delta^{17}O_{VSMOW}(F)$ values. The natural Atacama samples were measured at UCSD, previously published by Ewing et al. (2008). To compare $\Delta^{17}O$ values of samples from different depths (variations >1 cm), literature $\Delta^{17}O$ values of samples above and below the certain sampling depth were interpolated (values in italic). All $\Delta^{17}O_{VSMOW}(P)$ values were calculated using UoC-zero and UoC-β as listed in Table 2.1 for normalization purposes. All errors depict 1σ external reproducibility.

	Pyrolysis at UoC			Fluorination at HU	at UCSD	
	$\Delta^{17}O_{raw}$ (‰)	$\Delta^{17}O_{VSMOW}(P)$ (‰)	n	$\Delta^{17}O_{VSMOW}(F)$ (‰)	$\Delta^{17}O_{VSMOW}(F)$ (‰)	n
JMG	0.21 ± 0.12	0.15 ± 0.12	6	0.10 ± 0.02[a]		38
Yungay 7.5cm					0.47 ± 0.10	n.a.
Yungay 10cm	0.48 ± 0.12	0.43 ± 0.12	2		*0.48*	
Yungay 19cm					0.53 ± 0.10	n.a.
Yungay 20cm	0.59 ± 0.12	0.59 ± 0.12	4			
Yungay 33cm					0.52 ± 0.10	n.a.
Yungay 50cm	0.47 ± 0.12	0.43 ± 0.12	4		*0.47*	
Yungay 55cm	0.53 ± 0.12	0.51 ± 0.12	4		0.46 ± 0.10	n.a.
Yungay 75cm	0.56 ± 0.12	0.51 ± 0.12	2		*0.49*	
Yungay 79cm					0.50 ± 0.10	n.a.
Yungay 80cm	0.59 ± 0.12	0.60 ± 0.12	3			
Yungay 94cm					0.66 ± 0.10	n.a.
Yungay 95cm	0.53 ± 0.12	0.52 ± 0.12	4			
Yungay 100cm	0.53 ± 0.12	0.48 ± 0.12	1		*0.62*	
Yungay 112cm					0.53 ± 0.10	n.a.

[a] Cowie and Johnston (2016) recalculated with $\lambda = 0.52$

2.1.4. Conclusions

In this study, we developed an improved neutral pH sample dissolution procedure to convert Na- and Ca-sulfate from soil and geologic samples into pure Ag_2SO_4. For accurate and precise pyrolytic analysis careful attention to detail is required. The described dissolution method was used to quantitatively leach sulfate from natural samples in relatively small amounts of water. This approach avoids acidic sample dissolution, which may lead to analytical artifacts due to oxygen isotope exchange between sulfate and water (Rennie and Turchyn, 2014). To increase the sample throughput, the method from Schauer et al. (2012) was simplified by omitting the ion chromatography and only pay attention to the major contaminants Cl^- and $NO_3{}^-$. During the column chemistry, chloride precipitates on the resin as AgCl and is thus removed from the sample. To take account for contaminations by nitrate, the Ag-sulfate is leached three times with 50 µL water. The accuracy of this approach was verified by analyzing samples from an Atacama Desert soil pit which had previously been analyzed with the fluorination method by Ewing et al. (2008). Although variabilities between the two sample sets were expected due to possible intra-soil heterogeneity in $\Delta^{17}O$ and alteration over time, our pyrolysis results are identical to the previously published fluorination data within analytical uncertainty. However, for sample sets with significant amounts of ions other than Cl^- and $NO_3{}^-$ or organic material, ion chromatography or a pretreatment to remove organic material may be additionally carried out.

We obtain precise $\Delta^{17}O_{VSMOW}(P)$ results using the pyrolysis method with quartz cups by normalizing the data to laboratory in-house standards from Schauer et al. (2012). In comparison to quartz cups, gold capsule measurements show no irregular peak shapes probably because the capsules fully enclose the sample material and the reactor is therefore less prone to etching, and thus high scaling factors. However, quartz cups are less expensive and reusable with no significant decrease in precision compared to gold capsule.

The slope and intercept normalization procedure of scaling and shifting results in excellent reproducibility of standards from different laboratories including those using the fluorination method, which verifies high accuracy overall. Hence, raw data from gold capsules pyrolysis analyses are suitable for normalization and the resulting $\Delta^{17}O_{VSMOW}(P)$ scale is identical to the $\Delta^{17}O_{VSMOW}(F)$ scale within error. The sample peak shape and the normalizing parameters

have to be monitored to assure high data quality of each individual analysis and analytical session. We recommend normalizing the data from each analytical session to standards with known $\Delta^{17}O_{VSMOW}(P)$ or $\Delta^{17}O_{VSMOW}(F)$ values using Equation 2.5.

The obtained external reproducibility of 0.12‰ using quartz sample containers and a sample size of about 30 µmol Ag_2SO_4 can be further improved by minimizing sample size variability or by decreasing the threshold criteria for rejection. The scaling factor may be further suppressed by using gold capsules – although this was not thoroughly tested in this study – or more frequent exchange of the reactor tube. In addition, erratic errors caused by the autosampler used in this study might be remedied by using a different autosampler design. These respective improvements will probably suppress external reproducibility to the 0.0x‰ range.

2.2. Additional Isotope Measurements

Sulfur and Oxygen

For $\delta^{34}S_{SO_4}$ and $\delta^{18}O_{SO_4}$ measurements, the sample sulfate was dissolved as Na_2SO_4 as described in section 2.1.2 (p. 25). Subsequently, the sulfate was precipitated as barite ($BaSO_4$) by adding 2 mL 0.5 M $BaCl_2$ solution to the Na_2SO_4 sample solution. In order to remove any nitrate impurities that can induce artifacts on $\delta^{18}O_{SO_4}$ results due to its large $\delta^{18}O$ (up to 61‰; Reich and Bao, 2018), the dried $BaSO_4$ samples were redissolved in a DTPA-KOH solution and reprecipitated by adding HCl (Bao, 2006; Putnis et al., 2008). The pure and dried $BaSO_4$ samples were analyzed for $\delta^{18}O_{SO_4}$ and $\delta^{34}S_{SO_4}$ at IOW (Leibniz Institute for Baltic Sea Research, Warnemünde, Germany). For the calibration of $\delta^{18}O_{SO_4}$ the international standard material IAEA-SO-5, IAEA-SO-6, and NBS127 were used. Sulfur isotope data were calibrated against the international standard material IAEA-S-2, IAEA-S-3, and NBS127 after Mann et al. (2009). The average 1σ external reproducibility of $\delta^{18}O_{SO_4}$ and $\delta^{34}S_{SO_4}$ is 0.23‰ and 0.1‰, respectively.

Strontium

For Sr isotope measurements, about 50 mg of sample were digested using the protocol of Obert et al. (2022). First, gypsum was dissolved using 7 N HNO_3 on a hotplate at 120 °C. Then, the supernatant was separated from the silicate residue, dried and further digested on a hotplate at 120 °C in a 10:1 mixture of 7 N HNO_3 and 10 N HCl. To destroy organic compounds, 300 mL of H_2O_2 were added. After drying, the samples were dissolved in 1.5 mL 2.5 N HCl for standard ion exchange chromatography using AG 50W X8 resin. Strontium isotope ratios were measured using the Neptune MC-ICPMS at Cologne. For these analyses, measured $^{87}Sr/^{86}Sr$ ratios were normalized to an $^{86}Sr/^{88}Sr$ ratio of 0.1194 using the exponential law. Multiple measurements of the NBS 987 standard yielded a value of 0.710143 with a 2σ error of ±25 ppm. All $^{87}Sr/^{86}Sr$ data are given relative to a value of 0.710240 for the NBS 987 standard. The typical external reproducibility for samples is ±100 ppm. The procedural blank was 800 pg and is negligible, given the amount of Sr in the samples.

2.3. Marine Sulfate Contribution

The relative proportion of marine sulfate on the total sulfate of a sample was determined indirectly using a simple two source mixing model and the distinct $\delta^{34}S$ value of marine sulfate ($\delta^{34}S_m = 21.15 \pm 0.15‰$) and the an estimated $\delta^{34}S_{nm}$ value of $2.85 \pm 0.07‰$ for the non-marine sulfur source (volcanic or anthropogenic) following Rech et al. (2003):

$$\delta^{34}\text{S derived marine sulfate contribution } = \frac{\delta^{34}S_{meas} - \delta^{34}S_{nm}}{\delta^{34}S_m - \delta^{34}S_{nms}}, \tag{2.8}$$

where $\delta^{34}S_{meas}$ is the measured $\delta^{34}S_{SO_4}$ of the sample. For samples with $\delta^{34}S_{meas} < 2.85‰$, $\delta^{34}S$ derived marine sulfate contribution is defined as 0.0. Rech et al. (2003) combined results from steam, lake, and salar salts giving an average $\delta^{34}S_{nm}$ value of $5.4 \pm 2‰$. Sulfate cycling in those water bodies may lead to sulfur fractionation affecting the $\delta^{34}S_{nm}$ value. In the present study, the average of the lowest $\delta^{34}S$ value measured by (Rech et al., 2003) (2.8‰; Salar de Atacama) and the lowest $\delta^{34}S_{SO_4}$ value observed in soil samples of the present study (2.9‰) is used as non-marine sulfur isotope endmember ($\delta^{34}S_{nm} = 2.85 \pm 0.07‰$).

To test the reliability of this approach, the strontium isotope ratio ($^{87}Sr/^{86}Sr$) was used accordingly (Rech et al., 2003). The strontium isotope ratio in the modern ocean is $^{87}Sr/^{86}Sr_m = 0.7091$ (Burke et al., 1982). For the non-marine strontium isotope endmember the average of the lowest $^{87}Sr/^{86}Sr$ ratio measured by (Rech et al., 2003) (0.706682; unnamed salar in Llano de la Paciencia) and the lowest $^{87}Sr/^{86}Sr$ ratio observed in the present study (0.706122) is used. The result ($^{87}Sr/^{86}Sr_{nm} = 0.7064 \pm 0.0004$) is well within the expected range for mantle or juvenile igneous rocks with $^{87}Sr/^{86}Sr = 0.7050$ to 0.7075 (Rech et al., 2003). The Sr derived marine sulfate contribution was determined following:

$$\text{Sr derived marine sulfate contribution } = \frac{^{87}Sr/^{86}Sr_{meas} - {}^{87}Sr/^{86}Sr_{nm}}{^{87}Sr/^{86}Sr_m - {}^{87}Sr/^{86}Sr_{nm}}. \tag{2.9}$$

For samples with $^{87}Sr/^{86}Sr_{nm} < 0.7064$, the Sr marine sulfate contribution is defined as 0.0. This is just a simple approach to test for consistency between $\delta^{34}S$ values and $^{87}Sr/^{86}Sr$ ratios. However, the isotopic composition of the non-marine isotope endmember is more variable than presumed for Equation 2.9 (Gamboa et al., 2019; Godfrey et al., 2019).

3.

Application

3.1. Identifying Sulfate Sources and Water Availability in the Atacama Desert using Triple Oxygen and Sulfur Isotopes

3.1.1. Introduction

In the hyperarid Atacama Desert, sulfate is the dominating salt in soil deposits (e.g., Voigt et al., 2020). Sources include sea spray, terrestrial weathering (e.g. redeposition of playa sediments), and secondary atmospheric sulfate (SAS) (Bao et al., 2001a, 2004; Michalski et al., 2004). The contribution of each source to the total soil sulfate depository varies spatially depending on elevation, distance from sources, and local climate conditions like water availability or prevailing wind direction (Rech et al., 2003; Voigt et al., 2020). Because Atacama Desert sediments are dominated by sulfate, the identification and quantification of local sulfate sources is crucial to understand salt deposition in this unique desert environment. The combination of different isotope tools ($\Delta^{17}O_{SO_4}$, $\delta^{18}O_{SO_4}$, $\delta^{34}S_{SO_4}$, and $^{87}Sr/^{86}Sr$) can help to identify and quantify the different source contributions.

The triple oxygen isotope compositions of sulfate ($\delta^{18}O_{SO_4}$ and $\Delta^{17}O_{SO_4}$) are characteristic for each source, but especially useful to identify the atmospheric source contribution (Bao, 2015). The $\Delta^{17}O_{SO_4}$ from sea spray, playa lakes, and terrestrial weathering is at or slightly below zero, mostly reflecting reactions with water or molecular oxygen (Bao et al., 2004). Oxidation of SO_2 in the atmosphere generally results in positive $\Delta^{17}O_{SO_4}$ ultimately inherited from the mass-independent $\Delta^{17}O_{O_3}$ in ozone (Savarino et al., 2000; Bao, 2015). The positive $\Delta^{17}O_{SO_4}$ is unique for atmospheric oxidation and can therefore serve as a tool to quantify the relative contribution of SAS to the desert soil (Bao et al., 2004; Michalski et al., 2004).

After formation, sulfate is inert under abiotic Earth surface conditions (Bao, 2015). It only exchanges oxygen when processed by microbes or plants (Böttcher et al., 2001; Koprivova and

Kopriva, 2016). The sulfuroxy intermediates in the sulfate reduction pathway readily exchange oxygen and thereby overprint the oxygen isotope composition of sulfate by the isotopic signal of ambient water (Betts and Voss, 1970; Bao, 2015).

The sulfur isotope composition of sulfate ($\delta^{34}S_{SO_4}$) serves as a tool to quantify the contribution of marine sulfate to Atacama Desert soils (Rech et al., 2003). Marine sulfate from the modern Pacific Ocean shows a constant $\delta^{34}S$ value of 21.15 ±0.15‰ (Johnston et al., 2014). Rech et al. (2003) evaluated the marine sulfate contribution using this value for marine sulfate and an estimated $\delta^{34}S$ value of 5.4 ± 2‰ for Andean weathering. This value was obtained by combining and averaging results from Atacama stream, lake, and salar salts (Rech et al., 2003). Strontium isotope ratios can additionally serve as a tool to estimate the calcium source of Atacama Desert Ca-sulfates.

In this study, we combine $\Delta^{17}O_{SO_4}$, $\delta^{18}O_{SO_4}$, and $\delta^{34}S_{SO_4}$ analysis of sulfate from Atacama Desert soils sampled along four W-E transects between 19.5°S and 25°S in order to quantify the relative contribution and spatial distribution of different sulfate sources to the desert soil. Subsequently, the potential of $\Delta^{17}O_{SO_4}$ to identify bioactivity and thus water availability is evaluated.

3.1.2. Samples

The long-term hyperaridity of the Atacama Desert has led to a unique soil structure. A simple generalized Atacama Desert soil profile based on studies of nitrate mining regions consists of five different layers (Figure 3.2) (Ericksen, 1981). The upper 10 to 30 cm thick layer is called chuca, which is often covered by a friable gypsiferous crust with maximum thickness of about 0.5 cm. Chuca consists of powdery to poorly cemented gypsum and anhydrite with variable amounts of silt, sand, and gravels. At the base of this layer, an up to a few cm thick white saline horizon with highly soluble sulfate minerals such as thenardite (Na_2SO_4), bloedite ($Na_2Mg[SO_4]_2 \cdot 4\ H_2O$), and humberstonite ($K_3Na_7Mg_2[NO_3|(SO_4)_3]_2 \cdot 6\ H_2O$) occurs in some areas (Ericksen, 1981). Chuca gradually changes downward into costra – a 0.5 m to 2 m thick moderately to firmly cemented gypsum and anhydrite layer – into caliche – an up to 5 m thick layer of firmly cemented halite (NaCl) with up to 0.5 m thick lateral veins of nitratine ($NaNO_3$). Underneath the caliche follows either salt-cemented regolith containing little nitratine, called conjelo, or

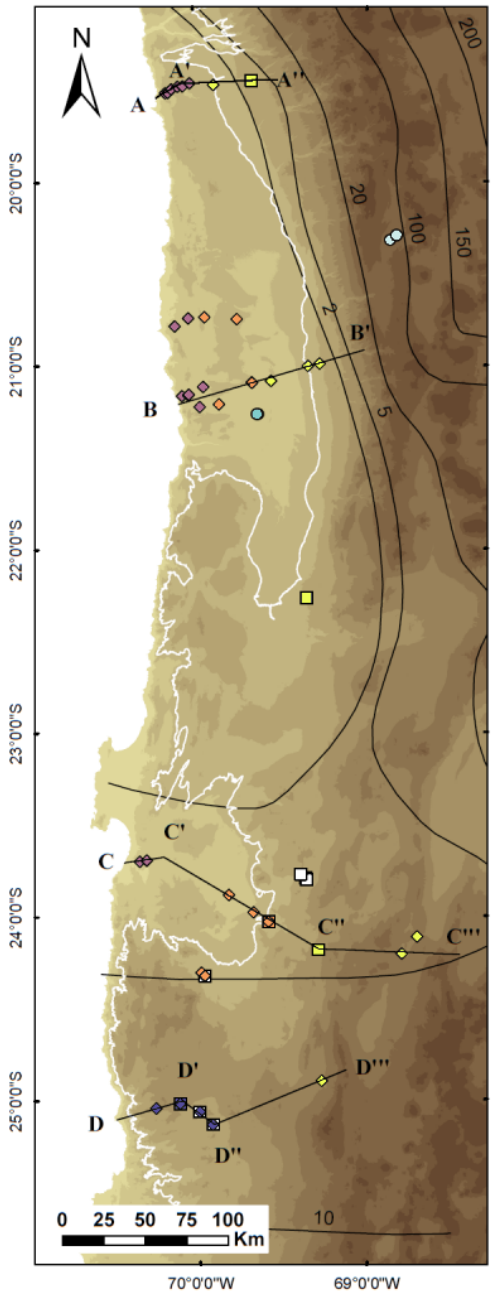

Figure 3.1.: Sample locations of surface samples (diamonds), subsurface samples (squares) and salar samples (circles) from the Western Cordillera, the Precordillera and alluvial fans expanding from there (yellow symbols), the Central Depression (orange symbols), the low Coastal Cordillera (< 1200 m; purple symbols), and from the high Coastal Cordillera (> 1200 m; dark blue symbols). Samples were taken along four W-E transects at Pisagua (19.5°S; A), Salar Grande (21.0°S; B), Antofagasta (24.0°S; C), and Paposo (25.0°S; D). Topographic profiles A-D indicated here are shown in Figure 3.4. The maximum extension of fog (approximately equal to 1200 m) is indicated by the solid white line (Cereceda et al., 2008).

loose unconsolidated regolith, named coba (Ericksen, 1981, 1983). Besides the widespread occurrence of bare soils, playa deposits (salars) with salt-cemented crusts and halite nodules cover large areas especially in the high Andes and the western part of the Central Depression, but also in local basins with past or present groundwater near the surface (Finstad et al., 2016). Active salars grow by evaporation and salt precipitation from capillary rising groundwater, whereby the most soluble salts concentrate at the surface (Finstad et al., 2016). In contrast to salars, the general soil profile from Ericksen shows a top down enrichment of soluble salts. Infiltrating water leaches soluble salts, like thenardite (Na_2SO_4), chloride (e.g., NaCl), and nitratine ($NaNO_3$), from the surface deeper into the soil, where evaporative reprecipitation leads in growth of separated horizons of these soluble salts (Ericksen, 1981, 1983; Chong, 1994; Ewing et al., 2008; Finstad et al., 2014, 2016). The location of each horizon within the soil profile depends on the amount and the solubility of the respective salt and the amount of water. The least soluble salt (here thenardite) forms a horizon closest to the surface, while more soluble salts (here chloride and nitrate) are washed deeper into the soil (Figure 3.2).

Soil samples were taken roughly along four W-E transects beginning at Pisagua (19.5°S), Salar Grande (21.0°S), Antofagasta (24.0°S), and Paposo (25.0°S) (Figure 3.1). The sample set includes 35 samples from the surface crust or chuca (surface samples) and 6 samples from the uppermost costra between 10 and 40 cm soil depth (subsurface samples). These samples have already been characterized for their chemical and mineralogical composition by Voigt et al. (2020). In addition, we determined the isotopic composition of 6 subsurface thenardite (Na_2SO_4) samples (Na_2SO_4 samples), five 'salar samples' including three Na-sulfate samples from the Salar del Huasco and two gypsum ($CaSO_4 \cdot 2\ H_2O$) samples from the Salar de Llamará, and sulfate from groundwater feeding the Salar de Llamará (GW sulfate).

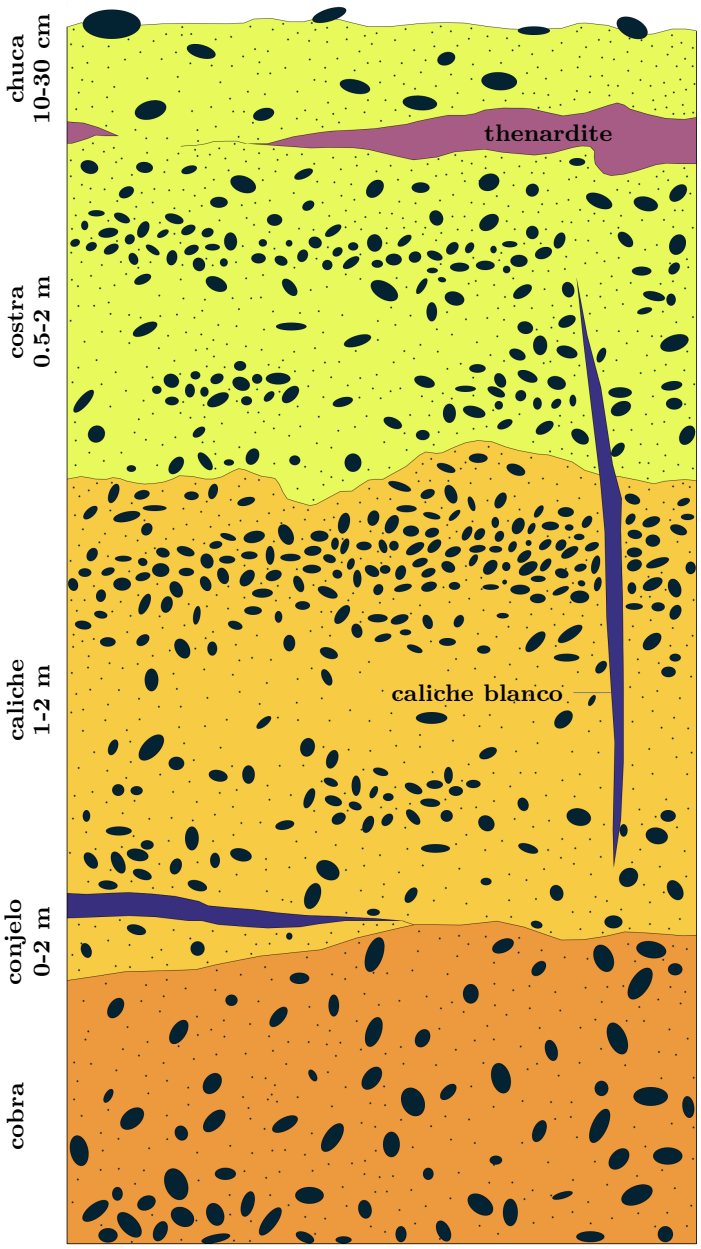

Figure 3.2.: A simple generalized Atacama Desert soil profile based on studies of nitrate mining regions consists of five different layers (see text for details). Figure modified from Ericksen (1983).

3.1.3. Results

All $\Delta^{17}O_{SO_4}$, $\delta^{18}O_{SO_4}$, and $\delta^{34}S_{SO_4}$ results are illustrated in Figure 3.3. The isotopic composition of sulfate varies with distance from the coast and elevation within the four W-E transects (Figure 3.4). Results from surface and subsurface samples taken from the same location are compared in Figure 3.5. Finally, the marine sulfate contribution calculated after Equation 2.8 and results from strontium isotope analysis are illustrated in Figure 3.6 and Figure 3.7. All sample localities, sample classifications, $\Delta^{17}O_{SO_4}$, $\delta^{18}O_{SO_4}$, $\delta^{34}S_{SO_4}$, and $^{87}Sr/^{86}Sr$ values are provided in the appendix (Table A.1).

Triple Oxygen and Sulfur Isotopes

Within all soil samples, $\Delta^{17}O_{SO_4}$ ranges from 0.3‰ to 1.1‰ and generally correlates inversely with $\delta^{18}O_{SO_4}$, which varies between −4‰ and 15‰ (Figure 3.3). Salt samples from Salar de Llamará and Salar del Huasco comprises the lowest $\Delta^{17}O_{SO_4}$ and highest $\delta^{18}O_{SO_4}$ values with 0.15 ± 0.05‰ and 15 ± 3‰, respectively. These samples define the low $\Delta^{17}O_{SO_4}$ endmember of the soil trend. Sulfate extracted from groundwater feeding the Salar de Llamará yields 0.27‰ in $\Delta^{17}O_{SO_4}$ and 10.3‰ in $\delta^{18}O_{SO_4}$. The highest $\Delta^{17}O_{SO_4}$ (>1‰) and lowest $\delta^{18}O_{SO_4}$ values (<1‰) are observed in samples from the highest altitudes in the Coastal Cordillera (high CC) – east of Paposo – well above the coastal fog zone (>1200 m). These surface and subsurface samples define the high $\Delta^{17}O_{SO_4}$ low $\delta^{18}O_{SO_4}$ end of the observed trend. Sediment samples from the lower Coastal Cordillera (low CC), the Central Depression (CD), from Pre-Andean alluvial fans, the Precordillera, and the Western Cordillera (together termed 'PC') plot in between these two endmembers of the trend. Na_2SO_4 samples generally show low $\delta^{18}O_{SO_4}$ values and plot slightly below the observed trend (Figure 3.3).

The $\delta^{34}S_{SO_4}$ values range from −0.9‰ to 19.1‰ and do not correlate with $\Delta^{17}O_{SO_4}$ (Figure 3.3) or $\delta^{18}O_{SO_4}$ (see appendix Figure A.1). Salar samples show $\delta^{34}S_{SO_4}$ values that range between 6.5‰ and 9.3‰. Na_2SO_4 samples generally show low $\delta^{34}S_{SO_4}$ values with ≤ 5.2‰. High $\delta^{34}S_{SO_4}$ values are observed in samples from the low Coastal Cordillera, which generally show $\delta^{34}S_{SO_4}$ values >8.5‰ (Figure 3.3).

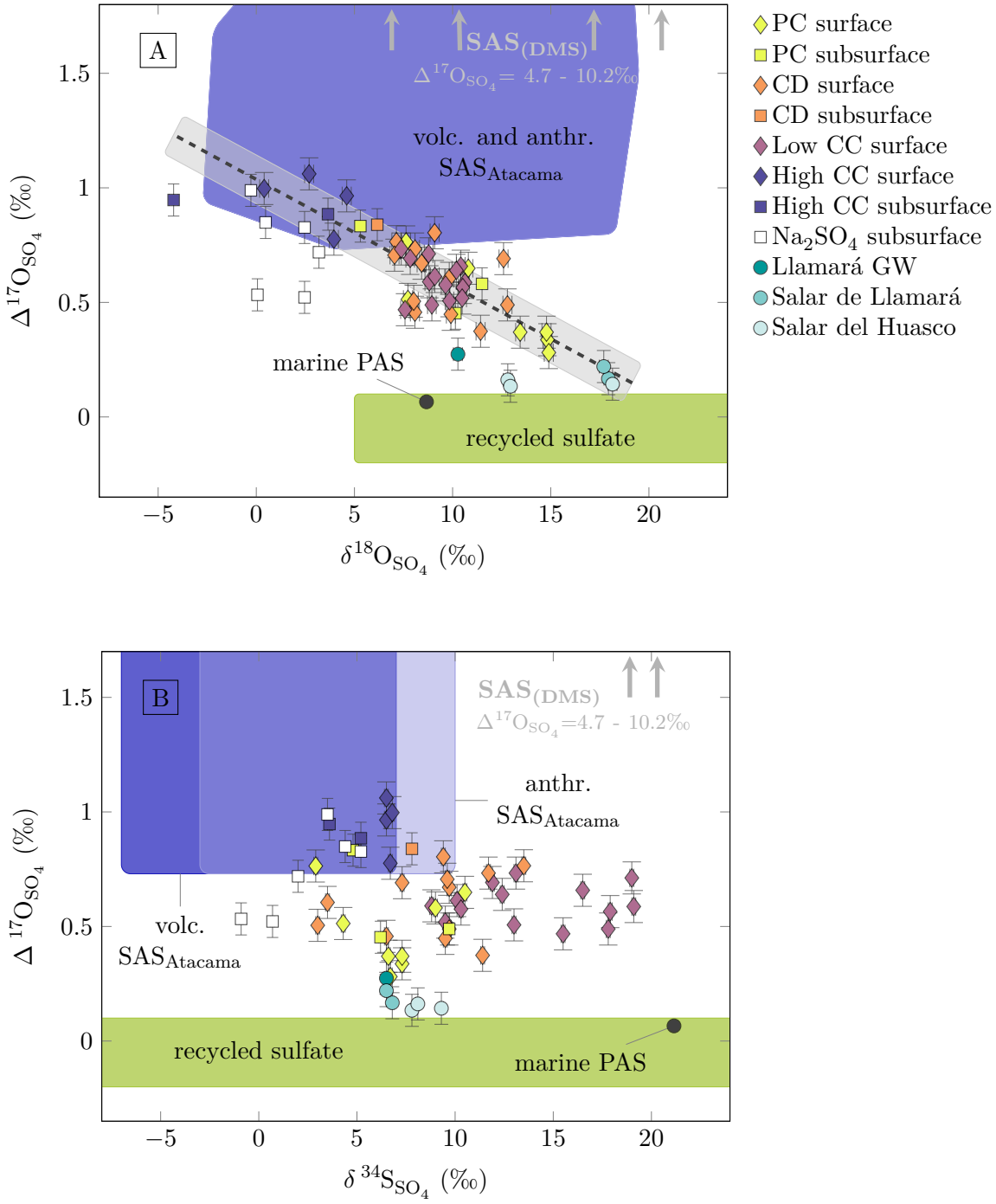

Figure 3.3.: Enlarged section from Figure 1.5 with results of surface (diamonds) and subsurface (squares) samples from the Coastal Cordillera >1200 m (high CC) and <1200 m (low CC), the Central Depression (CD), and the Western Cordillera, Precordillera and its alluvial fans (PC), along with results of Na_2SO_4 subsurface samples, groundwater, and salar samples. A) $\Delta^{17}O_{SO_4}$ values versus $\delta^{18}O_{SO_4}$. Error bars depict the mean 1σ standard deviation which is 0.07‰, 0.23‰, respectively. The dashed line displays a trend between $\Delta^{17}O_{SO_4}$ and $\delta^{18}O_{SO_4}$ of all analyzed surface samples with the mean deviation from this line shown in gray (1σ SD = 0.11). B) $\Delta^{17}O_{SO_4}$ versus $\delta^{34}S_{SO_4}$ values. Error bars depict the mean 1σ standard deviation which is 0.07‰, 0.1‰, respectively.

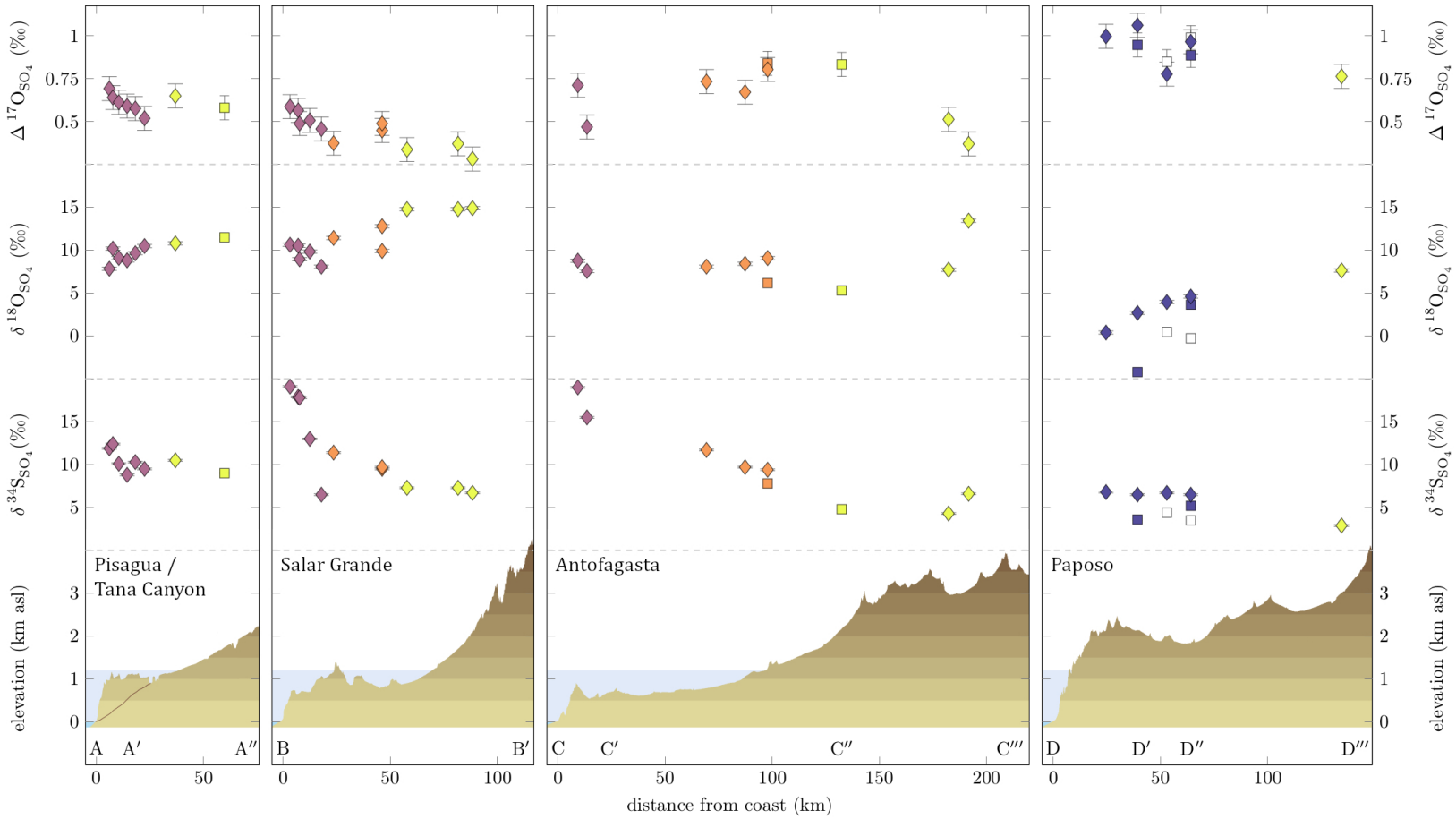

Figure 3.4.: $\Delta^{17}O_{SO_4}$, $\delta^{18}O_{SO_4}$, and $\delta^{34}S_{SO_4}$ results of all surface (diamonds) and subsurface (squares) samples taken along the four W-E transects, which are indicated in Figure 3.1. For further information on the colors of the symbols, the reader is referred to Figure 3.3. Topographic profiles with color shading that changes every 500 m are shown for each of the transects. Altitudes with possible fog advection are indicated as blue area below 1200 m. In transect A, samples were taken at the top of Tana Canyon. The dark line in profile A indicates the base of this canyon. Errors bars show mean 1σ standard deviations, which are 0.07‰, 0.23‰, and 0.1‰ for $\Delta^{17}O_{SO_4}$, $\delta^{18}O_{SO_4}$, and $\delta^{34}S_{SO_4}$, respectively. Samples from locations >15 km away from the respective profile line are not shown.

Transects

$\Delta^{17}O_{SO_4}$ generally decreases with distance from the coast (Figure 3.4). In transect A, B, and D, highest $\Delta^{17}O_{SO_4}$ values are observed within the Coastal Cordillera and absolute $\Delta^{17}O_{SO_4}$ values decrease towards north. Thus, overall highest $\Delta^{17}O_{SO_4}$ (>1‰) are found in samples from transect D within the Coastal Cordillera. In transect A and B, $\Delta^{17}O_{SO_4}$ decreases by about 0.2‰ within the first six samples of the respective transect. In transect A, $\Delta^{17}O_{SO_4}$ values remain constant, while those obtained in samples from transect B and D further decrease with distance from the coast. In transect C, $\Delta^{17}O_{SO_4}$ values are relatively uniform within 150 km distance from the coast with 0.72 ± 0.13‰. Samples from Precordillera and the Western Cordillera generally show low $\Delta^{17}O_{SO_4}$ values.

The $\delta^{18}O_{SO_4}$ values generally increase with distance from the coast (Figure 3.4). The lowest $\delta^{18}O_{SO_4}$ values are observed in transect D within the Coastal Cordillera. Highest $\delta^{18}O_{SO_4}$ are measured in samples from alluvial fans east of the Precordillera (transect A, B, and C).

In contrast to $\delta^{18}O_{SO_4}$, $\delta^{34}S_{SO_4}$ generally decreases with distance from the coast and with increasing elevation. This is especially observed in transect B and C, where $\delta^{34}S_{SO_4}$ values decrease from 19.1‰ to 6.5‰ and from 19.0‰ to 4.3‰, respectively. In transect A and D, $\delta^{34}S_{SO_4}$ is relatively constant with average values of 10.3 ± 1.3‰ and 5.1 ± 1.6‰, respectively.

Subsurface

$\Delta^{17}O_{SO_4}$ values of surface and subsurface samples taken from the same locality are identical within analytical uncertainty with an average deviation of -0.2 ± 0.8‰ (Figure 3.5). However, sediment subsurface samples show lower $\delta^{18}O_{SO_4}$ and $\delta^{34}S_{SO_4}$ values compared to respective surface samples, deviating by -3.6 ± 3.0‰ and -1.9 ± 0.9‰, respectively. Na_2SO_4 subsurface samples show even larger deviations compared to the respective surface sample with -6.0 ± 3.3‰ and -3.2 ± 1.1‰ in $\delta^{18}O_{SO_4}$ and $\delta^{34}S_{SO_4}$, respectively (Figure 3.5). For the interpretation and discussion of these results the reader is referred to section 3.1.4 (p. 67).

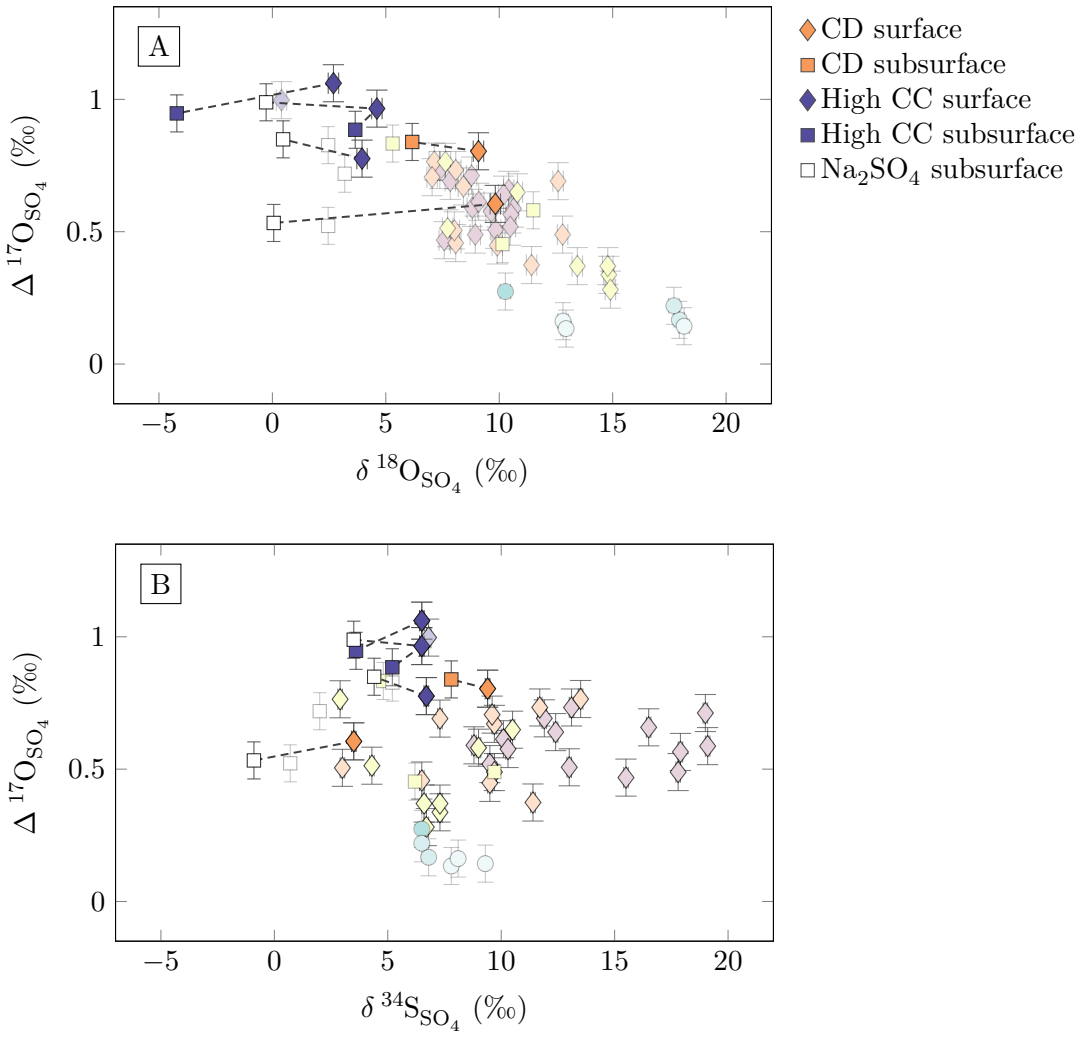

Figure 3.5.: A) $\Delta^{17}O_{SO_4}$ versus $\delta^{18}O_{SO_4}$ values and B) $\Delta^{17}O_{SO_4}$ versus $\delta^{34}S_{SO_4}$ of surface and subsurface samples. Dashed lines connect surface and respective subsurface samples from the same locality. Errors bars show mean 1σ standard deviations, which are 0.07‰, 0.23‰, and 0.1‰ for $\Delta^{17}O_{SO_4}$, $\delta^{18}O_{SO_4}$, and $\delta^{34}S_{SO_4}$, respectively.

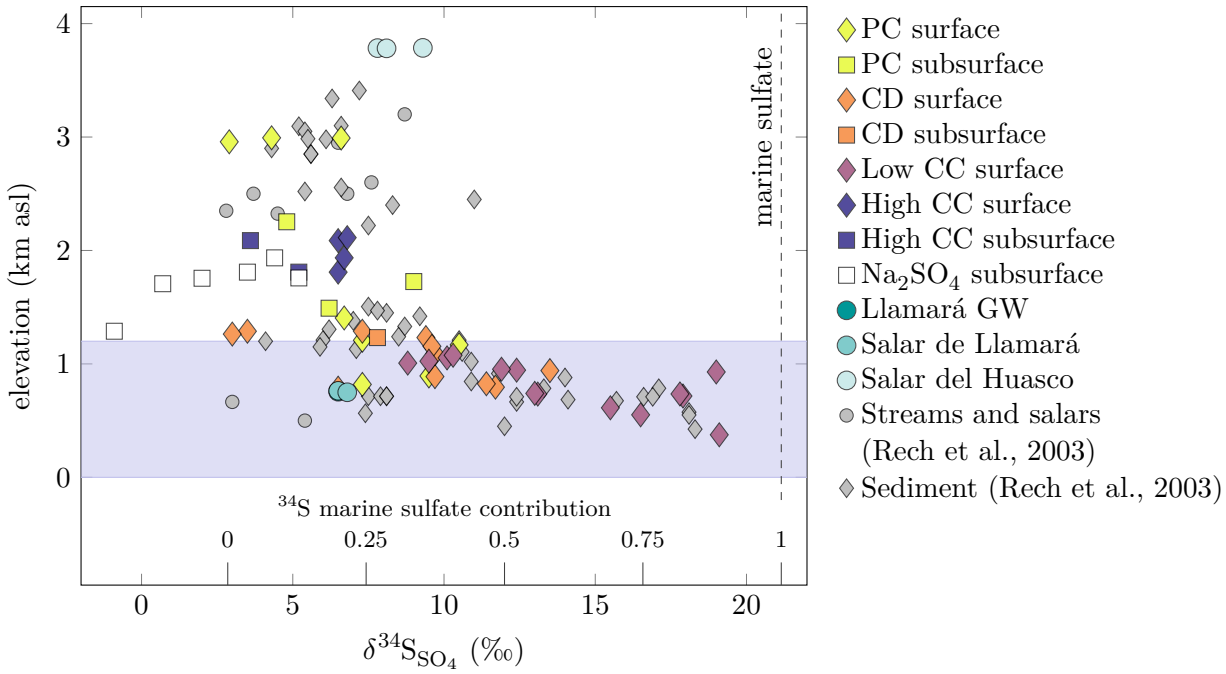

Figure 3.6.: $\delta^{34}S_{SO_4}$ values and the marine sulfate contribution calculated after (2.8) using these values versus elevation of the respective sample locations. Altitudes of fog occurrence are shaded in blue.

Marine Sulfate Contribution

The marine sulfate contribution calculated after Equation 2.8 shows large variations from 0.0 to 0.89 (Figure 3.6). Sediment samples taken below the maximum altitude of fog advection (1200 m) show higher marine sulfate source contributions (0.48 ± 0.21 on average) compared to samples taken above 1200 m (0.16 ± 0.12 on average). Marine sulfate contributions higher than 0.5 are only observed at elevations below 1200 m (Figure 3.6).

The marine sulfate contribution calculated after Equation 2.9 using $^{87}Sr/^{86}Sr$ correlates with the $\delta^{34}S_{SO_4}$ derived marine sulfate contribution for samples taken below 1200 m (Figure 3.7). Samples taken above this altitude show $\delta^{34}S_{SO_4}$ marine sulfate contribution < 0.5, while marine sulfate contributions derived from Sr cover the whole range from 0 to 1 (Figure 3.7).

The estimated marine sulfate contributions derived from $\delta^{34}S$ and Sr are discussed in section 3.1.4 (p. 58).

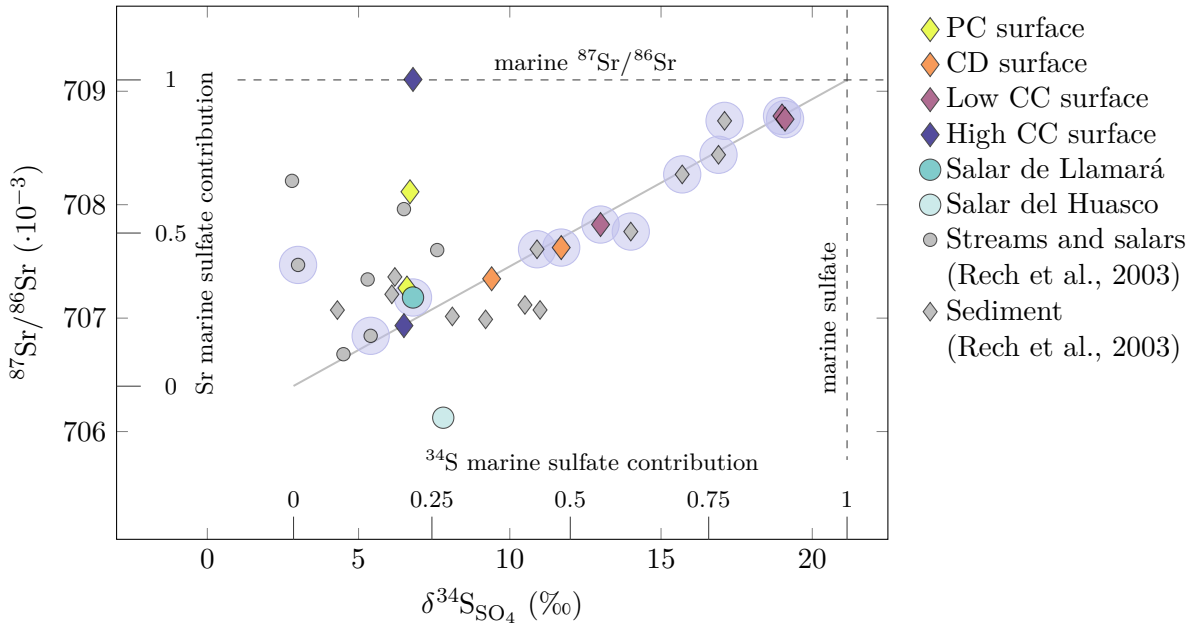

Figure 3.7.: $\delta^{34}S_{SO_4}$ and $^{87}Sr/^{86}Sr$ values of surface and salar samples compared to previously published data (gray symbols). Blue shaded data indicate samples that were taken below an altitude of 1200 m. The dashed lines indicate the $\delta^{34}S_{SO_4}$ of marine sulfate and the marine $^{87}Sr/^{86}Sr$ value. The gray line shows a 1:1 relationship of the marine sulfate contributions calculated using Equations (2.8) and (2.9).

3.1.4. Discussion

Atmospheric Sulfate

Throughout positive $\Delta^{17}O_{SO_4}$ values of sulfate samples (from 0.1‰ to 1.1‰) indicate that SAS contributes significantly to the sulfate budget of Atacama Desert soils (Figure 3.3). Previous studies already observed positive $\Delta^{17}O_{SO_4}$ in sediments from the Atacama Desert (Bao et al., 2004; Michalski et al., 2004; Ewing et al., 2008; Sun et al., 2018). First studies observed significantly higher values of up to 4.66‰ (Bao et al., 2004; Michalski et al., 2004). However, these high values were later found to be a result of contamination with nitrate (Bao, 2006). For $\Delta^{17}O_{SO_4}$ analysis by laser fluorination, $BaSO_4$ is precipitated from a sample solution. When this solution shows a high ${NO_3}^-/{SO_4}^{2-}$ ratio, nitrate is occluded in the $BaSO_4$ crystals. Nitrates from the Atacama Desert comprise $\Delta^{17}O_{NO_3}$ values up to 30‰ (Michalski et al., 2004), wherefore nitrate impurities significantly influence the $\Delta^{17}O_{SO_4}$ results. Samples that showed highest $\Delta^{17}O_{SO_4}$ values (4.62 ± 0.08‰ and 4.66 ± 0.08‰) were reanalyzed with an adjusted $BaSO_4$ sample preparation resulting in significantly lower $\Delta^{17}O_{SO_4}$ values (0.31 ± 0.08‰ and 0.36 ± 0.08‰, respectively) (Bao, 2006). The reanalyzed $\Delta^{17}O_{SO_4}$ values fall well within the $\Delta^{17}O_{SO_4}$ range observed in the present study. Ewing et al. (2008) analyzed samples from a 2 m soil pit (Yungay, 24°6.8′ S, 70°0.4′ W) receiving $\Delta^{17}O_{SO_4}$ values between 0.46 ± 0.1‰ and 0.66 ± 0.1‰. This soil pit was reanalyzed in the present study and results are identical to the published data within analytical uncertainty (see section 2.1.3; p. 38).Sun et al. (2018) analyzed samples from a 100 m deep exploration drill core (Spence, 22°47.3′ S, 69°15.3′ W). Within this profile $\Delta^{17}O_{SO_4}$ values decrease downwards from 0.29‰ to −0.20‰ (Sun et al., 2018). These low $\Delta^{17}O_{SO_4}$ values are interpreted to reflect wetter climate conditions in the past (Sun et al., 2018) and are therefore lower than results from surface and subsurface samples analyzed in the presented study. All in all, the $\Delta^{17}O_{SO_4}$ range observed in the presented studies is in well agreement with results obtained in previous studies (Bao et al., 2004; Michalski et al., 2004; Ewing et al., 2008; Sun et al., 2018).

In section 1.3.3 (p. 13) various global circulation models were used to estimate a range in $\Delta^{17}O_{SO_4}$ for SAS resulting in values between 0.7‰ and 2.4‰ (Figure 1.4B). The triple oxygen isotope data obtained from some natural samples analyzed in the presented study and

published data fall well within this modeled range. The isotopic composition of samples from the high Coastal Cordillera is interpreted to mainly reflect the isotopic composition of SAS (see discussion below; p. 67). Hence, the $\Delta^{17}O_{SO_4}$ endmember of pure SAS in the Atacama Desert is assumed to be about 1.1‰. Similar maximum values were obtained in previous studies. Dry and wet deposited atmospheric sulfate sampled in Baton Rouge (LA, USA) during a 600-day period yielded $\Delta^{17}O_{SO_4}$ values between 0.25‰ and 1.43‰ with a long-term average of 0.62 ± 0.32‰ (Jenkins and Bao, 2006). Atmospheric sulfates extracted from rain water from La Jolla (CA, USA) show a similar range in $\Delta^{17}O_{SO_4}$ from 0.2‰ to 1.4‰ (Lee and Thiemens, 2001). Sulfate aerosols analyzed in the same study have $\Delta^{17}O_{SO_4}$ values between 1‰ and 1.6‰ (Lee and Thiemens, 2001). Hence, the modeled oxygen isotopic composition for SAS with $\Delta^{17}O_{SO_4}$ from 0.7‰ to 2.4‰ seems to be reasonable for volcanic and anthropogenic SAS deposited to Atacama Desert sediments.

Marine Sulfate

Marine sulfate is transported to the Atacama Desert dissolved in fog water, sea spray or as dry marine aerosol. The upwelling water masses at the west coast of Chile transports nutrient-rich water to the ocean's surface, where solutes are incorporated into coastal fog by sea spray (O'Dowd and De Leeuw, 2007). While moving inland, the fog evaporates and the solutes are deposited to Atacama Desert soils by dry or wet deposition. Due to the subsidence inversion layer, aerosol transport from the Pacific into the Atacama Desert is restricted to altitudes < 1200 m.

The marine sulfate contribution was calculated first using $\delta^{34}S_{SO_4}$ after Equation 2.8 and second using $^{87}Sr/^{86}Sr$ after Equation 2.9 following Rech et al. (2003). Samples taken below 1200 m generally show higher $\delta^{34}S$ derived marine sulfate contributions compared to samples taken above this altitude (0.48 ± 0.21 and 0.16 ± 0.12, respectively). This is consistent with results from Rech et al. (2003), who observed that most soils within 90 km of the coast and below 1200 m in elevation, are influenced by marine aerosols (Figure 3.6). The $\delta^{34}S$ derived marine sulfate contribution in samples taken below 1200 m correlates with the marine sulfate contribution derived from Sr – especially for sediment samples (Figure 3.7). The observed

consistency in samples taken below 1200 m between both approaches indicates that they reflect the true marine sulfate source contribution.

For samples taken above 1200 m, the $\delta^{34}S$ derived marine sulfate contributions is generally low (0.16 ± 0.12) and does not correlate with the Sr derived marine sulfate contribution (Figure 3.7). In those samples, $\delta^{34}S$ derived marine sulfate contributions of up to 0.45 are observed, while the marine sulfate contributions derived from Sr cover the whole range from 0 to 1 (Figure 3.7). For both calculations (2.8) and (2.9) a simple mixing of two sulfate sources (marine and non-marine) with distinct isotope values was presumed. While the isotope values for the marine source are well defined with $\delta^{34}S_m = 21.15 \pm 0.15‰$ and $^{87}Sr/^{86}Sr_m = 0.7091$ (Burke et al., 1982; Johnston et al., 2014), a range in $\delta^{34}S_{nm}$ from $-7‰$ to $10‰$ (Figure 1.5) and in $^{87}Sr/^{86}Sr_{nm}$ from 0.705 to 0.715 for the non-marine source better reflects reality (Bao et al., 2003; Gislason and Torssander, 2006; Bindeman et al., 2007; Gamboa et al., 2019; Godfrey et al., 2019). Some of the observed scatter might be explained by the simplification that a distinct isotopic composition for the non-marine source was presumed.

In addition, $\delta^{34}S_{SO_4}$ values and $^{87}Sr/^{86}Sr$ ratios reflect the source of different parts of the sulfate mineral. $\delta^{34}S_{SO_4}$ reflects the sulfur source while $^{87}Sr/^{86}Sr$ represents the Ca source of Ca-sulfates. During dissolution and reprecipitation of sulfate, its $\delta^{34}S_{SO_4}$ value remains unchanged. However, the $^{87}Sr/^{86}Sr$ ratio may be overprinted by the strontium ratio of ambient water which is dependent on the underlying lithology. In the Atacama Desert, basement rocks are quite diverse and include Jurassic marine sediments, continental sediments from the Cretaceous to recent, and volcanic intrusive rocks and sediments from the Paleozoic to the Upper Tertiary (Tapia et al., 2018). This diversity results in highly variable observed $^{87}Sr/^{86}Sr$ ratios in Atacama Desert waters (between 0.705 and 0.715; Gamboa et al., 2019; Godfrey et al., 2019). Hence, (partial) dissolution and reprecipitation of sulfate affect the $^{87}Sr/^{86}Sr$ ratios and result in different marine sulfate contributions derived from $\delta^{34}S$ and Sr, respectively. Dissolution and reprecipitation of sulfate might also result in the marine $^{87}Sr/^{86}Sr$ ratio and a rather Andean $\delta^{34}S$ value observed in one sample from the high Coastal Cordillera (Figure 3.7). The observed range in $\delta^{34}S_{SO_4}$ in samples taken above 1200 m probably reflects a global mixture of volcanic and anthropogenic emissions, marine sulfate and SAS derived from

natural or anthropogenic sources. Whereas the range in the marine sulfate contribution derived from Sr rather results from the highly variable bedrock $^{87}Sr/^{86}Sr$ ratio.

Voigt et al. (2020) used Cl concentrations in bulk sediment samples as indicator for marine salt contributions. High Cl concentrations are only observed within the area of frequent fog occurrence supporting that 1200 m is generally the maximum level of marine aerosol transport. Because air masses from the Pacific Ocean do not exceed the subsidence inversion layer, marine sulfate transport from the Pacific Ocean above 1200 m is small. Hence, while samples taken below an altitude of 1200 m may be dominated by local marine sulfate input, the Cl concentration of samples taken above this altitude rather reflects the global sea spray signal.

Furthermore, biogenic sulfur gases that are emitted from the ocean, like DMS, comprise a marine sulfur isotopic composition with $\delta^{34}S$ values from 18.9‰ to 20.3‰ (Figure 1.5). The two source mixing model used for the estimation of the marine sulfate contribution does not take secondary atmospheric sulfate into account. Hence, contributions from $SAS_{(DMS)}$ lead to an overestimation of the marine sulfate source. Such contributions are identified in some samples taken close to the coast (Ata17-047a, Ata17-048a, and Ata17-008a). These samples comprise relatively high $\Delta^{17}O_{SO_4}$ and $\delta^{34}S_{SO_4}$ values (from 0.49‰ to 0.71‰ and from 16.5‰ to 19.1‰, respectively; Figure 3.4) which can not be explained by simple mixing of marine sulfate with volcanic or anthropogenic SAS. Adding $\Delta^{17}O_{SO_4}$ to the mixing model allows to distinguish between three sulfate sources – marine sulfate, SAS, and $SAS_{(DMS)}$. The relative contribution of $SAS_{(DMS)}$ is estimated using the distinct isotopic compositions of marine sulfate ($\Delta^{17}O_{SO_4} = 0.07 \pm 0.2$‰ and $\delta^{34}S_{SO_4} = 21.15 \pm 0.15$‰), SAS ($\Delta^{17}O_{SO_4} = 0.94 \pm 0.1$‰ and $\delta^{34}S_{SO_4} = 5.88 \pm 1.3$‰), and $SAS_{(DMS)}$ ($\Delta^{17}O_{SO_4} = 4.7$‰ to 10.2‰ and $\delta^{34}S_{SO_4} = 18.9$‰ to 20.3‰). Because samples from the high Coastal Cordillera best reflect the isotopic composition of SAS deposited in the Atacama Desert (see discussion below; p. 67), the mean $\Delta^{17}O_{SO_4}$ and $\delta^{34}S_{SO_4}$ value of these samples is used for the estimation of contributions from $SAS_{(DMS)}$. Such a three source mixing model based on $\Delta^{17}O_{SO_4}$ and $\delta^{34}S_{SO_4}$ results in contributions from $SAS_{(DMS)}$ of 3.2% to 11.6% in the named samples (Ata17-047a, Ata17-048a, and Ata17-008a). The obtained range is mainly due to the range in $\Delta^{17}O_{SO_4}$ of $SAS_{(DMS)}$. However, within this estimation possible sulfate cycling due to water availability is not considered. Biological sulfate cycling lowers the $\Delta^{17}O_{SO_4}$ values of a sample resulting in lower estimated $SAS_{(DMS)}$

contributions. All in all, the estimation of marine sulfate source contributions is more complex than predicted by the used two source mixing model following Rech et al. (2003). Considering $\Delta^{17}O_{SO_4}$ in addition to $\delta^{34}S$ allows to distinguish between contributions from marine sulfate and from $SAS_{(DMS)}$.

Cycled Sulfate

The triple oxygen isotope data ($\Delta^{17}O_{SO_4}$ and $\delta^{18}O_{SO_4}$) show a trend from the isotopic signal of SAS towards the isotopic composition of cycled sulfate (Figure 3.3). This trend seems to be isotopically independent from the influence of marine sulfate, even though, high $\delta^{34}S_{SO_4}$ values suggest a significant contribution from marine sulfate (up to 89%) especially for samples taken below 1200 m. This might be explained by contributions from $SAS_{(DMS)}$ which lead to higher $\delta^{34}S_{SO_4}$ values and therefore, to an overestimation of the marine sulfate source (Wang et al., 2014). In addition, biological sulfate cycling results in a shift in the oxygen isotopic composition due to oxygen isotope exchange with ambient water. This generally leads to $\Delta^{17}O_{SO_4}$ values that converge towards 0‰ and increasing $\delta^{18}O_{SO_4}$ values depending on the $\delta^{18}O$ of the respective water. $\delta^{34}S_{SO_4}$ is expected to remain unchanged during biological sulfate cycling, if no sulfur is introduced to or removed from the system (e.g., transport of dissolved sulfur species or precipitation or oxidation of sulfides). However, because biological sulfate cycling affects $\Delta^{17}O_{SO_4}$ and $\delta^{18}O_{SO_4}$ it is clearly identifiable by the observed inverse correlation. The low $\Delta^{17}O_{SO_4}$ high $\delta^{18}O_{SO_4}$ endmember of the trend is defined by salar samples which isotopically reflect cycled sulfate. Because all samples fall on a trend towards this isotopic endmember, the observed inverse correlation is interpreted to be a result of various relative amounts of cycled sulfate within the sample. The cycled sulfate contribution either originates from (1) redistribution of cycled sulfate, e.g., from salar surfaces (source dominated) and/or (2) in-situ biological sulfate cycling (process dominated).

Redistribution of cycled sulfate occurs on a rather local scale. Desert pavements and gypsum crusts – both commonly observed in the Atacama Desert – generally protects the underlying soil from wind erosion (Jianjun et al., 2001; Wang et al., 2014). In addition, entrainment of surface material results in large aerosols, which are usually deposited near the source because of rapid gravitational settlement (Wang et al., 2014). This is supported by geochemical, isotopic,

and mineralogical investigations of atmospherically deposited materials (Wang et al., 2014). Furthermore, salar surfaces mainly consists of halite (NaCl) (Finstad et al., 2016). Thus, if redistribution of cycled sulfate from salar surfaces is the dominant process to form the observed inverse correlation, samples with low $\Delta^{17}O_{SO_4}$ and high $\delta^{18}O_{SO_4}$ values should show a high NaCl concentration. Additionally, the Na/Cl ratio in these samples should show a molar Na/Cl ratio of 1. These samples however generally show lower NaCl concentrations and a Na/Cl ratio $\neq 1$ (Voigt et al., 2020). The average Na/Cl ratio of sediment samples with a high Cl concentration (=0.83) rather reflects the sea water ratio (=0.86) than the Na/Cl ratio of halite (=1) (Voigt et al., 2020). Redistribution of material from salar surfaces to the Atacama Desert soils hence only plays a minor role or is restricted to a very local scale (Wang et al., 2014; Voigt et al., 2020). The cycled sulfate contribution in Atacama sediments probably rather derives from in-situ biological sulfate cycling. Biological activity is limited by water and thus the observed trend between $\Delta^{17}O_{SO_4}$ and $\delta^{18}O_{SO_4}$ might be interpreted as a gradient for water availability. This is supported by Sun et al. (2018), who also observed an inverse correlation between $\Delta^{17}O_{SO_4}$ and $\delta^{18}O_{SO_4}$ in the lower part of the 100 m drill core from Spence. This trend is interpreted to reflect a change from wetter climate conditions (low $\Delta^{17}O_{SO_4}$, high $\delta^{18}O_{SO_4}$) (semiarid) to the hyperarid conditions (high $\Delta^{17}O_{SO_4}$, low $\delta^{18}O_{SO_4}$) prevailing today in the Atacama Desert (Sun et al., 2018).

Water Availability

The low water availability in the hyperarid Atacama Desert limits post-depositional biological alteration processes. Hence, the preservation of the positive $\Delta^{17}O_{SO_4}$ values from SAS is a distinct feature of arid desert environments (Wang et al., 2016). Biological sulfate cycling generally changes the oxygen isotope composition of deposited sulfate towards zero in $\Delta^{17}O_{SO_4}$ and towards higher $\delta^{18}O_{SO_4}$ values. The intensity of this isotopic shift depends on the degree of sulfate cycling and therewith indirectly on water availability. Possible water sources for Atacama Desert soils are groundwater, local precipitation, run-off from distal precipitation, and fog.

A shallow groundwater table, particularly present in parts of the Central Depression and the Western Cordillera, leads to the formation of salars (Finstad et al., 2016). Because in salars

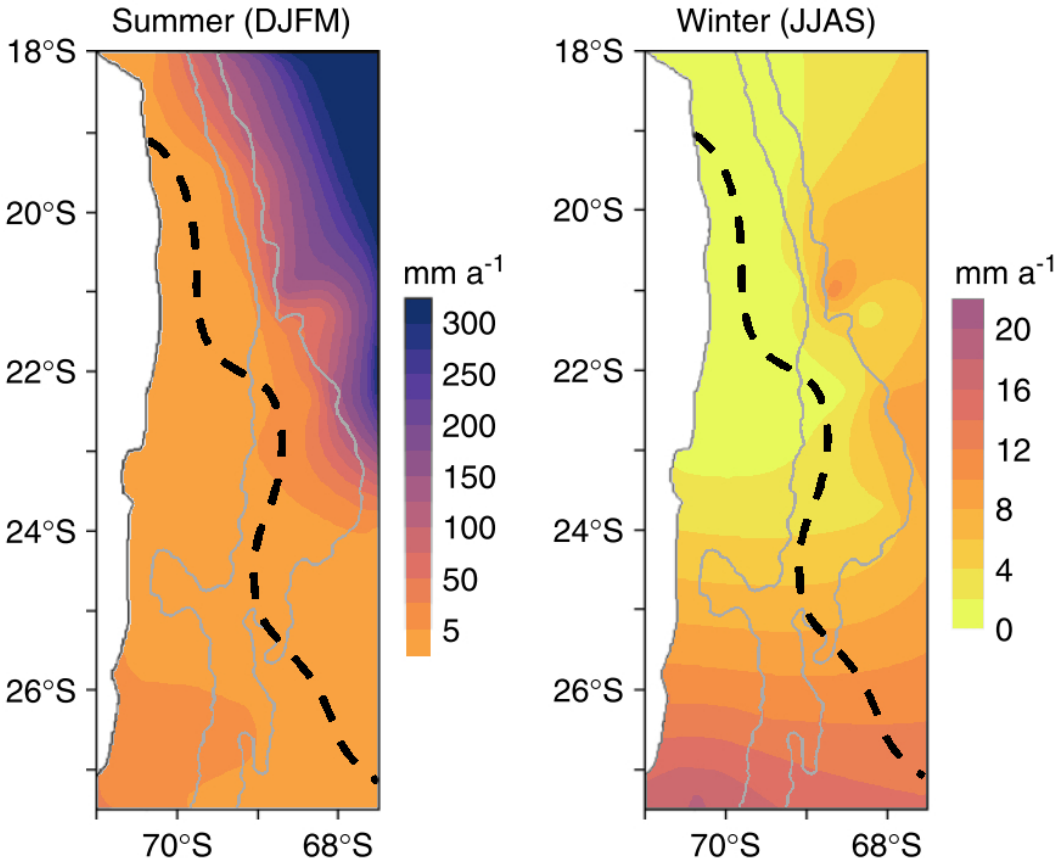

Figure 3.8.: Mean annual rainfall for the period 1977–2000 summer and winter months in the central Atacama Desert. Note the difference in scales for summer and winter. The dashed black line marks the border between areas dominated by summer and winter rainfall. The gray lines define the 2000 m and 4000 m elevation lines. Figure modified from Houston (2006).

water is constantly available, salar sulfates are expected to be almost completely biologically cycled. This is supported by low $\Delta^{17}O_{SO_4}$ and high $\delta^{18}O_{SO_4}$ values of salar sulfate samples (Figure 3.3). The variable range in $\delta^{18}O_{SO_4}$ observed in these salar sulfate samples might reflect different degrees of evaporation of the respective salar water (Surma et al., 2015, 2018; Voigt et al., 2021).

The Western Cordillera, the Precordillera and alluvial fans expanding along the slope of the Precordillera receive water from local and distal precipitation. In the northern part of the studied area (<22° S), rain events occur occasionally on the Altiplano and the western slope of the Andes especially during summer (Figure 3.8; Houston, 2006). These precipitation events result in flash-floods which frequently reach the alluvial fans (Scheihing et al., 2018; Viguier

et al., 2020), leading to higher water availability and consequently to effective sulfate cycling. In the southern part of the studied area, rain events predominantly occur during winter and generally show less precipitation (Figure 3.8; Houston, 2006). Thus, samples from the Western Cordillera and Precordillera of transect C and D generally receive less precipitation compared with respective samples of transect A and B. The relatively high water availability due to run-off from distal rain events is especially observable in transect B (Figure 3.4), where the lowest $\Delta^{17}O_{SO_4}$ and highest $\delta^{18}O_{SO_4}$ values in sediment samples are found. In transect A, the easternmost sample (Ata19-044c) originates from a topographic high between two canyons which are 150 m and 250 m deeper than the sample location (see appendix Figure A.2 and Figure A.3). Therefore, water availability at this particular location is lower compared to the alluvial fans in general leading to a low degree of biological cycled sulfate. The lower amount of annual precipitation in the southern part of the studied area and related therewith less biological sulfate cycling leads to a better preservation of the positive $\Delta^{17}O_{SO_4}$ values from SAS in this area. In the southern part of the studied area, the terrain is relatively rough, wherefore the topography of the sample location is important when interpreting the isotopic composition of a sample. For example in transect C, the easternmost two samples (Ata17-018a, Ata17-020a) originate from a local basin, where water from rare precipitation events is gathered. These samples have $\Delta^{17}O_{SO_4}$ values of 0.51 ± 0.07‰ and 0.37 ± 0.07‰ and $\delta^{18}O_{SO_4}$ values of 7.73 ± 0.23‰ and 13.44 ± 0.23‰. In contrast, the easternmost sample in transect D (Ata18-004a) originates from a topographic high close to the watershed and comprises $\Delta^{17}O_{SO_4} = 0.76 \pm 0.07$‰ and $\delta^{18}O_{SO_4} = 7.63 \pm 0.23$‰ supporting a relatively low degree of sulfate recycling. Hence, the respective location of this sample leads to relatively lower water availability and thus, less effective biological sulfate cycling compared to topographic lows.

In the Central Depression, local precipitation is generally lower than 5 mm yr^{-1} (Figure 3.1, Figure 3.8; Houston, 2006). Locally, higher water availability may be related to run-off water from distal precipitation, leading to the formation of small ephemeral ponds in local basins. In addition, elevations <1200 m are frequently affected by fog (Cereceda et al., 2008). Because fog penetrates inland expanding from the Pacific Ocean, the frequency of fog occurrence is highest close to the coast and decrease towards the east. This decreasing frequency of fog occurrence is generally reflected in the $\Delta^{17}O_{SO_4}$ values of samples from the Central Depression.

Samples taken <25 km from the coast and below 1200 m asl (Ata17-055b and Ata18-043a) show relatively low $\Delta^{17}O_{SO_4}$ values (0.37 ± 0.07‰ and 0.46 ± 0.07‰, respectively) reflecting a relative effective sulfate cycling due to moisture supply from fog. Moreover, samples taken >90 km from the coast (Ata17-014a and Ata17-014b) show relatively high $\Delta^{17}O_{SO_4}$ values (0.80 ± 0.07‰ and 0.84 ± 0.07‰, respectively) which indicate low biological sulfate cycling due to low water availability. In addition to in-situ sulfate cycling, redeposition of cycled sulfate from salar surfaces might be significant for some parts of the Central Depression, because paleo- and active salars can be found in this area (Finstad et al., 2016). However, as discussed above (p. 61 f.), low NaCl concentrations and Na/Cl ratios $\neq 1$ indicate that redeposition of cycled sulfate from salar surfaces is insignificant for the analyzed samples (Voigt et al., 2020).

Coastal areas between 600 and 1200 m asl frequently receive moisture from fog build of stratocumulus clouds expanding from the Pacific Ocean (Cáceres et al., 2007; Cereceda et al., 2008; Schween et al., 2020) allowing biological activity and effective sulfate cycling. Additionally, fog may transport marine aerosols leading to the deposition of marine sulfate and $SAS_{(DMS)}$. Changes in the relative amount of these two sulfate source and variabilities in the degree of sulfate cycling can be identified using $\Delta^{17}O_{SO_4}$, $\delta^{18}O_{SO_4}$, and $\delta^{34}S_{SO_4}$ (Figure 3.9). In the northern part of the Atacama Desert the Coastal Cordillera is intersected by deep canyons, through which this advective fog penetrates further inland. Because fog mainly follows the base of the canyon, possible moisture supply to the top of the canyon depends on the canyon depth and the distance from the coast. In transect A, samples were taken at the top of the Tana Canyon. Samples taken closest to the coastal cliff (Ata17-079a and Ata17-080a) show highest $\Delta^{17}O_{SO_4}$ values within this transect (0.69 ± 0.07‰ and 0.64 ± 0.07‰, respectively). Towards the end of the canyon $\Delta^{17}O_{SO_4}$ decreases while $\delta^{18}O_{SO_4}$ increases, and $\delta^{34}S_{SO_4}$ remains relatively constant (Figure 3.4). A higher marine sulfate contribution towards the end of the canyon could explain the decreasing $\Delta^{17}O_{SO_4}$ values, however, decreasing $\delta^{34}S_{SO_4}$ values do not support this possibility (Figure 3.9). The inverse relationship between $\Delta^{17}O_{SO_4}$ and $\delta^{18}O_{SO_4}$ towards the end of the canyon indicates an increasing degree of biological sulfate cycling due to increasing moisture supply from fog. In transect B and C, samples taken closest to the coast (Ata17-008a, Ata17-048a) show relatively high $\Delta^{17}O_{SO_4}$ (0.71 ± 0.07‰ and 0.59 ± 0.07‰, respectively) and $\delta^{34}S_{SO_4}$ (19.0 ± 0.1‰ and 19.1 ± 0.1‰, respectively) values indicating contributions from

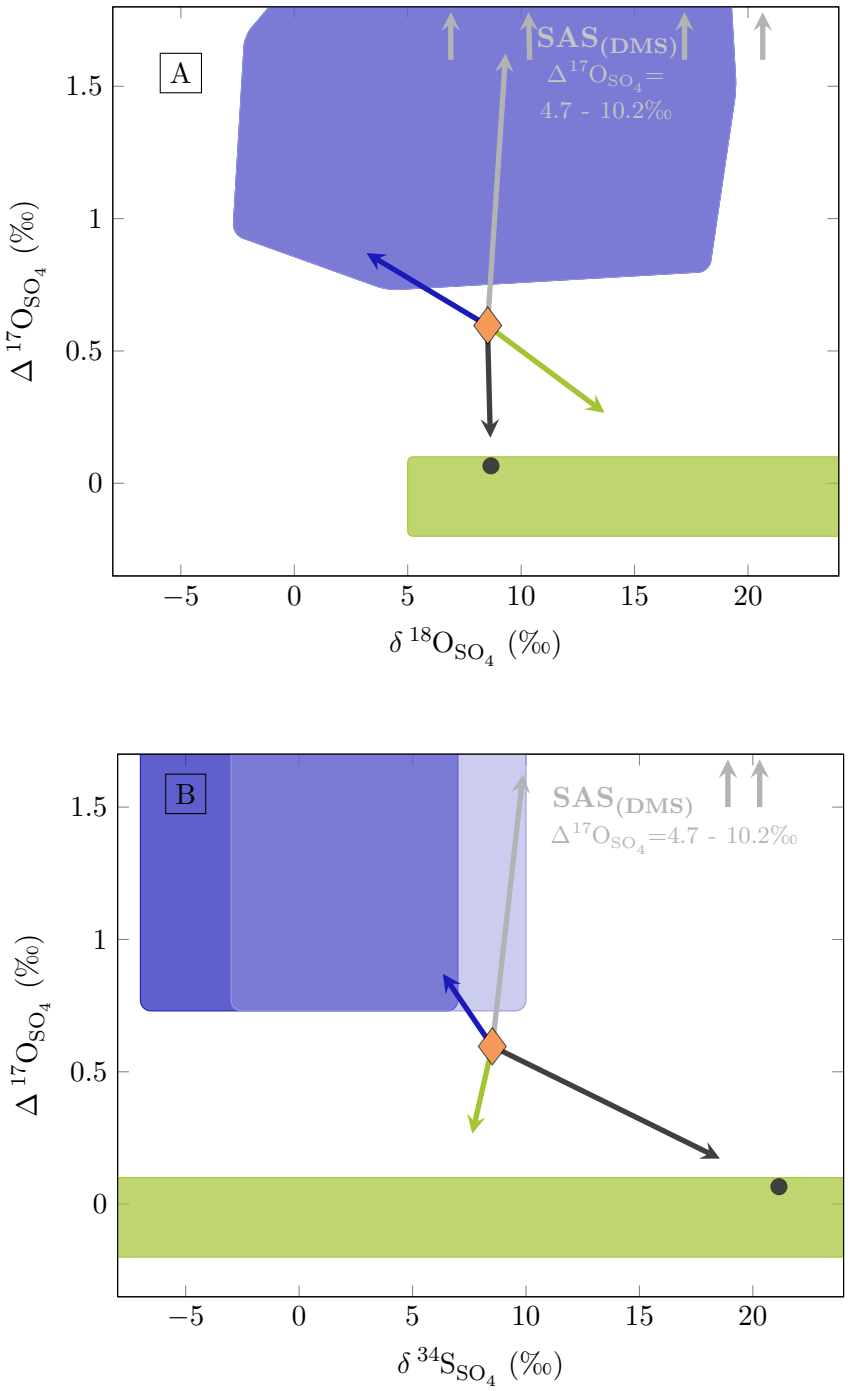

Figure 3.9.: Changes in the isotopic composition of an average sample (orange diamond; average $\Delta^{17}O_{SO_4}$, $\delta^{18}O_{SO_4}$, and $\delta^{34}S_{SO_4}$ values of all samples analyzed in the presented study) due to increasing sulfate source contributions from SAS (blue arrow), $SAS_{(DMS)}$ (gray arrow), marine sulfate (black arrow), and cycled sulfate (green arrow). For further information on the color shading the reader is referred to Figure 3.3.

$SAS_{(DMS)}$. Towards the east, $\Delta^{17}O_{SO_4}$ and $\delta^{34}S_{SO_4}$ values decrease while $\delta^{18}O_{SO_4}$ remains relatively constant indicating decreasing contributions from $SAS_{(DMS)}$ (Figure 3.9). Because in transect B $\delta^{34}S_{SO_4}$ values strongly decline towards the east, possible contributions from marine sulfate might additionally decrease eastwards (Figure 3.9).

In transect D, the Coastal Cordillera is generally higher than 1200 m and all possible moisture sources (groundwater, local and distal precipitation, and fog) are limited. Moisture supply from fog at altitudes >1200 m asl is negligible, and precipitation is generally low (<10 mm yr^{-1}; Houston, 2006). In some parts, a $2-5$ cm thick layer of thenardite (Na_2SO_4) can be found within the first $20-30$ cm below the surface. Because thenardite is highly soluble (solubility: 300 g L^{-1} at 20 °C; Willmes, 1993), this layer generally indicates low amounts of precipitation – otherwise, the thenardite would have been leached out of the sediment. Hence, even though, local precipitation events occasionally occur in this area, water availability is unsteady and probably generally too low for biological activity inhibiting sulfate cycling. Samples from this locality comprises highest $\Delta^{17}O_{SO_4}$ and lowest $\delta^{18}O_{SO_4}$ values (Figure 3.4) supporting a low degree of biological sulfate cycling. Within the high Coastal Cordillera, contributions from sulfate sources other than SAS are generally negligible because transport of marine sulfate and $SAS_{(DMS)}$ above the inversion layer at about 1200 m is unlikely. Additionally, redeposition of surface material only occurs on a rather local scale (see discussion above; p. 61), wherefore contributions from cycled sulfate from remote salar surfaces are implausible for the high Coastal Cordillera. Thus, large positive $\Delta^{17}O_{SO_4}$ values (of $\approx 1‰$) not only suggest a relatively pure isotopic signal from SAS but also indicate the relative absence of biological sulfate cycling and thus, reflect lowest water availability.

subsurface and Na_2SO_4 samples

Subsurface samples generally show low $\delta^{18}O_{SO_4}$ and $\delta^{34}S_{SO_4}$ values compared to respective surface samples (Figure 3.5). This discrepancy might be explained by a subsurface that consists of different materials than the surface, or the subsurface consists of older material. Infiltration of water leads to leaching of soluble salts from the surface and depending on the amount of water to their enrichment within a certain depth in the subsurface (Figure 3.2). A similar chemical composition of sediment surface and subsurface samples (Voigt et al., 2020) indicates

a minor importance of leaching. The observed difference between surface and subsurface may rather represent a change in the sulfate source contribution over time. Lower $\delta^{18}O_{SO_4}$ observed in the subsurface might be explained by lower $\delta^{18}O$ values of atmospheric water leading to lower $\delta^{18}O$ values of SAS. Lower contributions from $SAS_{(DMS)}$ within the subsurface might also lead to lower $\delta^{18}O_{SO_4}$ and $\delta^{34}S_{SO_4}$ values. In addition, lower $\delta^{34}S_{SO_4}$ values might reflect higher contributions from volcanic SAS, while surface samples comprise a higher relative amount of anthropogenic SAS (Figure 1.5) indicating an increase in anthropogenic emissions.

A particular exception are the Na_2SO_4 subsurface samples originate from relatively pure thenardite layers which can be found within the subsurface in some parts of the Atacama Desert ((Figure 3.2) Ericksen, 1983; Chong, 1994). The origin of the Na_2SO_4 and the general formation process of these layers are not yet fully understood. They might result from repeatedly leaching of Na_2SO_4 from the surface into the subsurface over long time scales. $\Delta^{17}O_{SO_4}$, $\delta^{18}O_{SO_4}$, and $\delta^{34}S_{SO_4}$ values of thenardite layers formed this way would represent average values of Na-sulfate deposited over a long time scale. Whereas, the isotopic composition of surface samples reflects recent sulfate source contributions integrated over a much shorter time scale. Thus, changes in the sulfate source contribution over time might have also led to the observed differences in the isotopic composition of Na_2SO_4 subsurface samples compared to respective bulk surface samples dominated by $CaSO_4$. This is supported by the fact that bulk sulfate subsurface samples show similar deviations from respective surface samples (Figure 3.5). However, it is questionable that leaching from the surface leads to the formation of several cm thick nearly pure thenardite layers (Figure 3.2; Ericksen, 1983; Chong, 1994).

The time of sulfate formation within an atmospheric water droplet might be different for Na_2SO_4 and $CaSO_4$ resulting in differences in $\delta^{18}O_{SO_4}$, and $\delta^{34}S_{SO_4}$ values between surface and Na_2SO_4 subsurface samples. Atmospheric water droplets typically comprises pH values between 3 and 6 (Eatough et al., 1994). At such pH values, H_2O_2 is the major oxidant, whereas oxidation via OH may become important when H_2O_2 is consequently depleted (Liang and Jacobson, 1999). During this SO_2 oxidation process, $CaSO_4$ might already precipitates from the water droplet due to its low solubility (=2.4 g L^{-1} at 20 °C Willmes, 1993) compared to the higher solubility of Na_2SO_4 (=300 g L^{-1} at 20 °C Willmes, 1993). Hence, the oxygen isotopic composition of $CaSO_4$ probably mainly reflect the oxidation via H_2O_2, while the oxygen isotopic

composition of Na_2SO_4 might also comprise higher proportions from OH oxidation. Proportions from oxidations via OH would result in lower $\Delta^{17}O_{SO_4}$ and $\delta^{18}O_{SO_4}$ values (see Figure 1.4). Additionally, fractionation effects during the dissolution and oxidation of SO_2 might result in lower $\delta^{34}S_{SO_4}$ values observed in the Na_2SO_4 samples. However, subsurface Na_2SO_4 samples do not show lower $\Delta^{17}O_{SO_4}$ values compared to respective surface samples (Figure 3.5), wherefore the formation time within a water droplet at most play a minor role in isotope fractionation.

Three of the Na_2SO_4 subsurface samples (Ata18-115b, Ata18-116b, and Ata18-121b) originate from the Domeyko Range, 100 km east of Antofagasta. At this locality, a typical soil profile is build from top to bottom of a thin gypsum surface crust, an up to a few cm think thenardite subsurface layer, a gypsum dominated horizon, and up to a few meter think nearly pure nitrate accumulations (see appendix Figure A.4). This extraordinary soil profile might be associated to hydrothermal waters with high concentrations of soluble salt. Hydrothermal waters might have leached Na_2SO_4 from surrounding materials and subsequent evaporation then has led to the concentration of Na_2SO_4. Because the Na_2SO_4 might have been transported the isotopic composition of Na_2SO_4 might differ from the local sulfate source contribution (e.g., surface gypsum crust). However, the gypsum surface crust from this locality has not been analyzed. In addition, the influence of hydrothermal waters or brines on the isotopic composition of sulfate has not yet been investigated.

3.1.5. Conclusion

The combination of $\Delta^{17}O_{SO_4}$, $\delta^{18}O_{SO_4}$, $\delta^{34}S_{SO_4}$, and $^{87}Sr/^{86}Sr$ allows to distinguish between different sulfate sources and post-depositional biological sulfate cycling. SAS originating from atmospheric oxidation of reduced sulfur species from volcanic or anthropogenic emissions, or biogenic sulfur gases (e.g., DMS) is the only sulfate source that comprises a distinct mass-independent ^{17}O anomaly. Hence, positive $\Delta^{17}O_{SO_4}$ values observed in all analyzed samples suggest a significant contribution from SAS to Atacama Desert soils. These results confirm indications from a few data in previous studies (Bao et al., 2004; Bao, 2006; Ewing et al., 2008; Sun et al., 2018) and verify the extensive spatial distribution of SAS by a large number of analyzed samples originating from all over the Atacama Desert.

3. Application

The triple oxygen isotope compositions ($\Delta^{17}O_{SO_4}$ and $\delta^{18}O_{SO_4}$) of all surface samples show a clear trend from volcanic and/or anthropogenic SAS towards cycled sulfate (Figure 3.3). This is interpreted to reflect a gradient in the degree of in-situ biological sulfate cycling and thus in water availability. Redistribution of surface material (e.g., cycled sulfate from salar surfaces) may only occur on a very local scale. Highest $\Delta^{17}O_{SO_4}$ (0.9‰ to 1.1‰) and lowest $\delta^{18}O_{SO_4}$ (−5‰ to 5‰) values indicating the purest SAS signal are observed in samples from the high Coastal Cordillera well above the coastal fog zone (>1200 m asl). Such high $\Delta^{17}O_{SO_4}$ values not only reflect low to negligible contributions from sulfate sources other than SAS, but also indicate the relative absence of in-situ biological sulfate cycling indicating lowest water availability within the Atacama Desert.

To evaluate the marine sulfate contribution the distinct marine $\delta^{34}S_{SO_4}$ value and $^{87}Sr/^{86}Sr$ ratio, and an estimated Andean $\delta^{34}S_{SO_4}$ value and $^{87}Sr/^{86}Sr$ ratio were used. For samples taken within the coastal fog zone (<1200 m), the two obtained marine sulfate contributions correlate on a 1:1 line. Although, possible proportions from $SAS_{(DMS)}$, which comprises $\delta^{34}S_{SO_4}$ values similar to that of marine sulfate, may lead to an overestimation of the marine sulfate source contribution determined by $\delta^{34}S_{SO_4}$. Because $SAS_{(DMS)}$ shows a distinct positive ^{17}O-anomaly, $\Delta^{17}O_{SO_4}$ facilitates to distinguish between $SAS_{(DMS)}$ and marine sulfate (with $\Delta^{17}O_{SO_4} \approx 0‰$). For samples taken above 1200 m, the two approaches to estimate the relative amount of marine sulfate result in significant different contributions. However, because the subsidence inversion layer limits the transport of marine aerosols from the Pacific Ocean to the Atacama Desert, contributions from marine sulfate are expected to be negligible above an altitude of 1200 m.

4.

Summary and Outlook

4.1. Summary

The aim of this work was to identify sulfate sources and post-depositional biogenic alteration processes by investigating the sulfur, strontium, and triple oxygen isotopic composition of sulfates from the Atacama Desert.

The first study dealt with the analytical method to determine $\Delta^{17}O_{SO_4}$ of Atacama Desert sulfate samples. A fast and easy to use protocol for quantitative dissolution of natural Ca-sulfates and conversion into sufficiently pure silver sulfate for accurate and precise pyrolysis analyses was developed. To increase the sample throughput, the previously protocol from Schauer et al. (2012) was simplified by only paying attention to the major contaminants Cl^- and NO_3^- without ion chromatography. To allow the comparison of $\Delta^{17}O_{SO_4}$ results, a normalization procedure was presented. Raw pyrolysis data was normalized to in-house standards with known $\Delta^{17}O_{SO_4}$ values resulting in excellent reproducibility for standards from different laboratories including those using the fluorination method. The overall accuracy was verified by analysis of samples from an Atacama Desert soil pit that was previously analyzed by the fluorination method. Both data sets are identical within analytical uncertainty confirming the accuracy of the developed method.

In the following study, the elaborated method was used to measure $\Delta^{17}O_{SO_4}$ of 55 natural samples from the Atacama Desert. Additionally, the $\delta^{18}O_{SO_4}$ and $\delta^{34}S_{SO_4}$ value of all samples and the $^{87}Sr/^{86}Sr$ ratio of eleven selected samples were determined to identify different sulfate sources and post-depositional alteration processes and to draw conclusions on their relative relevance. A simple two source mixing model was used to estimate the marine sulfate contribution derived from $\delta^{34}S_{SO_4}$ and from $^{87}Sr/^{86}Sr$, respectively (following Rech et al., 2003). For this purpose, the distinct isotope composition of marine sulfate and an estimated Andean endmember were used. While both indicators for the marine sulfate contribution correlate for

samples taken below an altitude of 1200 m with determined marine sulfate contributions of up to 90%, they differ in samples taken above this elevation. The observed scatter may be related to variabilities in $\delta^{34}S_{SO_4}$ and $^{87}Sr/^{86}Sr$ within the non-marine endmember which was not specifically accounted for in the model. In addition, the simple two source mixing model does not critically account for deposition of sulfate that is formed within the atmosphere. $SAS_{(DMS)}$ comprises a marine $\delta^{34}S_{SO_4}$ but positive $\Delta^{17}O_{SO_4}$ values derived from atmospheric reactions. Hence, $\Delta^{17}O_{SO_4}$ facilitates to distinguish between marine sulfate and $SAS_{(DMS)}$. Proportions from $SAS_{(DMS)}$ were identified in samples taken close to the coast below an altitude of 1200 m. The triple oxygen isotopic compositions ($\Delta^{17}O_{SO_4}$ and $\delta^{18}O_{SO_4}$) of all samples show a clear trend from the oxygen isotopic composition of SAS towards those of cycled sulfate which is distinct from the isotopic composition of marine sulfate. This indicates that, even though, a certain contribution from marine sulfate is expected especially in samples taken below 1200 m, the marine sulfate is not the dominating sulfate source for Atacama Desert soils. Positive $\Delta^{17}O_{SO_4}$ values throughout suggest a significant contribution from SAS. Because redistribution of cycled sulfate (e.g., from salar surfaces) is expected to be negligible, the trend is interpreted to reflect a gradient in the degree of in-situ biological sulfate cycling and therewith, water availability.

4.2. Outlook

The results of this thesis demonstrated that analysis of sulfur ($\delta^{34}S$) and triple oxygen ($\Delta^{17}O$ and $\delta^{18}O$) isotopes of sulfate are a suitable tool to identify various sulfate sources and to detect low water availability. However, further investigations are necessary to improve the understanding of sulfate deposition and biological sulfate cycling within Atacama Desert soils.

To be able to compare isotope data from different laboratories and methods, results are generally normalized to international accepted standards. In absence of certified $\Delta^{17}O$ reference Na- or Ca-sulfate material, all presented $\Delta^{17}O_{SO_4}$ data was normalized to in-house standards previously calibrated against in-house standards from the University of Washington (see chapter 2). The accuracy of this approach was verified by comparing the normalized $\Delta^{17}O_{SO_4}$ data to results from other laboratories using the pyrolysis or fluorination method. Even though,

international accepted Ba-sulfate standards are available, which are suitable for fluorination analysis only, they all comprise $\Delta^{17}O_{SO_4} \approx 0‰$. Hence, to improve the general comparability of $\Delta^{17}O_{SO_4}$ data, an international reference Na- or Ca-sulfate material – suitable for pyrolysis and fluorination – with a distinct $\Delta^{17}O_{SO_4}$ value is required.

The observed trend in the triple oxygen isotope composition of all samples is interpreted to reflect a gradient in the degree of in-situ biological sulfate cycling due to variable water availability. Additional biological analysis, e.g., for the amount and the composition of different microbe or plant genomes, may help to verify the hypothesis that $\Delta^{17}O_{SO_4}$ is an indicator for sulfate cycling. Furthermore, analysis of densely taken samples along well-known gradients in water availability, e.g., between 1000 m and 1400 m elevation in areas with frequent fog occurrence, would be useful to verify the potential of $\Delta^{17}O_{SO_4}$ as an indicator for water availability.

In the presented thesis, sulfate sources were identified and sulfate source contributions were estimated using using sulfur, strontium, and triple oxygen isotopes. To better quantify the relative amount of sulfate from each source, the isotopic compositions of SAS and cycled sulfate needs to be better characterized. For this purpose, additional samples from locations with extremely low water availability (e.g., high Coastal Cordillera) and extremely high water availability (e.g., salars or low Coastal Cordillera) should be analyzed. Furthermore, analyzing atmospheric dust collected close to anthropogenic or volcanic emissions may help to further narrow the range in the isotopic composition ($\Delta^{17}O_{SO_4}$, $\delta^{18}O$, and $\delta^{34}S$) of respective sulfate sources. Additional samples from the high Coastal Cordillera should be analyzed to verify that the samples with the highest $\Delta^{17}O_{SO_4}$ values observed in the presented study indeed reflect the isotopic composition of SAS.

The isotopic composition of sulfate sampled along vertical profiles may help to identify changes in the sulfate source contribution or in water availability over time. This was already done by previous studies (Ewing et al., 2008; Sun et al., 2018). However, changes in the isotopic composition of sulfate were only observed 34 m below the surface indicating the onset of hyperaridity in the Atacama Desert (Sun et al., 2018). Especially locations which today can be easily classified – e.g., as Precordillera and alluvial fans (high water availability), or

high Coastal Cordillera (low water availability) – are of special interest to further investigate possible changes in the sulfate source contribution and water availability over time.

References

B. Alexander, D. J. Allman, H. M. Amos, T. D. Fairlie, J. Dachs, D. A. Hegg and R. S. Sletten (2012). 'Isotopic constraints on the formation pathways of sulfate aerosol in the marine boundary layer of the subtropical northeast Atlantic Ocean'. *Journal of Geophysical Research Atmospheres*, **117 6**, 1–17.

B. Alexander, R. J. Park, D. J. Jacob and S. Gong (2009). 'Transition metal-catalyzed oxidation of atmospheric sulfur: Global implications for the sulfur budget'. *Journal of Geophysical Research Atmospheres*, **114 2**, 1–13.

B. Alexander, J. Savarino, N. I. Barkov, R. J. Delmas and M. H. Thiemens (2002). 'Climate driven changes in the oxidation pathways of atmospheric sulfur'. *Geophysical Research Letters*, **29 14**.

R. W. Allmendinger and G. González (2010). 'Invited review paper: Neogene to Quaternary tectonics of the coastal Cordillera, northern Chile'. *Tectonophysics*, **495 1-2**, 93–110.

F. Álvarez, M. Reich, A. Pérez-Fodich, G. Snyder, Y. Muramatsu, G. Vargas and U. Fehn (2015). 'Sources, sinks and long-term cycling of iodine in the hyperarid Atacama continental margin'. *Geochimica et Cosmochimica Acta*, **161**, 50–70.

A. Amrani, W. Said-Ahmad, Y. Shaked and R. P. Kiene (2013). 'Sulfur isotope homogeneity of oceanic DMSP and DMS'. *Proceedings of the National Academy of Sciences of the United States of America*, **110 46**, 18413–18418.

D. Babikov, B. K. Kendrick, R. B. Walker, R. T. Pack, P. Fleurat-Lesard and R. Schinke (2003). 'Formation of ozone: Metastable states and anomalous isotope effect'. *Journal of Chemical Physics*, **119 5**, 2577–2589.

N. Balci, W. C. Shanks, B. Mayer and K. W. Mandernack (2007). 'Oxygen and sulfur isotope systematics of sulfate produced by bacterial and abiotic oxidation of pyrite'. *Geochimica et Cosmochimica Acta*, **71 15**, 3796–3811.

H. Bao (2006). 'Purifying barite for oxygen isotope measurement by dissolution and reprecipitation in a chelating solution'. *Analytical Chemistry*, **78 1**, 304–309.

H. Bao (2015). 'Sulfate: A time capsule for Earth's O_2, O_3, and H_2O'. *Chemical Geology*, **395**, 108–118.

H. Bao, X. Cao and J. A. Hayles (2016). 'Triple Oxygen Isotopes: Fundamental Relationships and Applications'. *Annual Review of Earth and Planetary Sciences*, **44 1**, 463–492.

H. Bao, K. A. Jenkins, M. Khachaturyan and G. C. Díaz (2004). 'Different sulfate sources and their post-depositional migration in Atacama soils'. *Earth and Planetary Science Letters*, **224**, 577–587.

H. Bao, J. R. Lyons and C. Zhou (2008). 'Triple oxygen isotope evidence for elevated CO_2 levels after a Neoproterozoic glaciation'. *Nature*, **453**, 504–506.

H. Bao, G. M. Michalski and M. H. Thiemens (2001a). 'Sulfate oxygen-17 anomalies in desert varnishes'. *Geochimica et Cosmochimica Acta*, **65 13**, 2029–2036.

H. Bao and M. H. Thiemens (2000). 'Generation of O_2 from $BaSO_4$ using a CO_2-laser fluorination system for simultaneous analysis of $\delta^{18}O$ and $\delta^{17}O$'. *Analytical Chemistry*, **72 17**, 4029–4032.

H. Bao, M. H. Thiemens and K. Heine (2001b). 'Oxygen-17 excesses of the Central Namib gypcretes: spatial distribution'. *Earth and Planetary Science Letters*, **192**, 125–135.

H. Bao, M. H. Thiemens, D. B. Loope and X. L. Yuan (2003). 'Sulfate oxygen-17 anomaly in an Oligocene ash bed in mid-North America: Was it the dry fogs?' *Geophysical Research Letters*, **30 16**.

E. Barkan (2007). 'Diffusivity fractionations of $H_2{}^{16}O$ / $H_2{}^{17}O$ and $H_2{}^{16}O$ / $H_2{}^{18}O$ in air and their implications for isotope hydrology'. *Rapid Communications in Mass Spectrometry*, **21**, 2999–3005.

M. C. Barth, P. J. Rasch, J. T. Kiehl, C. M. Benkovitz and S. E. Schwartz (2000). 'Sulfur chemistry in the National Center for Atmospheric Research Community Climate Model: Description, evaluation, features, and sensitivity to aqueous chemistry'. *Journal of Geophysical Research Atmospheres*, **105 D1**, 1387–1415.

T. F. Berglen, T. K. Berntsen, I. S. Isaksen and J. K. Sundet (2004). 'A global model of the coupled sulfur/oxidant chemistry in the troposphere: The sulfur cycle'. *Journal of Geophysical Research D: Atmospheres*, **109 19**, 1–27.

R. H. Betts and R. H. Voss (1970). 'The kinetics of oxygen exchange between the sulfite ion and water'. *Canadian Journal of Chemistry*, **48 13**, 2035–2041.

I. N. Bindeman, J. M. Eiler, B. A. Wing and J. Farquhar (2007). 'Rare sulfur and triple oxygen isotope geochemistry of volcanogenic sulfate aerosols'. *Geochimica et Cosmochimica Acta*, **71 9**, 2326–2343.

M. E. Böttcher, B. Thamdrup and T. Vennemann (2001). 'Oxygen and sulfur isotope fractionation during anaerobic bacterial disporportioanation of elemental sulfur'. *Geochimica et Cosmochimica Acta*, **65 10**, 1601–1609.

G. J. Bowen and B. Wilkinson (2002). 'Spatial distribution of δ^{18}O in meteoric precipitation'. *Geology*, **30 4**, 315–318.

A. S. Bradley, W. D. Leavitt and D. T. Johnston (2011). 'Revisiting the dissimilatory sulfate reduction pathway'. *Geobiology*, **9 5**, 446–457.

G. W. Brass (1975). 'The effect of weathering on the distribution of strontium isotopes in weathering profiles'. *Geochimica et Cosmochimica Acta*, **39 12**, 1647–1653.

P. Brimblecombe (2013). *The Global Sulfur Cycle*. Elsevier Ltd., 2 ed.

A. Burke, T. M. Present, G. Paris, E. C. Rae, B. H. Sandilands, J. Gaillardet, B. Peucker-Ehrenbrink, W. W. Fischer, J. W. McClelland, R. G. Spencer, B. M. Voss and J. F. Adkins (2018). 'Sulfur isotopes in rivers: Insights into global weathering budgets, pyrite oxidation, and the modern sulfur cycle'. *Earth and Planetary Science Letters*, **496**, 168–177.

W. H. Burke, R. E. Denison, E. A. Hetherington, R. B. Koepnick, H. F. Nelson and J. B. Otto (1982). 'Variation of seawater $^{87}Sr/^{86}Sr$ throughout Phanerozoic time'. *Geology*, **10**, 516–519.

L. Cáceres, B. Gómez-Silva, X. Garró, V. Rodríguez, V. Monardes and C. P. McKay (2007). 'Relative humidity patterns and fog water precipitation in the Atacama Desert and biological implications'. *Journal of Geophysical Research: Biogeosciences*, **112 4**, 1–11.

X. Cao and H. Bao (2013). 'Dynamic model constraints on oxygen-17 depletion in atmospheric O_2 after a snowball Earth'. *Proceedings of the National Academy of Sciences of the United States of America*, **110 36**, 14546–14550.

X. Cao and H. Bao (2021). 'Small Triple Oxygen Isotope Variations in Sulfate: Mechanisms and Applications'. *Reviews in Mineralogy and Geochemistry*, **86 1**, 463–488.

M. Casado, A. Cauquoin, A. Landais, D. Israel, A. Orsi, E. Pangui, J. Landsberg, E. Kerstel, F. Prie and J. F. Doussin (2016). 'Experimental determination and theoretical framework of kinetic fractionation at the water vapour-ice interface at low temperature'. *Geochimica et Cosmochimica Acta*, **174**, 54–69.

P. Cereceda, H. Larrain, P. Osses, M. Farías and I. Egaña (2008). 'The spatial and temporal variability of fog and its relation to fog oases in the Atacama Desert, Chile'. *Atmospheric Research*, **87**, 312–323.

S. Chakraborty, P. Yanchulova and M. H. Thiemens (2013). 'Mass-Independent Oxygen Isotopic Partitioning During Gas-Phase SiO_2 Formation'. *Science*, **342**, 463–466.

H. Chiba, M. Kusakabe, S. I. Hirano, S. Matsuo and S. Somiya (1981). 'Oxygen isotope fractionation factors between anhydrite and water from 100 to 550 ℃'. *Earth and Planetary Science Letters*, **53 1**, 55–62.

G. Chong (1994). 'The Nitrate Deposits of Chile'. In 'Reutter KJ., Scheuber E., Wigger P.J. (eds) Tectonics of the Southern Central Andes', Springer, Berlin, Heidelberg, 303–316.

R. N. Clayton (2002). 'Self-shielding in the solar nebula'. *Nature*, **415**, 860–861.

R. N. Clayton, L. Grossman and T. K. Mayeda (1973). 'A component of primitive nuclear composition in carbonaceous meteorites'. *Science*, **182**, 485–488.

T. B. Coplen, J. a. Hopple, J. K. Böhlke, H. S. Peiser, S. E. Rieder, H. R. Krouse, K. J. R. Rosman, T. Ding, R. D. J. Vocke, K. M. Révész, a. Lamberty, P. Taylor and P. D. Bièvre (2002). 'Compilation of minimum and maximum isotope ratios of selected elements in naturally occurring terrestrial materials and reagents'. *US Geological Survey*, 110.

B. R. Cowie and D. T. Johnston (2016). 'High-precision measurement and standard calibration of triple oxygen isotopic compositions ($\delta^{18}O$, $\Delta'^{17}O$) of sulfate by F_2 laser fluorination'. *Chemical Geology*, **440**, 50–59.

H. Craig, L. I. Gordon and Y. Horibe (1963). 'Isotopic exchange effects in the evaporation of water: 1. Low-temperature experimental results'. *Journal of Geophysical Research*, **68 17**, 5079–5087.

P. W. Crockford, B. R. Cowie, D. T. Johnston, P. F. Hoffman, I. Sugiyama, A. Pellerin, T. H. Bui, J. Hayles, G. P. Halverson, F. A. Macdonald and B. A. Wing (2016). 'Triple oxygen and multiple sulfur isotope constraints on the evolution of the post-Marinoan sulfur cycle'. *Earth and Planetary Science Letters*, **435**, 74–83.

N. Dauphas and E. A. Schauble (2016). 'Mass Fractionation Laws, Mass-Independent Effects, and Isotopic Anomalies'. *Annual Review of Earth and Planetary Sciences*, **44**, 709–783.

W. L. Davis, I. de Pater and C. P. McKay (2010). 'Rain infiltration and crust formation in the extreme arid zone of the Atacama Desert, Chile'. *Planetary and Space Science*, **58 4**, 616–622.

G. Dominguez, T. Jackson, L. Brothers, B. Barnett, B. Nguyen and M. H. Thiemens (2008). 'Discovery and measurement of an isotopically distinct source of sulfate in Earth's atmosphere'. *Proceedings of the National Academy of Sciences of the United States of America*, **105 35**, 12769–12773.

T. J. Dunai, G. A. González López and J. Juez-Larré (2005). 'Oligocene-Miocene age of aridity in the Atacama Desert revealed by exposure dating of erosion-sensitive landforms'. *Geology*, **33 4**, 321–324.

D. J. Eatough, F. M. Caka and R. J. Farber (1994). 'The Conversion of SO_2 to Sulfate in the Atmosphere'. *Israel Journal of Chemistry*, **34 3-4**, 301–314.

G. E. Ericksen (1981). 'Geology and Origin of the Chilean Nitrate Deposits'. *Geological survey professional paper*, 1–37.

G. E. Ericksen (1983). 'The chilean nitrate deposits'. *American Scientist*, **71 3**, 366–374.

L. A. Evenstar, A. J. Hartley, F. M. Stuart, A. E. Mather, C. M. Rice and G. Chong (2009). 'Multiphase development of the Atacama Planation Surface recorded by cosmogenic ^{3}He exposure ages: Implications for uplift and Cenozoic climate change in Western South America'. *Geology*, **37 1**, 27–30.

L. A. Evenstar, A. E. Mather, A. J. Hartley, F. M. Stuart, R. S. Sparks and F. J. Cooper (2017). 'Geomorphology on geologic timescales: Evolution of the late Cenozoic Pacific paleosurface in Northern Chile and Southern Peru'. *Earth-Science Reviews*, **171**, 1–27.

S. A. Ewing, B. Sutter, J. Owen, K. Nishiizumi, W. Sharp, S. S. Cliff, K. Perry, W. Dietrich, C. P. McKay and R. Amundson (2006). 'A threshold in soil formation at Earth's arid-hyperarid transition'. *Geochimica et Cosmochimica Acta*, **70 21**, 5293–5322.

S. A. Ewing, W. Yang, D. J. DePaolo, G. Michalski, C. Kendall, B. W. Stewart, M. Thiemens and R. Amundson (2008). 'Non-biological fractionation of stable Ca isotopes in soils of the Atacama Desert, Chile'. *Geochimica et Cosmochimica Acta*, **72**, 1096–1110.

J. Farquhar, D. E. Canfield, A. Masterson, H. Bao and D. Johnston (2008). 'Sulfur and oxygen isotope study of sulfate reduction in experiments with natural populations from Fællestrand, Denmark'. *Geochimica et Cosmochimica Acta*, **72 12**, 2805–2821.

J. Feichter, E. Kjellström, H. Rodhe, F. Dentener, J. Lelieveld and G. J. Roelofs (1996). 'Simulation of the tropospheric sulfur cycle in a global climate model'. *Atmospheric Environment*, **30 10-11**, 1693–1707.

K. Finstad, M. Pfeiffer and R. Amundson (2014). 'Hyperarid Soils and the Soil Taxonomy'. *Soil Science Society of America Journal*, **78 6**, 1845–1851.

K. Finstad, M. Pfeiffer, G. McNicol, J. Barnes, C. Demergasso, G. Chong and R. Amundson (2016). 'Rates and geochemical processes of soil and salt crust formation in Salars of the Atacama Desert, Chile'. *Geoderma*, **284**, 57–72.

References

H. Frenkel, Z. Gerstl and J. R. van de Veen (1986). 'Determination of gypsum and cation exchange capacity in arid soils by a resin method'. *Geoderma*, **39**, 67–77.

C. Gamboa, L. Godfrey, C. Herrera, E. Custodio and A. Soler (2019). 'The origin of solutes in groundwater in a hyper-arid environment: A chemical and multi-isotope approach in the Atacama Desert, Chile'. *Science of the Total Environment*, **690**, 329–351.

Y. Q. Gao and R. A. Marcus (2001). 'Strange and unconventional isotope effects in ozone formation'. *Science*, **293**, 259–263.

M. Garcia and G. Hérail (2005). 'Fault-related folding, drainage network evolution and valley incision during the Neogene in the Andean Precordillera of Northern Chile'. *Geomorphology*, **65**, 279–300.

L. Geng, A. J. Schauer, S. A. Kunasek, E. D. Sofen, J. Erbland, J. Savarino, D. J. Allman, R. S. Sletten and B. Alexander (2013). 'Analysis of oxygen-17 excess of nitrate and sulfate at sub-micromole levels using the pyrolysis method'. *Rapid Communications in Mass Spectrometry*, **27**, 2411–2419.

S. R. Gislason and P. Torssander (2006). 'Response of sulfate concentration and isotope composition in Icelandic rivers to the decline in global atmospheric SO_2 emissions into the North Atlantic region'. *Environmental Science and Technology*, **40 3**, 680–686.

L. V. Godfrey, C. Herrera, C. Gamboa and R. Mathur (2019). 'Chemical and isotopic evolution of groundwater through the active Andean arc of Northern Chile'. *Chemical Geology*, **518**, 32–44.

E. Harris, B. Sinha, P. Hoppe, J. N. Crowley, S. Ono and S. Foley (2012). 'Sulfur isotope fractionation during oxidation of sulfur dioxide: Gas-phase oxidation by OH radicals and aqueous oxidation by H_2O_2, O_3 and iron catalysis'. *Atmospheric Chemistry and Physics*, **12 1**, 407–424.

E. Harris, B. Sinha, P. Hoppe and S. Ono (2013). 'High-precision measurements of ^{33}S and ^{34}S fractionation during SO_2 oxidation reveal causes of seasonality in SO_2 and sulfate isotopic composition'. *Environmental Science and Technology*, **47 21**, 12174–12183.

A. J. Hartley and G. Chong (2002). 'Late Pliocene age for the Atacama Desert: Implications for the desertification of western South America'. *Geology*, **30 1**, 43–46.

A. J. Hartley and L. Evenstar (2010). 'Cenozoic stratigraphic development in the north Chilean forearc: Implications for basin development and uplift history of the Central Andean margin'. *Tectonophysics*, **495**, 67–77.

A. J. Hartley, G. May, G. Chong, P. Turner, S. J. Kape and E. J. Jolley (2000). 'Development of a continental forearc: A Cenozoic example from the Central Andes, northern Chile'. *Geology*, **28 4**, 331–334.

D. Herwartz (2021). 'Triple Oxygen Isotope Variations in Earth's Crust'. *Reviews in Mineralogy and Geochemistry*, **86**, 291–322.

J. Hill-Falkenthal, A. Priyadarshi, J. Savarino and M. Thiemens (2013). 'Seasonal variations in ^{35}S and $\Delta^{17}O$ of sulfate aerosols on the Antarctic plateau'. *Journal of Geophysical Research Atmospheres*, **118**, 9444–9455.

M. E. Hofmann, B. Horváth and A. Pack (2012). 'Triple oxygen isotope equilibrium fractionation between carbon dioxide and water'. *Earth and Planetary Science Letters*, **319-320**, 159–164.

J. Houston (2006). 'Variability of Precipitation in the Atacama Desert: its causes and hydrological impact'. *International Journal of Climatology*, **26**, 2181–1298.

J. Houston and A. J. Hartley (2003). 'The central andean west-slope rainshadow and its potential contribution to the origin of hyper-aridity in the Atacama Desert'. *International Journal of Climatology*, **23 12**, 1453–1464.

C. Janssen, J. Guenther, K. Mauersberger and D. Krankowsky (2001). 'Kinetic origin of the ozone isotope effect: A critical analysis of enrichments and rate coefficients'. *Physical Chemistry Chemical Physics*, **3 21**, 4718–4721.

K. A. Jenkins and H. Bao (2006). 'Multiple oxygen and sulfur isotope compositions of atmospheric sulfate in Baton Rouge, LA, USA'. *Atmospheric Environment*, **40 24**, 4528–4537.

Q. Jianjun, H. Ning, D. Guangrong and Z. Weimin (2001). 'The role and significance of the Gobi Desert pavement in controlling sand movement on the cliff top near the Dunhuang Magao Grottoes'. *Journal of Arid Environments*, **48 3**, 357–371.

C. A. Johnson, M. A. Mast and C. L. Kester (2001). 'Use of $^{17}O/^{16}O$ to trace atmospherically-deposited sulfate in surface waters: A case study in alpine watersheds in the Rocky Mountains'. *Geophysical Research Letters*, **28 23**, 4483–4486.

D. T. Johnston, J. Farquhar and D. E. Canfield (2007). 'Sulfur isotope insights into microbial sulfate reduction: When microbes meet models'. *Geochimica et Cosmochimica Acta*, **71 16**, 3929–3947.

D. T. Johnston, B. C. Gill, A. Masterson, E. Beirne, K. L. Casciotti, A. N. Knapp and W. Berelson (2014). 'Placing an upper limit on cryptic marine sulphur cycling'. *Nature*, **513**, 530–533.

References

J. C. Johnston and M. H. Thiemens (1997). 'The isotopic composition of tropospheric ozone in three environments'. *Journal of Geophysical Research Atmospheres*, **102 21**, 25395–25404.

T. E. Jordan, C. Herrera L., L. V. Godfrey, S. J. Colucci, C. Gamboa P., J. Urrutia M., G. González L. and J. F. Paul (2019). 'Isotopic characteristics and paleoclimate implications of the extreme precipitation event of march 2015 in Northern Chile'. *Andean Geology*, **46 1**, 1–31.

D. Karátson, T. Telbisz and G. Wörner (2012). 'Erosion rates and erosion patterns of Neogene to Quaternary stratovolcanoes in the Western Cordillera of the Central Andes: An SRTM DEM based analysis'. *Geomorphology*, **139-140**, 122–135.

S. Klipsch, D. Herwartz and M. Staubwasser (2021a). 'Optimizing sulfate pyrolysis triple oxygen isotope analysis for samples from desert environments'. *Rapid Communications in Mass Spectrometry*, **35 14**, e9102.

S. Klipsch, C. Voigt, D. Herwartz, M. E. Böttcher and M. Staubwasser (2021b). 'Identifying Sulfate Sources and Water Availability using Triple Oxygen and Sulfur Isotopes'. In 'Goldschmidt Conference Abstracts', .

S. Kobayashi, H. Imai and H. Yurimoto (2003). 'New extreme ^{16}O-rich reservoir in the early solar system'. *Geochemical Journal*, **37 6**, 663–669.

I. Kohl and H. Bao (2011). 'Triple-oxygen-isotope determination of molecular oxygen incorporation in sulfate produced during abiotic pyrite oxidation (pH=2-11)'. *Geochimica et Cosmochimica Acta*, **75 7**, 1785–1798.

A. Koprivova and S. Kopriva (2016). 'Sulfation pathways in plants'. *Chemico-Biological Interactions*, **259**, 23–30.

E. Kreyszig (2006). *Advanced Engineering Mathematics*. John Wiley & Sons, Inc., 9th ed.

H. R. Krouse and B. Mayer (2000). 'Sulphur and Oxygen Isotopes in Sulphate'. *Environmental Tracers in Subsurface Hydrology*, 195–231.

S. A. Kunasek, B. Alexander, E. J. Steig, E. D. Sofen, T. L. Jackson, M. H. Thiemens, J. R. McConnell, D. J. Gleason and H. M. Amos (2010). 'Sulfate sources and oxidation chemistry over the past 230 years from sulfur and oxygen isotopes of sulfate in a West Antarctic ice core'. *Journal of Geophysical Research Atmospheres*, **115 D18313**, 1–13.

M. Kusakabe and B. W. Robinson (1977). 'Oxygen and sulfur isotope equilibria in the $BaSO_4$ - HSO_4^- - H_2O system from 110 to 350 ℃ and applications'. *Geochimica et Cosmochimica Acta*, **41 8**, 1033–1040.

A. Landais, H. C. Steen-Larsen, M. Guillevic, V. Masson-Delmotte, B. Vinther and R. Winkler (2012). 'Triple isotopic composition of oxygen in surface snow and water vapor at NEEM (Greenland)'. *Geochimica et Cosmochimica Acta*, **77**, 304–316.

E. Le Gendre, E. Martin, B. Villemant, P. Cartigny and N. Assayag (2017). 'A simple and reliable anion-exchange resin method for sulfate extraction and purification suitable for multiple O- and S-isotope measurements'. *Rapid Communications in Mass Spectrometry*, **31 1**, 137–144.

C. C. W. Lee and M. H. Thiemens (2001). 'The δ^{17}O and δ^{18}O measurements of atmospheric sulfate from a coastal and high alpine region: A mass-independent isotopic anomaly'. *Journal of Geophysical Research Atmospheres*, **106 D15**, 17359–17373.

J. Li, Y. L. Zhang, F. Cao, W. Zhang, M. Fan, X. Lee and G. Michalski (2020). 'Stable Sulfur Isotopes Revealed a Major Role of Transition-Metal Ion-Catalyzed SO_2 Oxidation in Haze Episodes'. *Environmental Science and Technology*, **54 5**, 2626–2634.

J. Liang and M. Z. Jacobson (1999). 'A study of sulfur dioxide oxidation pathways over a range of liquid water contents, pH values, and temperatures'. *Journal of Geophysical Research Atmospheres*, **104 D11**, 13749–13769.

M. C. Liu, K. D. McKeegan, J. N. Goswami, K. K. Marhas, S. Sahijpal, T. R. Ireland and A. M. Davis (2009). 'Isotopic records in CM hibonites: Implications for timescales of mixing of isotope reservoirs in the solar nebula'. *Geochimica et Cosmochimica Acta*, **73 17**, 5051–5079.

J. R. Lyons and E. D. Young (2005). 'CO self-shielding as the origin of oxygen isotope anomalies in the early solar nebula'. *Nature*, **435**, 317–320.

S. H. Manian, H. C. Urey and W. Bleakney (1934). 'An Investigation of the Relative Abundance of the Oxygen Isotopes O^{16}:O^{18} in Stone Meteorites'. *Journal of the American Chemical Society*, **56 12**, 2601–2609.

J. L. Mann, R. D. J. Vocke and W. R. Kelly (2009). 'Revised δ^{34}S reference values for IAEA sulfur isotope reference materials S-2 and S-3'. *Rapid Communications in Mass Spectrometry*, **23**, 1116–1124.

R. A. Marcus (2004). 'Mass-independent isotope effect in the earliest processed solids in the solar system: A possible chemical mechanism'. *Journal of Chemical Physics*, **121 17**, 8201–8211.

E. Martin, S. Bekki, C. Ninin and I. Bindeman (2014). 'Isotopic insight into volcanic sulfate formation in the troposphere'. *Journal of Geophysical Research: Atmospheres*, **119 22**, 12660–12673.

T. A. Mather, J. R. McCabe, V. K. Rai, M. H. Thiemens, D. M. Pyle, T. H. Heaton, H. J. Sloane and G. R. Fern (2006). 'Oxygen and sulfur isotopic composition of volcanic sulfate aerosol at the point of emission'. *Journal of Geophysical Research Atmospheres*, **111 18**, 1–9.

Y. Matsuhisa, J. R. Goldsmith and R. N. Clayton (1978). 'Mechanisms of hydrothermal crystallization of quartz at 250 ℃ and 15 kbar'. *Geochimica et Cosmochimica Acta*, **42**, 173–182.

K. Mauersberger (1987). 'Ozone Isotope Measurements in the Stratosphere'. *Geophysical Research Letters*, **14 1**, 80–83.

K. Mauersberger, D. Krankowsky, C. Janssen and R. Schinke (2005). 'Assessment of the ozone isotope effect'. *Advances in Atomic, Molecular and Optical Physics*, **50**, 1–54.

J. M. McArthur (1994). 'Recent trends in strontium isotope stratigraphy'. *Terra Nova*, **6 4**, 331–358.

J. M. McCrea (1950). 'On the isotopic chemistry of carbonates and a paleotemperature scale'. *The Journal of Chemical Physics*, **18 6**, 849–857.

W. Meier-Augenstein and A. Schimmelmann (2019). 'A guide for proper utilisation of stable isotope reference materials'. *Isotopes in Environmental and Health Studies*, **55 2**, 113–128.

G. Michalski, J. K. Böhlke and M. Thiemens (2004). 'Long term atmospheric deposition as the source of nitrate and other salts in the Atacama Desert, Chile: New evidence from mass-independent oxygen isotopic compositions'. *Geochimica et Cosmochimica Acta*, **68 20**, 4023–4038.

M. F. Miller and A. Pack (2021). 'Why Measure ^{17}O? Historical Perspective, Triple-Isotope Systematics and Selected Applications'. *Reviews in Mineralogy and Geochemistry*, **86 1**, 1–34.

J. Mohren, S. A. Binnie, B. Ritter and T. J. Dunai (2020). 'Development of a steep erosional gradient over a short distance in the hyperarid core of the Atacama Desert, northern Chile'. *Global and Planetary Change*, **184**, 103068.

R. Mörchen, E. Lehndorff, F. A. Diaz, G. Moradi, R. Bol, B. Fuentes, E. Klumpp and W. Amelung (2019). 'Carbon accrual in the Atacama Desert'. *Global and Planetary Change*, **181**, 102993.

H. Mukai, A. Tanaka, T. Fujii, Y. Zeng, Y. Hong, J. Tang, S. Guo, H. Xue, Z. Sun, J. Zhou, D. Xue, J. Zhao, G. Zhai, J. Gu and P. Zhai (2001). 'Regional characteristics of sulfur and lead isotope ratios in the atmosphere at several Chinese urban sites'. *Environmental Science and Technology*, **35 6**, 1064–1071.

R. C. Muñoz, R. A. Zamora and J. A. Rutllant (2011). 'The coastal boundary layer at the eastern margin of the southeast Pacific (23.4°S, 70.4°W): cloudiness-conditioned climatology'. *Journal of Climate*, **24 4**, 1013–1033.

L. Newman, H. R. Krouse and V. a. Grinenko (1991). 'Sulphur Isotope Variations in the Atmosphere'. *Stable Isotopes in the Assessment of Natural and Anthropogenic Sulphur in the Environment*, 133–176.

H. Nguyen, A. Evans, C. Lucas, I. Smith and B. Timbal (2013). 'The hadley circulation in reanalyses: Climatology, variability, and Change'. *Journal of Climate*, **26 10**, 3357–3376.

H. Nielsen (1974). 'Isotopic composition of the major contributors to atmospheric sulfur'. *Tellus*, **26 1-2**, 213–221.

J. C. Obert, C. münker, M. Staubwasser, D. Herwartz, K. Reicherter and G. Chong (2022). '230Th dating of gypsum from lacustrine, brackish-marine and terrestrial environments'. *Chemical Geology*, **607**, 121019.

C. D. O'Dowd and G. De Leeuw (2007). 'Marine aerosol production: A review of the current knowledge'. *Philosophical Transactions of the Royal Society A: Mathematical, Physical and Engineering Sciences*, **365 1856**, 1753–1774.

A. Pack (2021). 'Isotopic Traces of Atmospheric O_2 in Rocks, Minerals and Melts'. *Reviews in Mineralogy and Geochemistry*, **86**, 217–240.

A. Pack and D. Herwartz (2014). 'The triple oxygen isotope composition of the Earth mantle and understanding $\Delta^{17}O$ variations in terrestrial rocks and minerals'. *Earth and Planetary Science Letters*, **390**, 138–145.

M. R. Palmer (1992). 'Controls over the chloride concentration of submarine hydrothermal vent fluids: evidence from Sr/Ca and $^{87}Sr/^{86}Sr$ ratios'. *Earth and Planetary Science Letters*, **109**, 37–46.

A. Pérez-Fodich, M. Reich, F. Álvarez, G. T. Snyder, R. Schoenberg, G. Vargas, Y. Muramatsu and U. Fehn (2014). 'Climate change and tectonic uplift triggered the formation of the atacama desert's giant nitrate deposits'. *Geology*, **42 3**, 251–254.

C. Pisapia, M. Chaussidon, C. Mustin and B. Humbert (2007). 'O and S isotopic composition of dissolved and attached oxidation products of pyrite by Acidithiobacillus ferrooxidans: Comparison with abiotic oxidations'. *Geochimica et Cosmochimica Acta*, **71 10**, 2474–2490.

C. V. Putnis, M. Kowacz and A. Putnis (2008). 'The mechanism and kinetics of DTPA-promoted dissolution of barite'. *Applied Geochemistry*, **23 9**, 2778–2788.

P. J. Rasch, M. C. Barth, J. T. Kiehl, S. E. Schwartz and C. M. Benkovitz (2000). 'A description of the global sulfur cycle and its controlling processes in the National Center for Atmospheric Research Community Climate Model, Version 3'. *Journal of Geophysical Research Atmospheres*, **105 D1**, 1367–1385.

J. A. Rech, J. Quade and W. S. Hart (2003). 'Isotopic evidence for the source of Ca and S in soil gypsum, anhydrite and calcite in the Atacama Desert, Chile'. *Geochimica et Cosmochimica Acta*, **67 4**, 575–586.

M. Reich and H. Bao (2018). 'Nitrate deposits of the atacama desert: A marker of long-term hyperaridity'. *Elements*, **14 4**, 251–256.

V. C. Rennie and A. V. Turchyn (2014). 'Controls on the abiotic exchange between aqueous sulfate and water under laboratory conditions'. *Limnology and Oceanography: Methods*, **12**, 166–173.

M. Reyers and Y. Shao (2019). 'Cutoff lows off the coast of the Atacama Desert under present day conditions and in the Last Glacial Maximum'. *Global and Planetary Change*, **181**, 102983.

B. Ritter, S. A. Binnie, F. M. Stuart, V. Wennrich and T. J. Dunai (2018). 'Evidence for multiple Plio-Pleistocene lake episodes in the hyperarid Atacama Desert'. *Quaternary Geochronology*, **44**, 1–12.

P. W. Rundel, M. O. Dillon, B. Palma, H. A. Mooney and S. L. Gulmon (1991). 'The Phytogeography and Ecology of the Coastal Atacama and Peruvian Deserts'. *Aliso: A Journal of Systematic and Evolutionary Botany*, **13 1**, 1–49.

J. A. Rutllant, H. Fuenzalida and P. Aceituno (2003). 'Climate dynamics along the arid northern coast of Chile: The 1997-1998 Dinámica del Clima de la Región de Antofagasta (DICLIMA) experiment'. *Journal of Geophysical Research D: Atmospheres*, **108 17**, 1–13.

C. Sager, A. Airo, F. L. Arens and D. Schulze-Makuch (2021). 'New type of sand wedge polygons in the salt cemented soils of the hyper-arid Atacama Desert'. *Geomorphology*, **373**, 107481.

N. Sakamoto, Y. Seto, S. Itoh, K. Kuramoto, K. Fujino, K. Nagashima, A. N. Krot and H. Yurimoto (2007). 'Remnants of the early solar system water enriched in heavy oxygen isotopes'. *Science*, **317**, 231–233.

M. Salifu, T. Aiglsperger, L. Hällström, O. Martinsson, K. Billström, J. Ingri, B. Dold and L. Alakangas (2018). 'Strontium ($^{87}Sr/^{86}Sr$) isotopes: A tracer for geochemical processes in mineralogically-complex mine wastes'. *Applied Geochemistry*, **99**, 42–54.

J. Savarino, B. Alexander, V. Darmohusodo and M. H. Thiemens (2001). 'Sulfur and oxygen isotope analysis of sulfate at micromole levels using a pyrolysis technique in a continuous flow system'. *Analytical Chemistry*, **73 18**, 4457–4462.

J. Savarino, C. C. W. Lee and M. H. Thiemens (2000). 'Laboratory oxygen isotopic study of sulfur (IV) oxidation: Origin of the mass-independent oxygen isotopic anomaly in atmospheric sulfates and sulfate mineral deposits on Earth'. *Journal of Geophysical Research*, **105 D23**, 29079–29088.

J. Savarino and M. H. Thiemens (1999). 'Analytical procedure to determine both $\delta^{18}O$ and $\delta^{17}O$ of H_2O_2 in natural water and first measurements'. *Atmospheric Environment*, **33 22**, 3683–3690.

A. J. Schauer, S. A. Kunasek, E. D. Sofen, J. Erbland, J. Savarino, B. W. Johnson, H. M. Amos, R. Shaheen, M. Abaunza, T. L. Jackson, M. H. Thiemens and B. Alexander (2012). 'Oxygen isotope exchange with quartz during pyrolysis of silver sulfate and silver nitrate'. *Rapid Communications in Mass Spectrometry*, **26**, 2151–2157.

K. W. Scheihing, C. E. Moya, U. Struck, E. Lictevout and U. Tröger (2018). 'Reassessing hydrological processes that control stable Isotope Tracers in groundwater of the Atacama Desert (Northern Chile)'. *Hydrology*, **5 1**, 7–11.

B. Schueler, J. Morton and K. Mauersberger (1990). 'Measurements of isotopic abundances in collected stratospheric ozone samples'. *Geophysical Research Letters*, **17 9**, 1295–1298.

J. H. Schween, D. Hoffmeister and U. Löhnert (2020). 'Filling the observational gap in the Atacama Desert with a new network of climate stations'. *Global and Planetary Change*, **184**, 103034.

A. Seidell and W. F. Linke (1919). *Solubilities of Inorganic and Organic Compounds*. D. Van Nostrand Co., New York, 2nd ed.

R. Shaheen, M. Abauanza, T. L. Jackson, J. McCabe, J. Savarino and M. H. Thiemens (2013). 'Tales of volcanoes and El-Niño southern oscillations with the oxygen isotope anomaly of sulfate aerosol'. *Proceedings of the National Academy of Sciences of the United States of America*, **110 44**, 17662–17667.

Z. D. Sharp, J. A. Gibbons, O. Maltsev, V. Atudorei, A. Pack, S. Sengupta, E. L. Shock and L. P. Knauth (2016). 'A calibration of the triple oxygen isotope fractionation in the SiO_2 - H_2O system and applications to natural samples'. *Geochimica et Cosmochimica Acta*, **186**, 105–119.

References

P. C. Singer and W. Stumm (1970). 'Acidic Mine Drainage: The Rate-Determining Step'. *Science*, **167**, 1121–1124.

E. D. Sofen, B. Alexander and S. A. Kunasek (2011). 'The impact of anthropogenic emissions on atmospheric sulfate production pathways, oxidants, and ice core $\Delta^{17}O(SO_4{}^{2-})$'. *Atmospheric Chemistry and Physics*, **11**, 3565–3578.

T. Sun, H. Bao, M. Reich and S. R. Hemming (2018). 'More than ten million years of hyper-aridity recorded in the Atacama Gravels'. *Geochimica et Cosmochimica Acta*, **227**, 123–132.

J. Surma, S. Assonov, M. J. Bolourchi and M. Staubwasser (2015). 'Triple oxygen isotope signatures in evaporated water bodies from the Sistan Oasis, Iran'. *Geophysical Research Letters*, **42 20**, 8456–8462.

J. Surma, S. Assonov, D. Herwartz, C. Voigt and M. Staubwasser (2018). 'The evolution of ^{17}O-excess in surface water of the arid environment during recharge and evaporation'. *Scientific Reports*, **8**, 4972.

J. Surma, S. Assonov and M. Staubwasser (2021). 'Triple Oxygen Isotope Systematics in the Hydrologic Cycle'. *Reviews in Mineralogy and Geochemistry*, **86**, 401–428.

J. Tapia, R. González, B. Townley, V. Oliveros, F. Álvarez, G. Aguilar, A. Menzies and M. Calderón (2018). 'Geology and geochemistry of the Atacama Desert'. *Antonie van Leeuwenhoek, International Journal of General and Molecular Microbiology*, **111 8**, 1273–1291.

A. Teplukhin and D. Babikov (2018). 'Several Levels of Theory for Description of Isotope Effects in Ozone: Symmetry Effect and Mass Effect'. *Journal of Physical Chemistry A*, **122 47**, 9177–9190.

M. Thiel, E. Macaya, E. Acuña, W. Arntz, H. Bastias, K. Brokordt, P. Camus, J. Castilla, L. Castro, M. Cortés, C. Dumont, R. Escribano, M. Fernández, J. Gajardo, C. Gaymer, I. Gomez, A. González, H. González, P. Haye, J.-E. Illanes, J. Iriarte, D. Lancellotti, G. Luna-Jorquera, C. Luxoro, P. Manríquez, V. Marín, P. Muñoz, S. Navarrete, E. Perez, E. Poulin, J. Sellanes, H. Sepúlveda, W. Stotz, F. Tala, A. Thomas, C. Vargas, J. Vasquez and J. Alonso Vega (2007). 'The Humboldt Current System of Northern and Central Chile Oceanographic Processes, Ecological Interactions and Socioeconomic Feedback'. *Oceanography and Marine Biology*, **45**, 195–344.

M. H. Thiemens (2006). 'History and Applications of Mass-Independent Isotope Effects'. *Annual Review of Earth and Planetary Sciences*, **34 1**, 217–262.

M. H. Thiemens (2013). 'Introduction to chemistry and applications in nature of mass independent isotope effects special feature'. *Proceedings of the National Academy of Sciences of the United States of America*, **110 44**, 17631–17637.

M. H. Thiemens and J. E. Heidenreich (1983). 'The mass-independent fractionation of oxygen: A novel isotope effect and its possible cosmochemical implications'. *Science*, **219**, 1073–1075.

M. H. Thiemens and M. Lin (2021). 'Discoveries of Mass Independent Isotope Effects in the Solar System : Past, Present and Future'. *Reviews in Mineralogy and Geochemistry*, **86**, 35–95.

H. Thode (1991). 'Sulphur Isotopes in Nature and the Environment: An Overview'. In 'Stable isotopes: natural and anthropogenic sulphur in the environment', John Wiley & Sons, Inc., 1–26.

R. S. Thurston, K. W. Mandernack and W. C. Shanks (2010). 'Laboratory chalcopyrite oxidation by Acidithiobacillus ferrooxidans: Oxygen and sulfur isotope fractionation'. *Chemical Geology*, **269**, 252–261.

M. Tichomirowa and M. Junghans (2009). 'Oxygen isotope evidence for sorption of molecular oxygen to pyrite surface sites and incorporation into sulfate in oxidation experiments'. *Applied Geochemistry*, **24 11**, 2072–2092.

A. V. Turchyn and D. P. Schrag (2004). 'Oxygen Isotope Constraints on the Sulfur Cycle over the Past 10 Million Years'. *Science*, **303**, 2004–2007.

R. Uemura, E. Barkan, O. Abe and B. Luz (2010). 'Triple isotope composition of oxygen in atmospheric water vapor'. *Geophysical Research Letters*, **37 4**, 1–4.

UNEP (2011). 'Global Drylands: A UN system-wide response'. Tech. rep., United Nation Environmental Management Group.

H. C. Urey (1947). 'The Thermodynamic Properties of Isotopic Substances'. *Journal of the Chemical Society*, 562–581.

H. C. Urey and C. A. Bradley (1931). 'On the relative abundances of isotopes'. *Physical Review*, **38 4**, 718–724.

P. Victor, O. Oncken and J. Glodny (2004). 'Uplift of the western Altiplano plateau: Evidence from the Precordillera between 20° and 21°S (northern Chile)'. *Tectonics*, **23 4**.

B. Viguier, H. Jourde, V. Leonardi, E. Lictevout and L. Daniele (2020). 'Water table variations in atacama desert alluvial fans: Discussion of "evidence of short-term groundwater

recharge signal propagation from the andes to the central atacama desert: A singular spectrum analysis approach"'. *Hydrological Sciences Journal*, **65 9**, 1606–1613.

I. M. Villa, P. De Bièvre, N. E. Holden and P. R. Renne (2015). 'IUPAC-IUGS recommendation on the half life of ^{87}Rb'. *Geochimica et Cosmochimica Acta*, **164**, 382–385.

C. Voigt, D. Herwartz, C. Dorador and M. Staubwasser (2021). 'Triple oxygen isotope systematics of evaporation and mixing processes in a dynamic desert lake system'. *Hydrology and Earth System Sciences Discussions*, **25**, 1211–1228.

C. Voigt, S. Klipsch, D. Herwartz, G. Chong and M. Staubwasser (2020). 'The spatial distribution of soluble salts in the surface soil of the Atacama Desert and their relationship to hyperaridity'. *Global and Planetary Change*, **184**.

A. R. Waldeck, B. R. Cowie, E. Bertran, B. A. Wing, I. Halevy and D. T. Johnston (2019). 'Deciphering the atmospheric signal in marine sulfate oxygen isotope composition'. *Earth and Planetary Science Letters*, **522**, 12–19.

J. Walk, G. Stauch, M. Reyers, P. Vásquez, F. A. Sepúlveda, M. Bartz, D. Hoffmeister, H. Brückner and F. Lehmkuhl (2020). 'Gradients in climate, geology, and topography affecting coastal alluvial fan morphodynamics in hyperarid regions – The Atacama perspective'. *Global and Planetary Change*, **185**, 102994.

W. W. Walters, G. Michalski, J. K. Böhlke, B. Alexander, J. Savarino and M. H. Thiemens (2019). 'Assessing the Seasonal Dynamics of Nitrate and Sulfate Aerosols at the South Pole Utilizing Stable Isotopes'. *Journal of Geophysical Research: Atmospheres*, **124 14**, 8161–8177.

F. Wang, W. Ge, H. Luo, J.-H. Seo and G. Michalski (2016). 'Oxygen-17 anomaly in soil nitrate: A new precipitation proxy for desert landscapes'. *Earth and Planetary Science Letters*, **438 3**, 103–111.

F. Wang, G. Michalski, J.-H. Seo and W. Ge (2014). 'Geochemical, isotopic, and mineralogical constraints on atmospheric deposition in the hyper-arid Atacama Desert, Chile'. *Geochimica et Cosmochimica Acta*, **135**, 29–48.

S. D. Wankel, A. S. Bradley, D. L. Eldridge and D. T. Johnston (2014). 'Determination and application of the equilibrium oxygen isotope effect between water and sulfite'. *Geochimica et Cosmochimica Acta*, **125**, 694–711.

K. Wedepohl (1991). 'Chemical composition and fractionation of the continental crust'. *Geologische Rundschau*, **80 2**, 207–223.

A. Willmes (1993). *Taschenbuch Chemische Substanzen: Elemente - Anorganika - Origanika - Naturstoffe - Polymere*. Harri Deutsch - Thun, Frankfurt am Main, 1st ed.

U. G. Wortmann, B. Chernyavsky, S. M. Bernasconi, B. Brunner, M. E. Böttcher and P. K. Swart (2007). 'Oxygen isotope biogeochemistry of pore water sulfate in the deep biosphere: Dominance of isotope exchange reactions with ambient water during microbial sulfate reduction (ODP Site 1130)'. *Geochimica et Cosmochimica Acta*, **71 17**, 4221–4232.

L. Xie, B. Spiro and G. Wei (2016). 'Purification of $BaSO_4$ precipitate contaminated with organic matter for oxygen isotope measurements ($\delta^{18}O$ and $\Delta^{17}O$)'. *Rapid Communications in Mass Spectrometry*, **30 14**, 1727–1733.

E. D. Young, A. Galy and H. Nagahara (2002). 'Kinetic and equilibrium mass-dependent isotope fractionation laws in nature and their geochemical and cosmochemical significance'. *Geochimica et Cosmochimica Acta*, **66 6**, 1095–1104.

R. E. Zeebe (2010). 'A new value for the stable oxygen isotope fractionation between dissolved sulfate ion and water'. *Geochimica et Cosmochimica Acta*, **74 3**, 818–828.

A.

Appendix

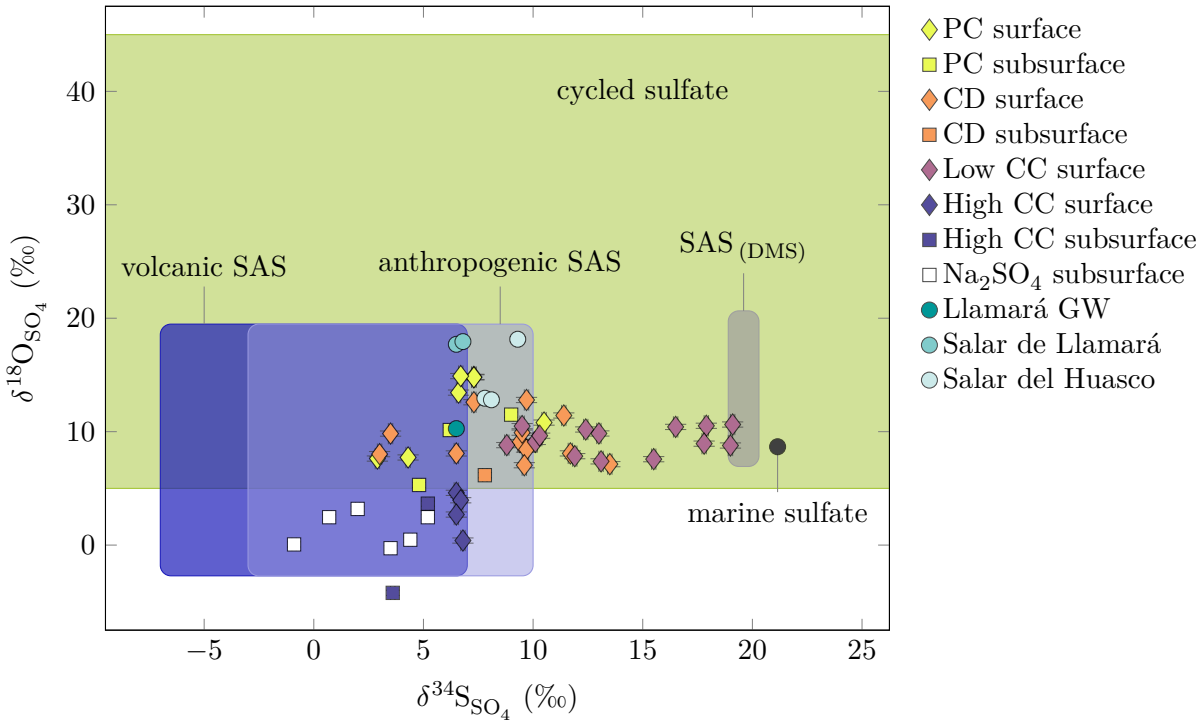

Figure A.1.: The $\delta^{18}O_{SO_4}$ and $\delta^{34}S_{SO_4}$ isotopic composition of each individual sulfate source. Sources include SAS that originates from volcanic and anthropogenic emissions and from biogenic sulfur gases (e.g., DMS), marine sulfate, and biological cycled sulfate. Additionally, all results of surface (diamonds) and subsurface (squares) samples from the Coastal Cordillera >1200 m (high CC) and <1200 m (low CC), the Central Depression (CD), and the Western Cordillera, Precordillera and its alluvial fans (PC) are displayed, along with results of Na_2SO_4 subsurface samples, groundwater, and salar samples.

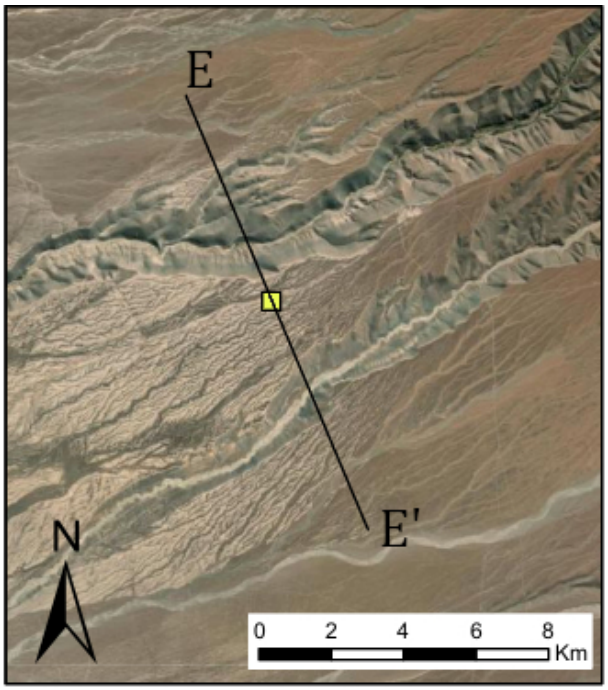

Figure A.2.: Sample location of Ata19-044c. The indicated profile is shown in Figure A.3.

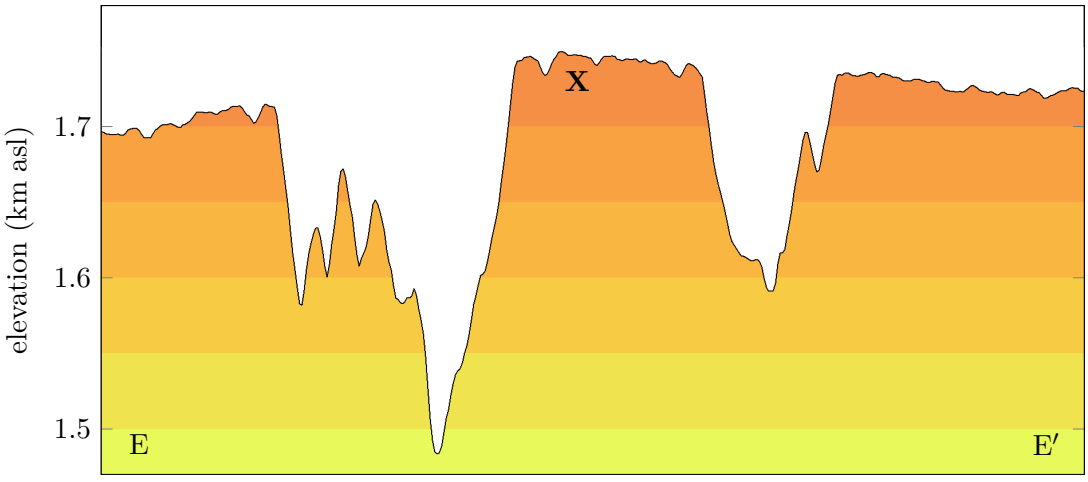

Figure A.3.: Topographic profile from the sample location of Ata19-044c indicated by X. Color shading changes every 50 m. The profile line is indicated in Figure A.2.

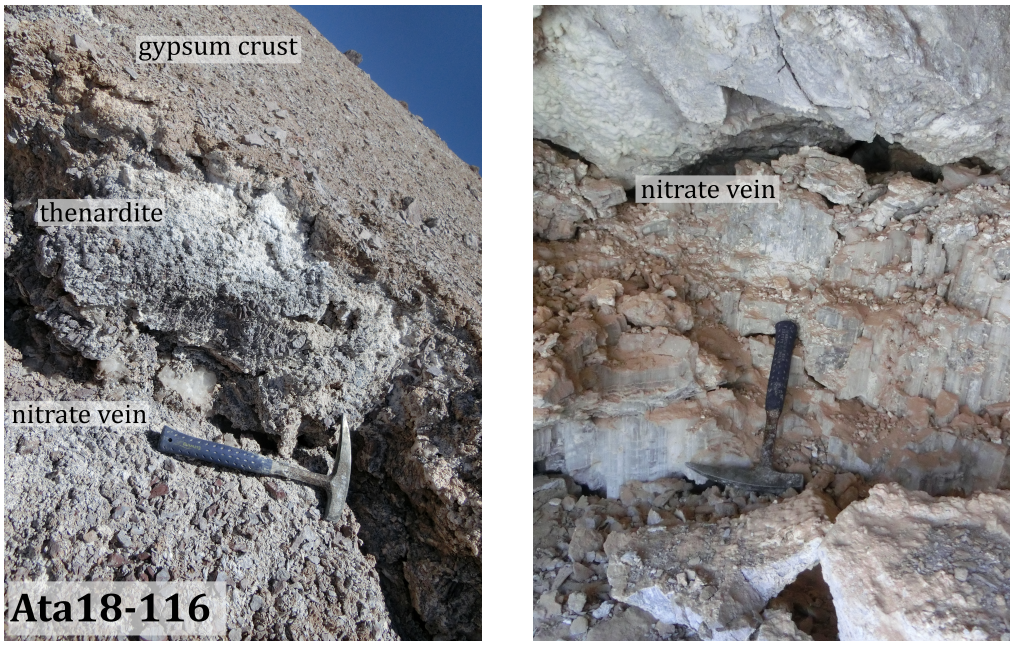

Figure A.4.: Pictures from the sample location of Ata18-116. Left panel: The surface is covered by a thin gypsum crust, followed by a few cm thick powdery thenardite layer. Further down a gypsum dominated horizon comprises multiple nitrate veins, which increase in size downwards (right panel). The picture in the right panel shows a nitrate vein approximately 2 m below the surface.

Table A.1.: Locations, classifications and isotope data of all samples. The mean 1σ standard deviation is 13 ppm, 0.1‰, 0.23‰, and 0.07‰ for $^{87}Sr/^{86}Sr$, $\delta^{34}S_{SO_4}$, $\delta^{18}O_{SO_4}$, and $\Delta^{17}O_{SO_4}$, respectively.

sample	type	transect	latitude	longitude	elevation (m.a.s.l.)	$^{87}Sr/^{86}Sr$	$\delta^{34}S_{SO_4}$ (‰)	$\delta^{18}O_{SO_4}$ (‰)	$\Delta^{17}O_{SO_4}$ (‰)
Precordillera and Western Cordillera									
Ata17-018a	surface	C	24°12.523′ S	68°47.625′ W	2993		4.3	7.73	0.51
Ata17-020a	surface	C	24°06.996′ S	68°42.121′ W	2991	0.707265	6.6	13.44	0.37
Ata17-026b	subsurface	C	24°11.182′ S	69°17.294′ W	2253		4.8	5.30	0.83
Ata17-087b	surface	A	19°28.372′ S	69°52.909′ W	1168		10.5	10.80	0.65
Ata18-004a	surface	D	24°54.091′ S	69°16.145′ W	2958		2.9	7.63	0.76
Ata19-044c	subsurface	A	19°27.030′ S	69°39.853′ W	1726		9.0	11.50	0.58
Ata19-076b	subsurface		22°16.264′ S	69°21.246′ W	1491		6.2	10.14	0.45
Ata19-088	surface	B	20°59.687′ S	69°16.503′ W	1405	0.708114	6.7	14.90	0.28
Ata19-091	surface	B	21°00.373′ S	69°20.455′ W	1208		7.3	14.78	0.37
Ata19-094	surface	B	21°05.262′ S	69°33.332′ W	819		7.3	14.83	0.34
Central Depression									
Ata17-014a	surface	C	24°02.024′ S	69°34.892′ W	1232	0.707347	9.4	9.08	0.80
Ata17-014b	subsurface	C	24°02.024′ S	69°34.892′ W	1232		7.8	6.16	0.84
Ata17-016a	surface	C	23°53.262′ S	69°48.983′ W	795	0.707622	11.7	8.08	0.73
Ata17-028b	surface	C	23°58.994′ S	69°40.298′ W	1090		9.7	8.42	0.67
Ata17-043a	surface		20°45.001′ S	69°45.200′ W	1155		9.6	7.04	0.71
Ata17-044a	surface		20°44.415′ S	69°56.448′ W	941		13.5	7.14	0.76
Ata17-055b	surface	B	21°12.842′ S	69°51.599′ W	825		11.4	11.42	0.37
Ata18-001a	surface		24°19.624′ S	69°57.701′ W	1288		3.5	9.83	0.61
Ata18-002	surface		24°19.624′ S	69°57.701′ W	1288		7.3	12.59	0.69
Ata18-038c	surface	B	21°05.858′ S	69°40.016′ W	888		9.7	12.79	0.49
Ata18-043a	surface	B	21°07.165′ S	69°56.995′ W	786		6.5	8.08	0.46

(continued)

sample	type	transect	latitude	longitude	elevation (m.a.s.l.)	$^{87}Sr/^{86}Sr$	$\delta^{34}S_{SO_4}$ (‰)	$\delta^{18}O_{SO_4}$ (‰)	$\Delta^{17}O_{SO_4}$ (‰)
Ata18-123a	surface		24°18.588′ S	69°58.906′ W	1263		3.0	8.02	0.50
Ata19-095a	surface	B	21°05.801′ S	69°40.034′ W	894		9.5	9.91	0.45
low Coastal Cordillera									
Ata17-008a	surface	C	23°42.213′ S	70°20.470′ W	929	0.708782	19.0	8.78	0.71
Ata17-010b	surface	C	23°41.807′ S	70°18.027′ W	613		15.5	7.58	0.47
Ata17-046a	surface		20°44.713′ S	70°02.073′ W	734		13.1	7.38	0.73
Ata17-047a	surface		20°47.304′ S	70°06.767′ W	551		16.5	10.42	0.66
Ata17-048a	surface	B	21°10.144′ S	70°04.444′ W	375	0.708754	19.1	10.63	0.59
Ata17-051a	surface	B	21°09.873′ S	70°02.275′ W	717		17.9	10.52	0.56
Ata17-052a	surface	B	21°09.703′ S	70°02.004′ W	735		17.8	8.94	0.49
Ata17-054a	surface	B	21°13.776′ S	69°58.319′ W	740	0.707825	13.0	9.84	0.51
Ata17-079a	surface	A	19°31.066′ S	70°09.584′ W	953		11.9	7.84	0.69
Ata17-080a	surface	A	19°30.930′ S	70°08.638′ W	945		12.4	10.19	0.64
Ata17-081a	surface	A	19°29.799′ S	70°07.390′ W	1053		10.1	9.10	0.61
Ata17-082a	surface	A	19°28.999′ S	70°05.347′ W	1007		8.8	8.81	0.59
Ata17-083a	surface	A	19°28.825′ S	70°03.629′ W	1076		10.3	9.64	0.58
Ata17-084a	surface	A	19°27.882′ S	70°01.168′ W	1024		9.5	10.49	0.52
high Coastal Cordillera									
Ata18-125a	surface	D	25°08.307′ S	69°55.081′ W	1809		6.5	4.61	0.97
Ata18-125c	subsurface	D	25°08.307′ S	69°55.081′ W	1809		5.2	3.65	0.89
Ata18-126a	surface	D	25°04.032′ S	69°59.818′ W	1935		6.7	3.95	0.78
Ata18-127a	surface	D	25°01.334′ S	70°06.847′ W	2087	0.706934	6.5	2.69	1.06
Ata18-127b	subsurface	D	25°01.334′ S	70°06.847′ W	2087		3.6	−4.21	0.95
Ata18-128a	surface	D	25°02.814′ S	70°15.368′ W	2113	0.709104	6.8	0.40	1.00

(continued)

sample	type	transect	latitude	longitude	elevation (m.a.s.l.)	$^{87}Sr/^{86}Sr$	$\delta^{34}S_{SO_4}$ (‰)	$\delta^{18}O_{SO_4}$ (‰)	$\Delta^{17}O_{SO_4}$ (‰)
Na_2SO_4									
Ata18-001c	subsurface		24°19.624′ S	69°57.701′ W	1288		−0.9	0.06	0.53
Ata18-115b	subsurface		23°47.788′ S	69°21.535′ W	1707		0.7	2.46	0.52
Ata18-116b	subsurface		23°48.354′ S	69°21.287′ W	1755		2.0	3.19	0.72
Ata18-121b	subsurface		23°46.582′ S	69°23.413′ W	1758		5.2	2.46	0.83
Ata18-125b	subsurface	D	25°08.307′ S	69°55.081′ W	1809		3.5	−0.28	0.99
Ata18-126b	subsurface	D	25°04.032′ S	69°59.818′ W	1935		4.4	0.47	0.85
Salar de Llamará									
Ata14-12d	Groundwater		21°16.364′ S	69°37.384′ W	755		6.5	10.27	0.27
Ata17-128	Ca-sulfate		21°16.196′ S	69°37.827′ W	763		6.5	17.70	0.22
Ata17-130	Ca-sulfate		21°16.193′ S	69°38.201′ W	750	0.707182	6.8	17.94	0.17
Salar del Huasco									
Ata18-056b	Na-sulfate		20°19.323′ S	68°51.831′ W	3786		9.3	18.15	0.14
Ata18-073b	Na-sulfate		20°17.764′ S	68°49.682′ W	3784	0.706122	7.8	12.95	0.13
Ata19-111b	Na-sulfate		20°17.695′ S	68°49.717′ W	3782		8.1	12.81	0.16

Erklärung

Hiermit versichere ich an Eides statt, dass ich die vorliegende Dissertation selbstständig und ohne die Benutzung anderer als der angegebenen Hilfsmittel und Literatur angefertigt habe. Alle Stellen, die wörtlich oder sinngemäß aus veröffentlichten und nicht veröffentlichten Werken dem Wortlaut oder dem Sinn nach entnommen wurden, sind als solche kenntlich gemacht. Ich versichere an Eides statt, dass diese Dissertation noch keiner anderen Fakultät oder Universität zur Prüfung vorgelegen hat; dass sie - abgesehen von unten angegebenen Teilpublikationen und eingebundenen Artikeln und Manuskripten - noch nicht veröffentlicht worden ist sowie, dass ich eine Veröffentlichung der Dissertation vor Abschluss der Promotion nicht ohne Genehmigung des Promotionsausschusses vornehmen werde. Die Bestimmungen dieser Ordnung sind mir bekannt. Darüber hinaus erkläre ich hiermit, dass ich die Ordnung zur Sicherung guter wissenschaftlicher Praxis und zum Umgang mit wissenschaftlichem Fehlverhalten der Universität zu Köln gelesen und sie bei der Durchführung der Dissertation zugrundeliegenden Arbeiten und der schriftlich verfassten Dissertation beachtet habe und verpflichte mich hiermit, die dort genannten Vorgaben bei allen wissenschaftlichen Tätigkeiten zu beachten und umzusetzen. Ich versichere, dass die eingereichte elektronische Fassung der eingereichten Druckfassung vollständig entspricht.

- Swea Klipsch -

Teilpublikationen:

S. KLIPSCH, D. HERWARTZ and M. STAUBWASSER (2021). 'Optimizing sulfate pyrolysis triple oxygen isotope analysis for samples from desert environments'. *Rapid Communications in Mass Spectrometry*, **35 14**, https://doi.org/10.1002/rcm.9102

S. KLIPSCH, D. HERWARTZ, C. VOIGT, C. MÜNKER, G. CHONG, M. E. BÖTTCHER and M. STAUBWASSER (in progress). 'Sulfate deposition mechanism, biologic cycling, and their relationship to water availability in Atacama Desert soils revealed by sulfate isotope signatures'.